NORTHWESTERN UNIVERSITY

Anisotropic van der Waals Materials for Polarization-Sensitive Photonics

A DISSERTATION

SUBMITTED TO THE GRADUATE SCHOOL

IN PARTIAL FULFILLMENT OF THE REQUIREMENTS

for the degree

DOCTOR OF PHILOSOPHY

Field of Electrical and Computer Engineering

By

Sina Abedini Dereshgi

EVANSTON, ILLINOIS

March 2023

ABSTRACT

Anisotropic van der Waals Materials for Polarization-Sensitive Photonics

Sina Abedini Dereshgi

The on-going demand for miniaturized optical and on-chip photonic systems of the future has led to a few potential solutions in the literature. Recent advances in van der Waals and 2-dimensional materials signal a bright future for the next generation, compact electronic and photonic devices. With reduced dimensionality and material thicknesses reaching down to atomic and molecular levels, 2-dimensional materials provide access to unique electrical, optical and mechanical properties that can enable compact, sub-diffraction limit and yet efficient devices. van der Waals materials are also compatible with all substrates and usually do not require restrictive crystal-matching requirements of conventional birefringent materials and can make up high-crystalline complex heterostructures. In this thesis several emerging van der Waals materials with anisotropic crystals are investigated and reintroduced as potential polarization-modulation candidates for the future on-chip photonics in visible, near-infrared and infrared, in the context of van der Waals metamaterials and low-symmetry vdW multilayers.

The mentioned bands of electromagnetic spectrum house critical technologies such as display systems, optical communication systems and atmospheric sensing systems.

For visible and near-infrared range, 2-dimensional metal borophene and transparent α-MoO_3 are investigated as strong candidates for polarization-dependent on-chip photonics. A detailed theoretical study is conducted on the anisotropic plasmonic response of borophene monolayer (a monolayer 2-dimensional metal) and patterned nanoribbons and nanopatches of borophene monolayer where polarization-sensitive absorption values in the order of 50% is obtained. It is demonstrated that by adding a metal layer, this absorption can be enhanced to 100%. We also examine giant dichroism in monolayer borophene which can be tuned passively (patterning) and actively (electrostatic gating) and our simulations yield 20% reflected light with significant polarization rotation. In another attempt to identify a vdW material that does not require patterning and metamaterial approach and is birefringent by nature, α-MoO_3 is investigated which exhibits a polarization-dependent refractive index due to its anisotropic crystal structure. Using polarizers and analyzers, we demonstrate that α-MoO_3 has negligible loss and birefringence values as high as 0.15 and 0.12 at 532 nm and 633 nm, respectively, is achievable. With such a high birefringence, we demonstrate quarter- and half-wave plate actions for a 1400 nm α-MoO_3 flake at green (532 nm) and red (633 nm) wavelengths and we report polarizability as high as 90%. Furthermore, we investigate a system of double α-MoO_3 heterostructure layer that provides the possibility of tuning polarization as a function of rotation angle between the α-MoO_3 layers. As a proof of concept, polarization-sensitive photonic devices including polarization reflectors and polarization color filters are designed and realized by constructing metal–insulator–metal FP cavities.

It is observed that resonance frequencies for designed transmission and reflection filters change up to 25 nm with incident polarization which stems from the birefringence of α-MoO_3.

In infrared, emerging anisotropic vdW materials, hexagonal boron nitride (hBN) and α-MoO_3 are studied and their rich phononic properties are tailored to polarization-sensitive photonics. For the van der Waals metamaterial approach, we investigate a structure composed of Au grating arrays fabricated onto a Fabry-Perot cavity composed of hBN, Ge, and Au back reflector layers. The plasmonic Fabry-Perot cavity reduces the required device thickness by enhancing modal interactions and introduces in-plane polarization sensitivity due to the Au array lattice. Our experiments show multiple absorption peaks of over 90% in the mid-infrared region and band stop filters with 80% efficiency using only a 15 nm hBN slab. Moreover, mode interaction with experimental coupling strengths as high as 10.8 meV in the mid-infrared region is investigated. Anticrossing splitting ascribed to the coupling of optical phonons to plasmonic modes can be tuned by the designed geometry which can be tailored to efficient response band engineering for infrared photonics. hBN is also analyzed by highlighting birefringence introduced by grating design on top of it. For the heterostructure van der Waals birefringent solution to polarization-sensitive photonics, α-MoO_3 has been identified as a birefringent van der Waals material capable of sustaining naturally orthogonal in-plane phonon modes in infrared. We investigate the polarization-dependent optical characteristics of cavities formed using α-MoO_3 on Ge-Au stacks to extend the degrees of freedom in the design of infrared photonic components exploiting the in-plane anisotropy of this material. Polarization-dependent absorption over 80% in a multilayer Fabry-

Perot structure with α-MoO_3 is reported without the need for nanoscale fabrication on the α-MoO_3. We observe coupling between the α-MoO_3 optical phonons and the Fabry-Perot cavity resonances. Using cross-polarized reflectance spectroscopy we show that the strong birefringence results in 15% of the total power converted into the orthogonal polarization with respect to incident wave. Infrared wave plate action is also demonstrated relying on the anisotropic optical phonons of α-MoO_3.

In this thesis, a further step is taken to tailor the cross-polarization spectrosopy of phonons to identifying crystal quality of materials with low crystal symmetry. We investigate the far-field characteristics of MOCVD-grown Ga_2O_3 thin films. With a combination of cross-polarization Fourier Transform Infrared Spectroscopy and Atomic Force Microscopy characterization techniques, we propose an easy and non-invasive route to distinguish $\varkappa$and βphases of Ga_2O_3 and study the quality of these crystals. Using numerical methods and cross-polarization spectroscopy, the depolarization characteristics of β-Ga_2O_3 is examined and depolarization strength values as high as 0.95 and 3.3 are measured respectively for 400 and 800 nm-thick β-Ga_2O_3. The strong birefringence near optical phonon modes of an 800 nm β-Ga_2O_3 on sapphire substrate is used to obtain several polarization states for the reflected light in the second atmospheric window (8-14 µm).

As a future path toward realizing tunable polarization modulation in infrared, a phase change material, VO_2, is combined with anisotropic van der Waals materials. We investigate the tunability of optical phonons of α-MoO_3 in a multilayer structure with VO_2 sandwiched between α-MoO_3 layer on top and a bottom reflector. Our experiments show the frequency and intensity tuning of 2 cm^{-1} and 11% for optical

phonons in the [100] direction and 2 cm^{-1} and 28% for optical phonons in the [010] crystal direction of α-MoO_3. Using the effective medium theory and dielectric models of each layer, we verify these findings with simulations. We also report preliminary results for actively tunable wave plate action in the same multilayer configuration. Our simulations reveal tunability of the response of the proposed multilayer system with heat that can toggle between quarter- and half-wave plate action in infrared.

These findings reveal the possibility to manipulate phase, amplitude and polarization of light in visible, near-infrared and infrared and provides insight into tunable manipulation of the properties of light using emerging van der Waals materials. We envisage that our findings can open new avenues in the quest for tunable polarization filters and low-loss, integrated planar photonics and in dictating polarization control, as well as camouflage and radiative cooling devices of the next generation.

Acknowledgements

First, I would like to express my sincere appreciation to Prof. Koray Aydin for his unmatched support from the first day of me receiving admission to Northwestern. During the highs and lows of PhD, he was always available with invaluable depth of knowledge and supervision and held me to a high standard. I would like to thank my committee members, Prof. Hooman Mohseni, Prof. Pedram Khalili and Prof. Vinayak Dravid for their support about thesis and non-thesis topics and their genuine guidance which made this thesis stronger.

I would like to thank my current and former teammates at Metamaterials and Nanophotonic Devices Lab (MNDL), especially Wisnu and Ibrahim for sharing the hardships of research and being wonderful colleagues and friends. I want to thank my collaborators, Yea-Shine and Akshay from Dravid group for their top-notch integrity that added to the quality of the pulications. I would also like to thank Prof. Larciprete and Prof. Centini from Sapienza for fruitful collaborations and scientific discussions. I also appreciate Prof. Razeghi for pushing collaborations to a higher standard.

I am also very grateful for making good friends in the path of my PhD; friends that cross beyond the definition of friendship and are more like family, especially during the Covid-19 pandemic. I would like to thank Aslan for being a real friend and a true example of academic integrity and passion for science. I appreciate my friend, Cesar for making Chicago feel like home for me. I want to thank Naghmeh, Rawan,

Simone, Alireza, Bahram, Amir, Maryam, Parisa, Ian, Lisa, Rohanna, Diego, Moe, Ali and countless other friends that are too many to be mentioned here. I am honored to be friends with such wonderful, accomplished and successful people and scientists.

Most importantly, I would like to thank my family for putting up with my rare presence during my PhD. I would like to especially thank my mom for her unconditional love and support for as long as I remember. I would also like to thank talented artist, my wonderful and loving sister for believing too much in me which was always heartwarming, and my father for not believing too much in me which was encouraging. He was the one who ignited the insatiable enthusiasm for science in me. I am grateful for the most recent addition to the people I adore, my lovely niece, Elsa, for always being on my side. I am also thankful for my brother-in-law for being the brother that I never had. My family has truly been my source of inspiration and the system of checks and balances that I need to go further in life.

Dedication

D

edicated to the Iranian women, for being the source of inspiration and courage. As Iranians, we are blessed to have them as our mentors, colleagues, friends and partners. Their courage has deservedly taken the world by storm.

Table of Contents

List of Tables

List of Figures

CHAPTER 1

Introduction

1.1. Optical anisotropy with vdW low crystal-symmetry materials

Anisotropy offers a platform for controlling the polarization of electromagnetic waves which is the back-bone of several polarization-sensitive photonic applications such as polarizers, waveplates [1, 2, 3], light modulators [4], spectroscopy systems [5], nonlinear optical devices [3, 6, 7], liquid crystal displays [8] and biological tissue imaging [9]. In a nutshel, anisotropic crystals give rize to optical polarization sensitivity that provide an extra parameter, i.e. polarization, to design versatile photonic devices. Despite the availability of anisotropic materials, the ever-growing demand for realizing miniaturized polarization-sensitive devices drives the research for novel platforms for polarization-sensitive on-chip photonics. Optical anisotropy can be achieved both through the well-established natural crystals such as $CaCO_3$ birefringent crystal [10] or through artificially made crystals, aka metamaterials [11] in visible range (VIS). With the advent of graphene [12] and the recent groundbreaking advances in understanding and realizing of van der Waals (vdW) materials, specifically low-symmetry crystals such as black phosphorus (BP) new avenues have opened up to the miniaturization of integrated photonics. vdW materials are layered crystals of materials that are highly crystaline and can be exfoliated down to monolayers. The promise of these materials is in their innate surface passivation. This property puts vdW materials in a unique

position; they can be transferred onto different substrates to be integrated in heterostructures of different vdW materials to yield novel photonic applications [13]. Bulky polarizers and wave plates used for the second atmospheric window in infrared (8 - 14 μm) have been reported in the past decades, the most notable ones being ZnSe and ZnS wire grid polarizers [14, 15] that are standard optical components for polarimetry in infrared. Besides ZnSe and ZnS, there are reports of other bulky elements such as silicides (WSi) [16] and birefringent polymers [17]. Analoguous to their VIS counterparts, these wave plates are bulky and cannot be grown on arbitrary substrates and are not a viable option on-chip photonics. In this thesis, vdW materials are identified as a solution for on-chip infrared photonics thanks to strong dispersion near their optical phonon resonances. These routes also add to the generally lacking photonic components for the second atmospheric window.

1.2. Polarization-sensitive metamaterials

Artificially-introduced anisotropy in metamaterials can be achieved by patterning natural materials or by adding polarization symmetry-breaking features. Artificial materials (*aka* metamaterials) consist of reflective and transparent domains or alternatively, different dielectrics, which are usually developed with intricate fabrication methods that rely on periodic sub-wavelength features patterned using laborious lithography techniques [18]. In recent years, metamaterials have proven to be a viable solution for polarization control. Relying on mietronics, plasmonics and phononics achievable with metamaterials, several applications have been stipulated and implemented covering light generation [19, 20], guiding and beaming [21, 22, 23, 24, 25], confining [26, 27, 28,

29], and detection [30, 31]. Passive [32] and active [33] manipulation of polarization has also been successfully demonstrated by metamaterials at the expense of high-budget and time-consuming patterning methods associated with metamaterials. Metamaterials are known to host high-momentum modes that are wave-matter quasiparticles named polaritons. Polaritons are not accessible by direct excitation with light due to their higher momenta, which are much higher than light-line in free space. Therefore, small spatial features should be incorporated that serve to diffract light to a wide range of momenta which can in turn excite polaritons that are tightly confined to the surfaces [13]. From the library of polaritons, plasmon polaritons (PP) and phonon polaritons (PhP) are mostly sought for anisotropy. The most straightforward approach to excite PPs is using a metal-dielectric interface where the metal layer has negative permittivity and is patterned in deep subwavelength dimensions to launch high momenta modes. Therefore, light couples to the free electrons in the material interface that oscillate and launch PPs [34]. The occurance of PhPs is similar; polar materials have reststrahlen (RS) bands where each RS band is bracketed by transverse (*TO*) and longitudinal (*LO*) optical phonons. In RS band, permittivity is negative and a metal-insulator surface is mimicked. Hence, the charge oscillation can be sustained [35]. The only difference between PPs and PhPs is that the former takes place when light is coupled to electron oscillations and the latter when the light couples to the lattice vibrations. Consequently, PPs occur at higher frequencies due to the smaller effective masses of electrons, reaching visible (VIS) and near-infrared (NIR) frequencies [13], as opposed to PhPs that occur in mid-IR. Metamaterials and some naturally polar materials can demonstrate hyperbolicity in RS bands. Hyperbolicity [13, 36] is an extreme form of birefringence where one

or more of the crystal axes have a negative dielectric function, whilst the other(s) are positive. Therefore, not only does hyperbolicity address anisotropy, but also, it reduces the required device dimensions by few orders of magnitude [6]. Metamaterials usually require smaller device footprints to achieve strong birefringence compared to natural low-symmetry crystals of vdW materials. However, achieving hyperbolicity with metamaterials can be challenging since these class of materials are prone to fabrication non-idealities; the geometric quality of the periodic cell and associated fabrication non-idealities, compromise the photonic figures of merit of the devices [18]. Contrarily, naturally hyperbolic materials have innate hyperbolicity encoded in their single-crystal atomic arrangement.

1.3. Limitations of polaritons

Apart from usual photonic applications such as guiding, lasing and confining, polaritons and hyperbolicity contribute to enhanced light-matter interaction and make way for intriguing photonic applications such as hyperlensing [37, 38, 39], canalization [36] and negative refraction [40]. In an attempt to extend the list of the potential applications of polaritons, we report that the anisotropic PPs can significantly alter the polarization of the light in the first 2D metal, borophene, that was recently grown. Despite these exotic applications, polaritons are mostly near-field effects and they are associated with considerable losses. PPs suffer from high Ohmic losses associated with light-electron coupling mechanism. This loss mechanism, specifically in metals impede their application for technologies with light below the diffraction limit since almost half of the total energy is stored in the form of kinetic energy and is therefore subjected

to loss mechanisms, such as phonon assisted absorption, electron electron scattering, Landau dampening and interband absorption [41]. This can lead to localized heating [42, 43] that can be undesirable in temperature-sensitive applications and can cause deformation of nanostructures and reduced optical performance over time given that there is an inverse relation between melting temperature and particle size [44]. Therefore, refractory material plasmonics [45], Mie resonances [46], 2D material plasmonics [47] as well as PhPs [13] are being considered as possible routes to address the realizability issues that are concomitant to PPs. One of the routes to obtain reliable anisotropy is to benefit optical phonons (OPh) which can be excited with direct illumination and do not require lithography. In order to demonstrate the potential of OPhs in interacting with radiation, we have experimentally realized a structure with hexagonal boron nitride (hBN), where strong coupling of electromagnetic radiation to the system is observed. Polarization sensitivity is also introduced with grating structure integrated to hBN. However, hBN does not have in-plane anisotropy which again requires nanofabrication to introduce birefringence that increases the nanofabrication time and budget. Therefore, another recently grown naturally birefringence material, α-MoO_3, is studied in a Fabry-Perot configuration that shows strong anisotropic response obviating the need for demanding lithography processes, both in VIS and IR. This thesis borrows insight from the existing bulky anisotropic optical components and attempts to demonstrate the potential of alternative low-dimentional materials for the polarization-sensitive applications in integrated photonics of the next generation. In-plane anisotropic vdW materials were introduced as a potential small-scale alternative route for polarization manipulation with the introduction of BP [48]. Further research into optical anisotropy of BP with orthorhombic crystal

[49] fueled widespread interest in recognizing anisotropic crystals that give rise to vdW materials with optical and electrical anisotropy [50]. Ever since, a myriad of anisotropic vdW crystals with in-plane optical anisotropy have been identified and studied, such as orthorhombic SnSe [51], monoclinic GaTe [51] and triclinic ReS_2 [52]. Such low-symmetry crystals are promissing candidates for miniaturized on-chip polarization-sensitive photonics. In this direction, several emerging birefringent materials have been investigated in this report, specifically, orthorhombic α-MoO_3 and monoclinic β-Ga_2O_3.

1.4. Thesis outline

In this thesis, several emerging vdW materials and their anisotropic optical properties are investigated. In Chapter 2 we will introduce optical modeling techniques for emerging vdW materials, followed by developing a universal electromagnetic simulation method based on Transfer Matrix Method (TMM). In Chapters 3 and 4 vdW materials are investigated for polarization-sensitive on-chip photonics in VIS/NIR and IR, respectively. Each of the Chapters 3 and 4 offer two solutions using vdW materials:

(1) vdW materials and their incorporation to polaritonics with metamaterials,

(2) vdW materials incorporated to multilayers relying on their low crystal-symmetry strong birefringent dispersion.

Chapter 3 is dedicated to emerging birefringent vdW materials for VIS and NIR polarizing photonics. On the polaritonics front, a theoretical investigation of anisotropic plasmonic optical response of an recently-grown 2D metal, borophene, in VIS and NIR is investigated, followed by theoretical and experimental investigation of natural birefringence of a

strong birefringence vdW material, α-MoO_3 in VIS. Chapter 4 extends the discussion to the infrared polarization-dependent photonics with anisotropic phononic vdW material, hBN, where metal gratings are used to enhance its optical response in infrared by coupling PPs to OPhs as the metamaterial solution. In another attempt to address birefringence in infrared using natural anisotropy of vdW crystals, a versatile material, α-MoO_3 is studied in detail and quarter wave plates are designed using this material. In Chapter 5, β-Ga_2O_3 is rediscovered as a polarizing material for mid-infrared, and polarization-dependent infrared spectroscopy is introduced as a solid method to guage the crystal quality of this material that is important for ultraviolet optoelectronics. This thesis report concludes with Chapter 6, where a further step is taken to introduce active tunability to polarization control using a phase change material, VO_2, followed by future possibilities for tunable on-chip IR waveplates using low-symmetry vdW materials and phase change materials. Chapter 6 also highlights preliminary results for active tuning of polarization using VO_2.

The publications that are included in this report are listed below. This thesis also includes results from two other submitted manuscripts.

- Abedini Dereshgi, S., Liu, Z. and Aydin, K. "Anisotropic localized surface plasmons in borophene." *Optics Express*, 28 (11), pp.16725-16739 (2020) [53].
- Song, X., Abedini Dereshgi, S., Palacios, E., Xiang, Y. and Aydin, K. "Enhanced Interaction of Optical Phonons in h-BN with Plasmonic Lattice and Cavity Modes. " *ACS Applied Materials & Interfaces*, 28 (11), pp.16725-16739 (2021) [27].

- Abedini Dereshgi, S., Folland, T.G., Murthy, A.A., Song, X., Tanriover, I., Dravid, V.P., Caldwell, J.D. and Aydin, K. "Lithography-free IR polarization converters via orthogonal in-plane phonons in α-MoO_3 flakes." *Nature Communications*, 11(1), pp.1-9 (2020) [54].
- Abedini Dereshgi, S., Larciprete, M., Centini, M., Murthy, A.A., Tang, K., Wu, J., Dravid, V.P. and Aydin, K. "Tuning of Optical Phonons in α-MoO_3-VO_2 Multilayers." *ACS Applied Materials & Interfaces*, (2021) [55].
- Wei, C., Abedini Dereshgi, S., Song, X., Murthy, A., Dravid, V.P., Cao, T. and Aydin, K. "Polarization Reflector/Color Filter at Visible Frequencies via Anisotropic α-MoO_3." *Advanced Optical Materials*, 11(1), pp.2000088 (2020) [56].

CHAPTER 2

Simulations and Methods

In this chapter, the simulations and methods used to shed light on the physical phenomena taking place in the systems are described in more detail. The simulations are partly carried out using full wave simulation software Lumerical finite difference time domain (FDTD solutions). Although this software is well-established in the photonics community, it is time-consuming and would give little insight to the problem under study due to its great user interface and little effort required for its modeling. Therefore, for reasonably simpler structures, which happens to be the case for the most of the heterostructures, a full wave solver code is developed in MATLAB and material modelings are added as library to it.

2.1. 2×2 Transfer Matrix Method for multilayers with diagonal dielectric tensors

Transfer Matrix Method (TMM) is well-known in photonics community for solving Maxwell equations in multilayer structures with known boundary conditions. However, most of the formulations deal with isotropic and lossless structures and are not applicable when there are layers with complex refractive indices and different crystal orientations in heterostructure form. In an attempt to address this issue, a TMM code is developed that can tackle various complex diagonal dielectric tensors, incident polarizations and incident angles, as well as heterostructures with different crystal orientation on top.
In cartesian coordinates $\hat{x}o\hat{y}o\hat{z}$, when the material of interest has a diagonal dielectric

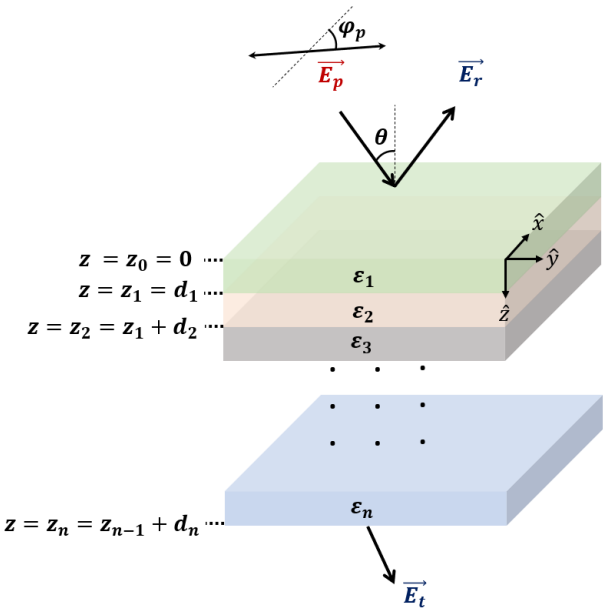

Figure 2.1. Schematic representation of multilayer system for solving TMM.

tensor and the orientation of materials are parallel in Cartesian coordinates, the problem can be decoupled to two 2D orthogonal 2×2 systems, $\hat{x}o\hat{z}$ and $\hat{y}o\hat{z}$. Afterwards, the farfield transmittance (T) and reflectance (R) along with reflected and transmitted fields can be calculated from the superposition of the two solved orthogonal problems. In all of the derivations throughout this study, the relative permittivity ε_r is represented by ε for simplicity and increasing the legibility of the equations, noting that the relative and total permittivity have the relation $\varepsilon_r = \varepsilon/\varepsilon_0$.

Figure 2.1 schematically shows the multilayer system that is solved using TMM. The Electric field ($\mathbf{E}$) in each medium m and direction $\hat{j}$, propagating along optical axis

$\hat{z}$ (Figure 2.1) can be written in 2D as

$$\vec{\mathbf{E}} = \mathbf{E}_{j,m}(j,z)\hat{j}, \tag{2.1}$$

$$\mathbf{E}_{j,m}(j,z) = \mathcal{E}_{j,m}(z)\exp(iqj), \tag{2.2}$$

$$\mathcal{E}_{j,m}(z) = C_m^+ \exp(-ik_{z,m}z) + C_m^- \exp(ik_{z,m}z), \qquad j = x, y. \tag{2.3}$$

In Equations 2.2 and 2.3, q is the tangential wavevector and $\mathcal{E}$ is the electric field amplitude function including counter-propagating waves represented by C^+ and C^-. The boundary conditions enforce the tangential component of the wavevector q, to be equal in all layers,

$$q_x = \left(\frac{2\pi}{\lambda}\right)\sin(\theta)\cos(\phi_p), \qquad q_y = \left(\frac{2\pi}{\lambda}\right)\sin(\theta)\sin(\phi_p), \tag{2.4}$$

where λ is the wavelength, and θ and ϕ_p are respectively the incidence angle and incident polarization (or polarizer) angle with respect to $\hat{x}$ axis. Note that this equation is written in a way that corresponds to TEM waves only. It can be applied to TE and TM waves, as will be discussed later in this section. The prependicular component of the wavevector can be found in each layer using the following equation

$$k_{zj,m} = \sqrt{\varepsilon_{jj,m}[\left(\frac{2\pi}{\lambda}\right)^2 - \left(\frac{q^2}{\varepsilon_{zz,m}}\right)]}, \qquad \Im m(k_{zj,m}) \geq 0, \tag{2.5}$$

where $\Im m(k_{z,m}) \geq 0$ enforces decay and/or propagation in the layers and $\varepsilon_{jj,m}$ is the diagonal component of dielectric function tensor in direction $\hat{j}$,

$$\bar{\bar{\varepsilon}}_m = \begin{bmatrix} \varepsilon_{xx,m} & 0 & 0 \\ 0 & \varepsilon_{yy,m} & 0 \\ 0 & 0 & \varepsilon_{zz,m} \end{bmatrix}. \tag{2.6}$$

The coefficients (C) of the amplitude function in Equation 2.3 can be represented in terms of the reflection and transmission coefficients from the boundaries of layers m and n ($n = m + 1$), respectively r_{mn} and t_{mn}, which can be calculated as

(2.7)

$$Q_m = \frac{\varepsilon_{jj,m}}{k_{zj,m}}, \qquad r_{mn} = \frac{Q_n - Q_m + S_n}{Q_n + Q_m + S_n}, \qquad S_n = \frac{2\lambda}{c}\sigma_n(q,\lambda), \qquad t_{mn} = 1 + r_{mn},.$$

In Equation 2.7, c is the speed of light in free space and S represents the surface charge in the interface between layers m and n through the conductivity parameter σ [57]. Here, we use the definition for TE component which will satisfy TEM condition in normal illumination. Using these definitions, we can define the recursive boundary condition ($\mathbf{B_{mn}}$) and propagation ($\mathbf{P_{mn}}$) matrices

$$\mathbf{B_{mn}} = \frac{1}{t_{mn}} \begin{bmatrix} 1 & r_{mn} \\ r_{mn} & 1 \end{bmatrix}, \qquad \mathbf{P_{mn}} = \begin{bmatrix} \exp(-ik_{zj,n}d_n) & 0 \\ 0 & \exp(ik_{zj,n}d_n) \end{bmatrix}, \tag{2.8}$$

where d_n is the thickness of the n^{th} layer. The transmission matrix ($\mathbf{T_{mn}}$) can be calculated for each layer as

$$\begin{bmatrix} E_0 \\ rE_0 \end{bmatrix} = \prod_{m=0}^{N} \mathbf{T_{mn}} \begin{bmatrix} tE_0 \\ 0 \end{bmatrix}, \qquad \mathbf{T_{mn}} = \mathbf{B_{mn}}\mathbf{P_{mn}}. \tag{2.9}$$

In Equation 2.9, N is the total number of layers and 0 is the air where the incident light enters the system. E_0 is the total amplitude of light which is assumed to be equal to 1. r_j and t_j are respectively the total complex reflection and transmission coefficients of the system in direction $\hat{j}$. It is worth pointing out that in the total matrix the illumination is from top Figure 2.1; hence, the second row in the right-hand 2×1 matrix of Equation 2.9 vanishes. In other words, there is no backward illumination in the air medium after the sample and the transmitted backward propagating wave is set to 0. Using Equation 2.9, the problem boils down to a calculated total transmission matrix $\mathbf{T}$ which in turn can be used to obtain reflectance (R) and transmittance (T) of the entire system,

$$\mathbf{T}_j = \prod_{m=0}^{N} \mathbf{T_{mn}} = \begin{bmatrix} T_{11} & T_{12} \\ T_{21} & T_{22} \end{bmatrix}, \qquad R_j = |r_j|^2 = |\frac{T_{21}}{T_{11}}|^2, \qquad T_j = |\frac{k_{zj,N}}{k_{zj,0}}||t_j|^2 = |\frac{k_{zj,N}}{k_{zj,0}}||\frac{1}{T_{11}}|^2. \tag{2.10}$$

In Equation 2.10 N and 0 are the last and first layers respectively. Finally, absorbance (A) is simply calculated by $A_j = 1 - R_j - T_j$. In order to simulate an unpolarized transmission or reflection experiment, the incoming light can be divided in half in terms of intensity to represent the total transmission and reflection. The TMM can be solved twice to obtain T_x, R_x and T_y, R_y, or equivalently, $E_{0x} = E_0\cos(45)$ and

$E_{0y} = E_0 \sin(45)$,

(2.11) $$T = T_x + T_y, \qquad R = R_x + R_y. \qquad A = 1 - R - T.$$

As stated earlier, the derivations were solved for TE mode. In order to derive the TM component, electromagnetism duality theorem can be used [58], by following replacements,

(2.12) $$\mathbf{E} \rightarrow \mathbf{H}, \qquad \mathbf{H} \rightarrow -\mathbf{E} \qquad \mu \rightarrow \varepsilon \qquad \varepsilon \rightarrow \mu.$$

These conditions therefore can be set based on the specific experiment simulation conditions between TE, TM or TEM configurations.

2.2. TMM for polarization-sensitive spectroscopy

unpolarized measurements are demonstrated schematically in Figure 2.2a. In order to characterize the polarization-sensitive response of the materials used in this report polarizers and analyzers can be used. Three different polarization-dependent measurements are schematically illustrated in Figure 2.2b and c, showcasing polarizer-only, analyzer-only and polarizer-analyzer configurations. We define linear polarizers and analyzers, ϕ_p and ϕ_a respectively, for the purpose of this report; however, any arbitrary polarization can be defined and solved by the developed TMM. In order to maintain and analyze all of the polarization information in simulations, electric fields are calculated and converted to intensity (i.e. measured values) by magnitude square of the fields. The two configurations demonstrated in Figures 2.2b are equivalent due to Malus law and electromagnetic reciprocity. The reflected and transmitted electric fields in $\hat{x}$ ($\hat{y}$)

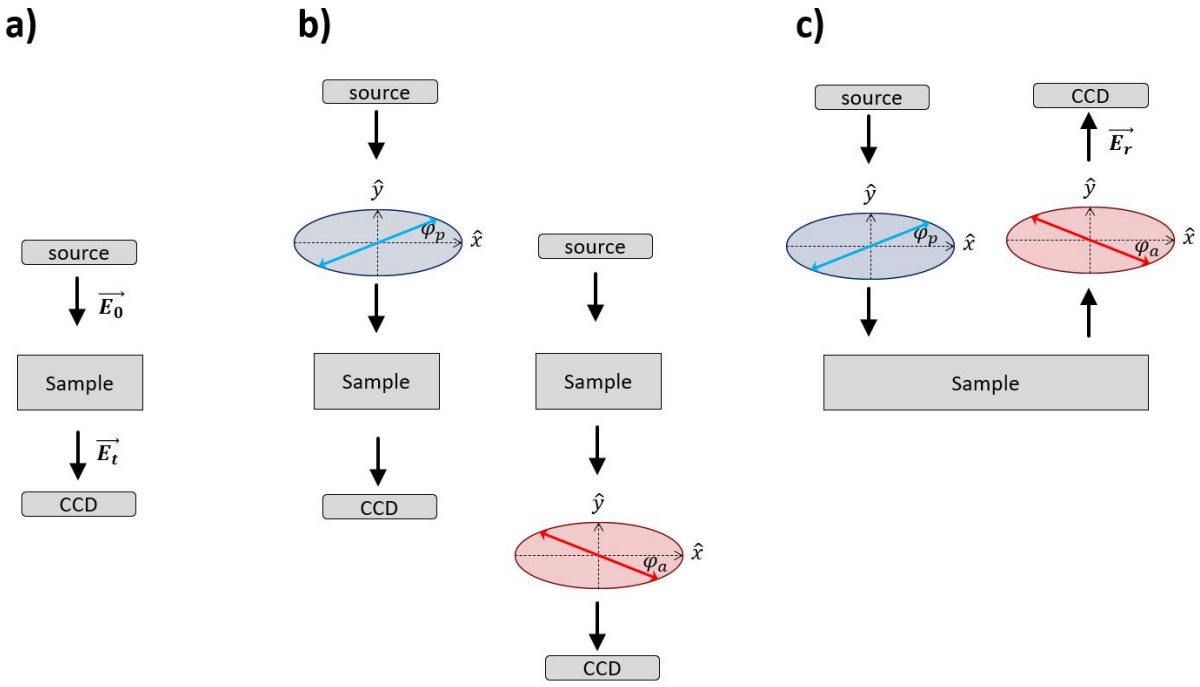

Figure 2.2. Measurement setup with (a) no polarizer or analyzer, (b) only polarizer and only analyzer in transmission mode. (c) Measurement set-up with polarizer and analyzer in reflection mode.

direction are $\mathcal{E}_{rx}$ ($\mathcal{E}_{ry}$) and $\mathcal{E}_{tx}$ ($\mathcal{E}_{ty}$), respectively. Deriving the electric field in farfield in case of adding only a polarizer to the optical path, we arrive at

$$\mathcal{E}_{rx} = r_x \cos(\phi_p) E_0, \qquad \mathcal{E}_{ry} = r_y \sin(\phi_p) E_0, \tag{2.13}$$

$$\mathcal{E}_{tx} = |\sqrt{\frac{k_{zx,N}}{k_{zx,0}}}| t_x \cos(\phi_p) E_0, \qquad \mathcal{E}_{ty} = |\sqrt{\frac{k_{zy,N}}{k_{zy,0}}}| t_y \sin(\phi_p) E_0. \tag{2.14}$$

The results for adding only an analyzer to the system will be the same where ϕ_p should be replaced by analyzer polarization, ϕ_a. Note that in case of adding only a polarizer (analyzer), the output fields will not interfere and they remain orthogonal, with all of the polarization information engraved in the solved $\mathcal{E}$, which in turn can be used to

visualize polarization ellipses of the transmitted and reflected light. The magnitude square of the results in Equation 2.14 yields R and T as

$$R = R_x + R_y = |\mathcal{E}_{rx}|^2 + |\mathcal{E}_{ry}|^2, \tag{2.15}$$

$$T = T_x + T_y = |\mathcal{E}_{tx}|^2 + |\mathcal{E}_{ty}|^2. \tag{2.16}$$

When both polarizer and analyzer are incorporated to the measurement in ellipsometer configuration illustrated schematically in Figure 2.2, the output electric fields can be calculated that carry the important polarization information,

$$\mathcal{E}_{rx} = r_x \cos(\phi_p) E_0 \cos(\phi_a), \qquad \mathcal{E}_{ry} = r_y \sin(\phi_p) E_0 \sin(\phi_a), \tag{2.17}$$

$$\mathcal{E}_{tx} = |\sqrt{\frac{k_{zx,N}}{k_{zx,0}}} t_x \cos(\phi_p) E_0 \cos(\phi_a), \qquad \mathcal{E}_{ty} = |\sqrt{\frac{k_{zy,N}}{k_{zy,0}}} t_y \sin(\phi_p) E_0 \sin(\phi_a). \tag{2.18}$$

It should be noted that using polarizer and analyzer will force fields to interfere and we will not have orthogonal non-intteracting fields for intensity due to the analyzer that forces field to pass through a polarization angle. Therefore, T and R cannot be decoupled and broken down to x and y components and are found to be

$$R = |\mathcal{E}_{rx} - \mathcal{E}_{ry}|^2, \qquad T = |\mathcal{E}_{tx} + \mathcal{E}_{ty}|^2. \tag{2.19}$$

The minus sign in R in Equation 2.19 is used to make right-handed reference frame consistent with the input (reflection is backpropagating with respect to the input field). The polarization ellipse can be used to fit to ellipse equation to derive the analytical parameters such as ellipticity, using the calculated $\mathcal{E}$ for both transmitted and reflected

light.

$$\frac{\mathcal{E}_x}{E_{0x}^2} + \frac{\mathcal{E}_y}{E_{0y}^2} - 2\frac{\mathcal{E}_x \mathcal{E}_y}{E_{0x} E_{0y}} \cos\delta = \sin^2\delta, \tag{2.20}$$

where δ is the phase difference between y and x components of electric field ($\mathcal{E}_y$ and $\mathcal{E}_x$), $\delta = \angle\mathcal{E}_y - \angle\mathcal{E}_x$ and E_{0x} and E_{0y} are the half diameters of the polarization ellipse.

2.3. 4×4 Transfer Matrix Method for multilayers with non-diagonal dielectric tensor

For some multilayer systems that have thin films where the dielectric tensor is non-diagonal, solving 2×2 TMM twice with methodology outlined in Section 2.1 will not be applicable due to the fact that the fields in two orthogonal in-plane directions couple through the off-diagonal dielectric tensor elements. Hence, the two 2×2 TMM solutions are not decoupled. This is the case when two birefringent materials are rotated with respect to each other and their crystal directions are not aligned. For the purpose of this thesis, two birefringent layers with rotated frames are considered. In order to solve this problem, a general 4×4 TMM method is required. The solution is implemented from the work of Abdulhalim [59]. The coordinate system that is of main importance is called Lab coordinate system (LCS) ($\hat{x}o\hat{y}o\hat{z}$) which is defined parallel to the crystal directions of the birefringent material in the bottom (Figure 2.3a) with wavevector of incident light as $\vec{k}$ = (k_x, k_y, k_z). Then, a calculation coordinate system (CCS) is defined ($\hat{x}'o\hat{y}'o\hat{z}'$) such that $\vec{k}'$ = (k'_x, 0, k'_z), hence polarization in CCS is $\phi'_p = 0$. All the layers will be rotated to CCS and once the fields are calculated, they will be rotated back to the LCS. The dielectric permittivity of the top layer is rotated by $\alpha_1 = \phi_p - \delta$ where δ is the rotation of top birefringent layer with respect to the bottom one (Figure 2.3a). The

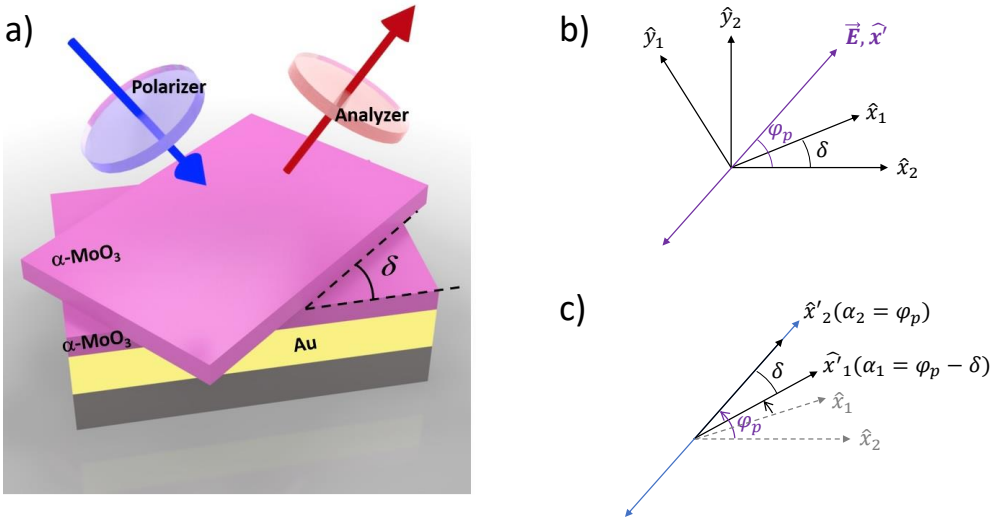

Figure 2.3. (a) Twisted orthorhombic vdW heterostructures with orthorhombic α-MoO_3. (b) Illustration of crystal axes for each twisted layer including top layer $\hat{x}_1 o \hat{y}_1 o \hat{z}_1$ and bottom layer $\hat{x}_2 o \hat{y}_2 o \hat{z}_2$, lab coordinate system (LCS) $\hat{x} o \hat{y} o \hat{z}$ and calculation coordinate system (CCS) $\hat{x}' o \hat{y}' o \hat{z}'$. (c) Illustration of the system after transforming to CCS with rotating the dielectric function of the top and bottom layer by α_1 and α_2 respectively to obtain $\hat{x}'_1 o \hat{y}'_1 o \hat{z}'_1$ and $\hat{x}'_2 o \hat{y}'_2 o \hat{z}'_2$.

dielectric tensor in the rotated frame can be rotated with rotation matrix R and thus, the dielectric tensor of the first (top) layer (Figure 2.3) can be calculated as,

$$\bar{\bar{\varepsilon}}'_1 = R(\alpha_1)\bar{\bar{\varepsilon}}_1 R^{-1}(\alpha_1), \tag{2.21}$$

$$R(\alpha_1) = \begin{bmatrix} \cos\alpha_1 & -\sin\alpha_1 & 0 \\ \sin\alpha_1 & \cos\alpha_1 & 0 \\ 0 & 0 & 1 \end{bmatrix}. \tag{2.22}$$

Note that $\bar{\bar{\varepsilon}}_1'$ is not diagonal anymore in CCS. For the bottom layer, the dielectric tensor is transformed to CCS by rotating it by $\alpha_2 = \phi_p$ using Equation 2.21. Any isotropic layer, or more specifically, any layer with in-plane isotropy will have its dielectric tensor intact. The general form of dielectric tensor for mth layer is

$$\bar{\bar{\varepsilon}}_m' = \begin{bmatrix} \varepsilon_{xx,m}' & \varepsilon_{xy,m}' & \varepsilon_{xz,m}' \\ \varepsilon_{yx,m}' & \varepsilon_{yy,m}' & \varepsilon_{yz,m}' \\ \varepsilon_{zx,m}' & \varepsilon_{zy,m}' & \varepsilon_{zz,m}' \end{bmatrix}. \tag{2.23}$$

The normalized in-plane wavevector (q_x) is the same in all layers, $q_x = k_x/(\omega/c) = \sin\phi_p$. Using this, a 4×1 field matrix (ψ', in CCS) and 4×4 matrix called Δ can be defined for each layer m,

$$\psi_m'^T = [\sqrt{\epsilon_0}E_x \qquad \sqrt{\mu_0}H_y \qquad \sqrt{\epsilon_0}E_y \qquad \sqrt{\epsilon_0}H_x]e^{ik_{z,m}z}, \qquad \frac{\partial}{\partial z}\psi = ik_0\Delta\psi, \tag{2.24}$$

where T in $\psi_m'^T$ stands for transpose of matrix ψ_m'. The determinant of Δ matrix gives the four eigenvalues for k_z. Defining $q_z = k_z/k_0$, the following equation can be derived from the determinant of Δ_m matrix for each layer m,

$$q_{z,m}^4 + aq_{z,m}^3 + bq_{z,m}^2 + cq_{z,m} + d = 0, \tag{2.25}$$

Out of the four solutions for q_z, two represent forward and two represent backward propagating waves. The solution of Equation 2.25 gives the dispersion relation. Some simplifications can be made in special cases; for normal incidence (which is the case in

this study), $a = c = 0$ in Equation 2.25 and can be solved easily for each layer m,

$$q_{z,m_{1,3}} = \pm\sqrt{\frac{-b + \sqrt{b^2 - 4d}}{2}}, \qquad q_{z,m_{2,4}} = \pm\sqrt{\frac{-b - \sqrt{b^2 - 4d}}{2}}. \tag{2.26}$$

Using Equation 2.26, the Δ matrix can be derived. Relying on the fact that $q_y = 0$ due to CCS,

$$\Delta_m = \begin{bmatrix} -\frac{q_{x,m}\varepsilon'_{zx,m}}{\varepsilon'_{zz,m}} & 1 - \frac{q_{x,m}^2}{\varepsilon'_{zz,m}} & -\frac{q_{xx,m}\varepsilon'_{zy,m}}{\varepsilon'_{zz,m}} & 0 \\ \varepsilon'_{xx,m} - \frac{\varepsilon'_{xz,m}\varepsilon'_{zx,m}}{\varepsilon'_{zz,m}} & -\frac{q_{x,m}\varepsilon'_{xz,m}}{\varepsilon'_{zz,m}} & \varepsilon'_{xy,m} - \frac{\varepsilon'_{xz,m}\varepsilon'_{zy,m}}{\varepsilon'_{zz,m}} & 0 \\ 0 & 0 & 0 & 1 \\ \varepsilon'_{yx,m} - \frac{\varepsilon'_{yz,m}\varepsilon'_{zx,m}}{\varepsilon'_{zz,m}} & -\frac{q_{x,m}\varepsilon'_{yz,m}}{\varepsilon'_{zz,m}} & \varepsilon'_{yy,m} - q_{x,m}^2 - \frac{\varepsilon'_{yz,m}\varepsilon'_{zy,m}}{\varepsilon'_{zz,m}} & 0 \end{bmatrix}. \tag{2.27}$$

For normal incidence, the partial transfer matrix (P'_m) can be derived as follows for each layer m,

$$P'_m = \begin{bmatrix} P'_{11} & P'_{12} & P'_{13} & P'_{14} \\ P'_{21} & P'_{22} & P'_{23} & P'_{24} \\ P'_{31} & P'_{32} & P'_{33} & P'_{34} \\ P'_{41} & P'_{42} & P'_{43} & P'_{44} \end{bmatrix}, \tag{2.28}$$

$$
\begin{aligned}
P'_{11} &= -f_{2,m} - f_{3,m}\Delta_{21,m}, \\
P'_{12} &= f_{1,m}\Delta_{21,m} + f_{4,m}, \\
P'_{13} &= -f_{3,m}\Delta_{23,m}, \\
P'_{14} &= f_{1,m}\Delta_{23,m}, \\
P'_{21} &= f_{1,m}(\Delta^2_{21,m} + \Delta_{23,m}\Delta_{41,m}) + f_{4,m}\Delta_{21,m}, \\
P'_{22} &= -f_{2,m} - f_{3,m}\Delta_{21,m}, \\
P'_{23} &= -f_{1,m}b\Delta_{23,m} + f_{4,m}, \\
P'_{24} &= -f_{3,m}\Delta_{23,m}, \\
P'_{31} &= -f_{3,m}\Delta_{41,m}, \\
P'_{32} &= f_{1,m}\Delta_{41,m}, \\
P'_{33} &= -f_{2,m} - f_{3,m}\Delta_{43,m}, \\
P'_{34} &= f_{1,m}\Delta_{43,m}, \\
P'_{41} &= -f_{1,m}b\Delta_{41,m} - f_{4,m}\Delta_{41,m}, \\
P'_{42} &= -f_{3,m}\Delta_{41,m}, \\
P'_{43} &= f_{1,m}(\Delta_{41,m}\Delta_{23,m} + \Delta^2_{43,m} + f_{4,m}\Delta_{43,m}), \\
P'_{44} &= -f_{2,m} - f_{3,m}\Delta_{43,m},
\end{aligned}
\tag{2.29}
$$

where b is the coefficient from Equation 2.26, Δ_{ij} is the ith row and jth column element of matrix Δ, and $f_{1,m}$, $f_{2,m}$, $f_{3,m}$ and $f_{4,m}$ for the mth layer are calculated as follows,

$$
\begin{aligned}
f_{1,m} &= -i\frac{q_{z,m_1}\sin(k_0 t_m q_{z,m_2}) - q_{z,m_2}\sin(k_0 t_m q_{z,m_1})}{q_{z,m_1}^3 q_{z,m_2} - q_{z,m_2}^3 q_{z,m_1}},\\
f_{2,m} &= \frac{q_{z,m_2}^2\cos(k_0 t_m q_{z,m_1}) - q_{z,m_1}^2\cos(k_0 t_m q_{z,m_2})}{q_{z,m_1}^2 - q_{z,m_2}^2},\\
f_{3,m} &= \frac{\cos(k_0 t_m q_{z,m_2}) - \cos(k_0 t_m q_{z,m_1})}{q_{z,m_1}^2 - q_{z,m_2}^2},\\
f_{4,m} &= -i\frac{q_{z,m_1}^3\sin(k_0 t_m q_{z,m_2}) - q_{z,m_2}^3\sin(k_0 t_m q_{z,m_1})}{q_{z,m_1}^3 q_{z,m_2} - q_{z,m_2}^3 q_{z,m_1}},
\end{aligned}
\tag{2.30}
$$

where t_m is the thickness of the mth layer. After calculating P'_m matrices, the transfer matrix of each layer can be built as $P_m = P'_m e^{ik_0 t_m \Delta_m}$. Using the partial transfer matrices of all layers m = 1,2,..., N (from top to bottom), the full transfer matrix of the N-layer system can be calculated as $P = P_N ... P_2 P_1$ which relates the input and output fields as follows,

$$\psi_t = P(\psi_i + \psi_r), \tag{2.31}$$

where ψ_t, ψ_i and ψ_r are respectively the transmitted, incident and reflected fields defined similar to Equation 2.24. Equation 2.31 gives two 2×2 matrices where one relates input and reflected fields and the other relates the input and transmitted fields. Defining $\psi_j(j,z) = \mathcal{E}'_j(z)e^{iq_j j}, j = x', y'$ in CCS similar to Equation 2.3, these two matrices are,

$$\begin{bmatrix} \mathcal{E}'_{rx} \\ \mathcal{E}'_{ry} \end{bmatrix} = \begin{bmatrix} r_{xx} & r_{xy} \\ r_{yx} & r_{yy} \end{bmatrix} \begin{bmatrix} \mathcal{E}'_{ix} \\ \mathcal{E}'_{iy} \end{bmatrix}, \tag{2.32}$$

$$\begin{bmatrix} \mathcal{E}'_{tx} \\ \mathcal{E}'_{ty} \end{bmatrix} = \begin{bmatrix} t_{xx} & t_{xy} \\ t_{yx} & t_{yy} \end{bmatrix} \begin{bmatrix} \mathcal{E}'_{ix} \\ \mathcal{E}'_{iy} \end{bmatrix}. \tag{2.33}$$

Note that $\mathcal{E}'_{rx} = r_{xx}\mathcal{E}'_{ix}$ since $\mathcal{E}'_{iy} = 0$ in CCS. The reflection and transmission matrices are calculated as,

$$r = \frac{1}{a_4a_6 - a_2a_8} \begin{bmatrix} a_1a_8 - a_4a_5 & a_3a_8 - a_4a_7 \\ a_2a_5 - a_1a_6 & a_2a_7 - a_6a_3 \end{bmatrix}, \tag{2.34}$$

$$t = \begin{bmatrix} b_1 + b_2r_{xx} + b_3r_{yx} & b_4 + b_2r_{xy} + b_3r_{yy} \\ b_5 + b_6r_{xx} + b_7r_{yx} & b_8 + b_6r_{xy} + b_7r_{yy} \end{bmatrix}. \tag{2.35}$$

For normal incidence (q = 0), $a_2 = a_1$, $a_4 = a_3$, $a_6 = a_5$ and $a_8 = a_7$,

$$\begin{aligned} a_1 &= n_i(n_tP_{12} - P_{22}) + (n_tP_{11} - P_{21}), \\ a_3 &= n_tP_{13} - P_{23} + n_i(n_tP_{14} - P_{24}), \\ a_5 &= n_i(n_tP_{32} - P_{42}) + (n_tP_{13} - P_{41}), \\ a_7 &= n_tP_{33} - P_{43} + n_i(n_tP_{34} - P_{44}), \end{aligned} \tag{2.36}$$

$$
\begin{aligned}
b_1 &= (n_i P_{22} + P_{21})/n_t, \\
b_2 &= (n_i P_{22} - P_{21})/n_t, \\
b_3 &= (P_{23} - n_i P_{24})/n_t, \\
b_4 &= (P_{23} + n_i P_{24})/n_t, \\
b_5 &= n_i P_{32} + P_{31}, \\
b_6 &= n_i P_{32} - P_{31}, \\
b_7 &= (P_{33} - n_i P_{34}), \\
b_7 &= (P_{33} + n_i P_{34}),
\end{aligned}
\tag{2.37}
$$

where P_{ij} are the elements of the partial transfer matrix (P), n_i and n_t are respectively the refractive indices of the incident and transmitted media, which are air. Once the electric fields are calculated in CCS, they can be transformed back into the LCS with $-\phi_p$ rotation,

$$
\begin{bmatrix} \mathcal{E}_{rx} \\ \mathcal{E}_{ry} \end{bmatrix} = \begin{bmatrix} \cos(-\phi_p) & -\sin(-\phi_p) \\ \sin(-\phi_p) & \cos(-\phi_p) \end{bmatrix} \begin{bmatrix} \mathcal{E}'_{rx} \\ \mathcal{E}'_{ry} \end{bmatrix}, \tag{2.38}
$$

$$
\begin{bmatrix} \mathcal{E}_{tx} \\ \mathcal{E}_{ty} \end{bmatrix} = \begin{bmatrix} \cos(-\phi_p) & -\sin(-\phi_p) \\ \sin(-\phi_p) & \cos(-\phi_p) \end{bmatrix} \begin{bmatrix} \mathcal{E}'_{tx} \\ \mathcal{E}'_{ty} \end{bmatrix}. \tag{2.39}
$$

These fields now can be used to calculate polarization ellipse as outlined in Section 2.2. A 4×4 TMM method has also been developed by Passler et. al. [60] which can be downloaded for free and is used for monoclinic material β-Ga_2O_3.

2.4. Effective medium theory

Modeling patterned layers can be often challenging in numerical methods. Effective medium theory (EMT) rectifies this issue by proposing an approximate dielectric function. For patterns that are simple in shape, such as circles, disks and gratings and cylinders, there is a route to achieve a reliable dielectric tensor model if the pattern periodicity of the layer is very small compared to the wavelength of interest (a rule of thumb is more than 10 times smaller). Applying Maxwell Garnett (MG) mixing formula it is possible to obtain a homogenized effective dielectric tensor that captures the optical behavior of the patterned layer [61, 62]. The generalized version of MG mixing formula for calculation of dielectric function ε_{eff} in direction $\hat{j}$ is,

$$\varepsilon_{eff,j} = \varepsilon_h + f\frac{\varepsilon_h(\varepsilon_i - \varepsilon_h)}{\varepsilon_h + (1-f)L_j(\varepsilon_i - \varepsilon_h)}, \tag{2.40}$$

where ε_h and ε_i are respectively the dielectric functions of the host medium and inclusion. For example, in a metal grating (ϵ_m) pattern on a sample, the host medium is air with $\varepsilon_h = 1$ and the inclusion is the metal dielectric function $\varepsilon_i = \varepsilon_m$. In Equation 2.40, f is the volume filling ratio of the inclusion to the host, $f = Vol_{\varepsilon_h}/Vol_{\varepsilon_i}$ and L_j is depolarization factor that takes the shape of the inclusion into account and satisfies the condition $L_x + L_y + L_z = 1$ [63]. The condition of depolarization factor sets restraints in the complexity of the inclusions that can be modeled. Some examples of L values for different simple inclusion shapes are provided in Figure 2.4.

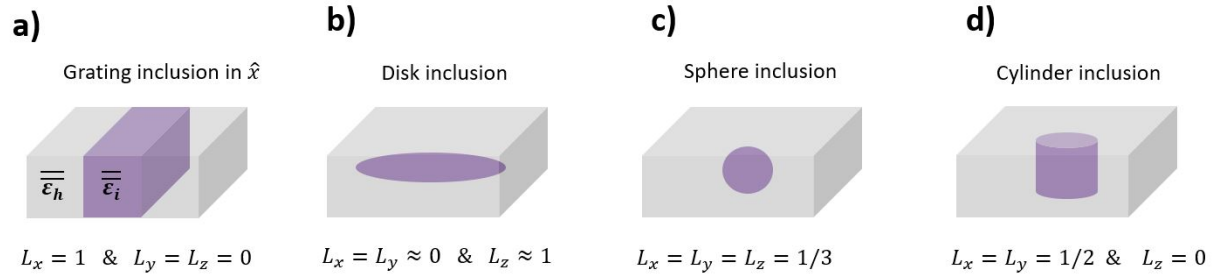

Figure 2.4. Depolarization factor example for some simple inclusions in host material.

2.5. Oscillator model for coupled systems

One of the strong tools to study the coupling of modes in photonic systems is the coupled oscillator model. This model provides an easy approach by fitting the spectra with Lorentz oscillators to the measured and/or simulated spectra to obtain the Rabi frequency which contains coupling strength. Each ocillator can be modeled with a Lorentz equation and they can be coupled using coupling constant as demonstrated in Figures 2.5a and b which represent an uncoupled mode and two interacting modes, respectively.

The oscillator model in the frequency domain (ω) for the mth mode (N total oscillators) in the system can be described as [64, 65, 66, 67],

$$\ddot{x}_m(t)^2 + i\gamma_m \dot{x}_m(t) + \omega_{o,m}^2 x_m(t) - \sum_{m=0}^{N} \Omega_{nm}^2 x_n(t) = F(t), \qquad n \neq m, \tag{2.41}$$

where x_m represents the amplitude and phase of the mth oscillator, γ and ω_0 are respectively the broadening factor and resonance frequency, $\Omega = 2g$ and F respectively represent the coupling strength between oscillators m and n and driving force in the

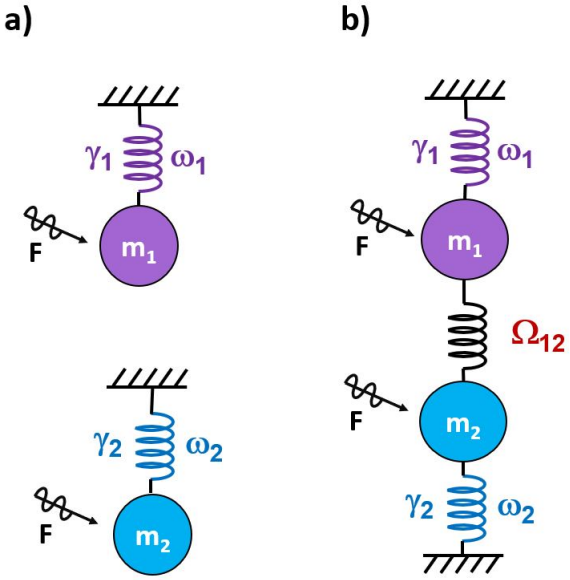

Figure 2.5. Schematically illustrated (a) two independent oscillators and (b) two coupled oscillators.

oscillator configuration. x_n is the amplitude of the other oscillator(s) coupled to the oscillator m. Since the driving force is electromagnetic, in steady state, it has oscillatory form of $\mathcal{R}e[F\exp(-i\omega t)] = F\cos(i\omega t)$. Hence, the solutions have similar form of $x(t) = \mathcal{R}e[X(\omega)\exp(-i\omega t)]$, where $X(\omega)$ is the Fourier transform of $x(t)$. The matrix formulation in frequency domain for the system of interacting modes are,

$$\begin{bmatrix} \widehat{O_1} & \Omega_{12}^2 & \cdots & \Omega_{1N}^2 \\ \Omega_{21}^2 & \widehat{O_2} & \cdots & \Omega_{2N}^2 \\ \vdots & \vdots & \ddots & \vdots \\ \Omega_{N1}^2 & \Omega_{N2}^2 & \cdots & \widehat{O_N} \end{bmatrix} \begin{bmatrix} X_1 \\ X_2 \\ X_3 \\ X_4 \end{bmatrix} = \begin{bmatrix} F_1 \\ F_2 \\ F_3 \\ F_4 \end{bmatrix}, \tag{2.42}$$

$$\widehat{O_m} = (-i\omega)^2 - i\omega\gamma_m + \omega_m^2. \tag{2.43}$$

In Equation 2.42, Ω_{mn} represents the coupling (Rabi) frequency (strength) between the modes m and n. Solving this system of equations within the frequency range of interest for $X(\omega)$, the spectral absorption $(\alpha(\omega))$ can be calculated as

$$\alpha(\omega) \propto \frac{\omega}{\varepsilon_0 E_0 c} \mathcal{I}m[\sum_{m=0}^{N} F_m X_m]. \tag{2.44}$$

In order to fit this model to the simulation and experimental absorption results, first, each mode is separately fitted to an oscillator, without coupling frequency ($\Omega_{mn} = 0$). Then, the coupled system with the interacting mode is fitted by a proper value of Ω_{mn}, keeping all other parameters the same as their uncoupled values to extract the Rabi frequency.

2.6. Material modeling and dispersion

One of the approaches used in this report is the optical modelling of the novel anisotropic vdW materials and relying on matching their dispersion with the existing literature. Material models are mathematical equations that capture the optical properties of the material of interest, i.e. dielectic tensor, and generate accurate optical responses once incorporated into TMM or FDTD simulations.

2.6.1. Material models

Here, we introduce the material models that will be tailored to simulation of materials throughout this study.

Cauchy model. For materials that have negligible loss in any frequency band, Cauchy model [68] can be used which assumes a purely real refractive index (hence,

purely real dielectric function). This model is used predominantly to model transparent materials in VIS whose bandgaps lie in ultra-viole (UV), such as glass. The refractive index is derived as

$$n = a + \frac{b}{\lambda_{nm}^2} + \frac{c}{\lambda_{nm}^4} + O(\lambda), \tag{2.45}$$

where the constants a, b and c are taken by fitting to the ellipsometer data. λ_{nm} is written to emphasize that conventionally the constants are found for wavelength in units of nanometers. While it is possible to fit higher order constants to this equation ($O(\lambda)$), practically, two or three constants produce very high accuracy and are sufficient. Dielectric function can be obtained using n from Equation 2.45 as $\varepsilon = n^2$ which can be driven for any crystal direction to form the components of the corresponding material's dielectric tensor $\bar{\bar{\varepsilon}}$.

Drude and Lorentz models. In order to model the polaritons in thin vdw materials (2D limit) such as borophene, phenominalogically adopted Kramers-Kronig relations are used [69]. For PPs, since it occurs in metal-like materials with high carrier density, this phenomenon is modeled macroscopically by semi-classical Drude model which treats electrons as free carriers [70]. The Drude model is used to derive the diagonal components of the conductivity tensor ($\bar{\bar{\sigma}}$),

$$\sigma_{jj} = \frac{iD_j}{\pi(\omega + i/\tau_j)} \qquad D_j = \frac{\pi e^2 n}{m_j}. \tag{2.46}$$

In Equation 2.46 e, n, ω and τ represent respectively the electron charge, 2D density of electrons, frequency of excitation ($\omega = 2\pi c/\lambda$) and mean free time of electrons. D_j and

m_j stand for the Drude weight and effective electron mass in direction $\hat{j}$. The dielectric function can be derived from Equation 2.46 as

$$\varepsilon_{jj} = \varepsilon_\infty + \frac{i\sigma_{jj}}{\varepsilon_0 \omega d}, \tag{2.47}$$

where d is the thickness of the plasmonic layer. Substituting Equation 2.46 in Equation 2.47 followed by some basic algebra gives the dielectric function of the plasmonic material as

$$\varepsilon_{jj} = [\varepsilon_\infty - \frac{e^2 n}{m_j \varepsilon_0 d(\omega^2 + 1/\tau^2)}] + i[\frac{e^2 n/\tau}{m_j \varepsilon_0 d\omega(\omega^2 + 1/\tau^2)}]. \tag{2.48}$$

For PhPs and OPhs in materials with phononic response such as hBN and α-MoO_3, Lorentz oscillator model is used [71]. In IR, many materials demonstrate strong polarizability that results in lattice vibration peaks which is the phenomenon responsible for Raman spectroscopy. In mid-IR, some materials have phonon resonances that cause hyperbolicity. Hyperbolicity [13] is an extreme form of birefringence where one or more of the crystal axes have a negative real part of the dielectric function, whilst the others are positive. Based on lattice anisotropy, for certain crystal directions $\hat{j}$ the real part of the dielectric function can be negative in a band of frequency labeled RS band. These RS bands are bracketed by longitudinal (LO) and transverse (TO) optic phonons in each direction. The zero crossing of the real part of the permittivity in these materials marks a significant increase in loss which is where the OPhs are located. The dielectric function of the

material in each crystal direction is a made up of of Lorentz oscilltors,

$$\varepsilon_{jj} = \varepsilon_{\infty,j} \prod_{m=0}^{n} \left(\frac{\omega_{LO,jm}^2 - \omega^2 - i\omega\Gamma_j}{\omega_{TO,jm}^2 - \omega^2 - i\omega\Gamma_j}\right), \qquad j = x, y, z. \tag{2.49}$$

In Equation 2.49, $\varepsilon_{\infty,j}$ and Γ_j respectively stand for the high frequency permittivity and phonon damping (broadening factor of Lorentz function), while $\omega_{LO,j}$ and $\omega_{TO,j}$ represent LO and TO phonon frequencies that bracket each RS band along the corresponding direction $\hat{j}$. n is the number of Lorentz oscillator terms used for the dielectric function of each direction.

2.6.2. Material dispersion

Dispersion relation, i.e. the relation between ω and k, is a key fingerprint of the modes in a system and it provides insight to many characteristics of an optical system, such as mode frequency, mode momentum (wavenumber) as well as the number of modes and their group velocities at the point of operation. Finding the dispersion relation of polaritons is specifically important since they have high momenta and their dispersion curves are not linear. The developed TMM simulation and material models can be used to obtain the dispersion of the polariton modes. The easiest method to obtain the dispersion relation is to calculate the reflectance coefficient r_j using Equation 2.10, where the parallel component of the wavevector (q) is not calculated using Equation 2.4 and is instead assumed to be a variable. Consequently, $r_j(\omega, q)$ will be a function of two variables. The poles of the imaginary part of r_j will give the dispersion line of the system. In order to visualize the dispersion, it is common practice to plot a false color

image plot of r_j as a function of ω and k that clearly gives all of the possible modes in the system, including PPs, PhPs and light lines [72].

CHAPTER 3

Birefringent vdW materials for polarization-dependent photonics in VIS/NIR

This chapter is mostly adapted from a submitted manuscript and the following published articles:

- Abedini Dereshgi, S., Liu, Z. and Aydin, K. "Anisotropic localized surface plasmons in borophene." *Optics Express*, 28 (11), pp.16725-16739 (2020) [53].
- Wei, C., Abedini Dereshgi, S., Song, X., Murthy, A., Dravid, V.P., Cao, T. and Aydin, K. "Polarization Reflector/Color Filter at Visible Frequencies via Anisotropic α-MoO_3." *Advanced Optical Materials*, 11(1), pp.2000088 (2020) [56].

3.1. Chapter 3 highlights

In this chapter emerging vdW materials, 2D metal borophene and transparent α-MoO_3 are investigated as strong candidates for polarization-dependent on-chip photonics. We first present a theoretical study on the plasmonic response of borophene, a monolayer 2D material that is predicted to exhibit metallic response and anisotropic plasmonic behavior in visible wavelengths. We investigate plasmonic properties of borophene monolayers as well as borophene nanoribbons and nanopatches where polarization-sensitive absorption values in the order of 50% is obtained with monolayer borophene. It is demonstrated that by adding a metal layer, this absorption can be enhanced to

100%. We also examine giant dichroism in monolayer borophene which can be tuned passively (patterning) and actively (electrostatic gating) and our simulations yield 20% reflected light with significant polarization rotation.

Anisotropic optical properties of α-MoO_3 in the visible frequency range have not attracted the deserved scrutiny. Here, α-MoO_3 is investigated as an optical material at the visible frequency (400-750 nm), which exhibits a polarization-dependent refractive index due to the anisotropic crystal structure. Depolarization characteristics of orthorhombic α-MoO_3 is investigated in detail in VIS. Using polarizers and analyzers, we demonstrate that α-MoO_3 has negligible loss and birefringence values as high as 0.15 and 0.12 at 532 nm and 633 nm, respectively, is achievable. With such a high birefringence, we demonstrate quarter- and half-wave plate actions for a 1400 nm α-MoO_3 flake at green (532 nm) and red (633 nm) wavelengths and we report polarizability as high as 90%. Furthermore, we investigate a system of double α-MoO_3 heterostructure layer that provides the possibility of tuning polarization as a function of rotation angle between the α-MoO_3 layers. As a proof of concept, polarization-sensitive photonic devices including polarization reflectors and polarization color filters are designed and realized by constructing metal–insulator–metal FP cavities. It is observed that resonance frequencies for designed transmission and reflection filters change up to 25 nm with incident polarization which stems from the polarization-dependent complex refractive indices of α-MoO_3. The largest contrasts are observed for two orthogonal polarization states parallel to the two orthogonal in-plane crystal directions.

These findings reveal the potential of borophene and α-MoO_3 in the manipulation of phase, amplitude and polarization of light in VIS and NIR.

3.2. Birefringent metamaterial: Anisotropic plasmons in borophene for polarization-dependent photonics

3.2.1. Motivation

As argued in Chapter 1, the recent advances in 2D materials signal a bright future for the next generation, compact electronic and photonic devices [73]. With reduced dimensionality and material thicknesses reaching down to atomic and molecular levels, 2D materials provide access to unique electrical, optical and mechanical properties that can enable compact, sub-diffraction limit and yet efficient devices. Another landmark phenomenon that plays a crucial role in the trend of smaller devices is plasmonics. Conventional plasmonic materials are usually noble metals like silver and gold, and literature around these plasmonic materials is vast. Plasmonic materials are also utilized in designing metamaterials and metasurfaces that could modify the amplitude, phase and polarization of light [74]. Metasurfaces and metamaterials find applications in wide range of areas including absorbers [26, 75], photodetectors [76, 30], solar cells [77], retarders [78], waveguides [79] and lenses [80], and negative refraction and cloaking [81]. Graphene was the first 2D material to be discovered and investigated in detail. Despite its monolayer thickness, theoretical and experimental studies in the recent years have unearthed the capability of graphene in supporting plasmons and interacting strongly with light. Initial demonstrations included, but were not limited to, nanostructured graphene (i.e. nanoribbons) which supports localized and propagating surface plasmon polaritons (LSPP and PSPP) with an exceptional tunability of plasmonic response with different doping methods (i.e. electrical, chemical and optical) [13, 82]. Despite having

access to 2D semi-metals (e.g. Graphene), insulators (e.g. hBN) and semiconductors (e.g. MoS_2), a 2D metal has been elusive. Recently, borophene was introduced as a 2D material that supports plasmons in the visible and C-band ranges of electromagnetic spectrum with high electron density and hence is called a 2D metal even though in bulk form it is a semiconductor [83, 84]. After initial demonstration of experimental growth of borophene on Ag (111) substrate [85, 86], optical and electronic properties of borophene deserves more in-depth investigation. The high electron density and strong anisotropy of borophene has garnered attention as an outstanding 2D material that has potential to excite PSPPs and LSPPs [87, 88]. Moreover, owing to its highly dispersive optical response in different in-plane crystallographic directions, it can give rise to several interesting physical phenomena. Similar to black phosphorus (BP) [89], borophene can support hyperbolic response and anisotropic plasmons and canalization. Unlike BP which supports LSPPs in mid-IR, borophene supports plasmons in the visible range thanks to its high carrier density compared to BP [70, 84]. Here, we theoretically investigate borophene as a birfringent plasmonic material for VIS and NIR. Borophene and its heterostructures are reported to only be grown on metal films, specifically Ag and Au using molecular beam epitaxy (MBE) [90, 91, 92]. However, recently scientists have reported the growth of free-standing borophene with lateral dimensions as large as 1.2 μm by liquid-phase synthesis of freestanding borophene sheets via sonochemical exfoliation [93]. Hence, this study provides a path toward the integration of this novel 2D metal to on-chip photonic applications in VIS and C-band of NIR.

3.2.2. Optical model of borophene

In the 2D limit, boron atoms form bonds in a hybrid lattice of hexagonal and triangle distributions. Theoretical calculations predict several polymorphs of borophene; however, only three phases α, β_{12} and χ_3 have attracted scrutiny. It was also reported that borophene allotropes are unstable in free-standing form and a distribution of vacancies is required to make it experimentally feasible. Growth of borophene using MBE on Ag (111) surface alleviates the stability issue since Ag passivates the sp^2 hybridization. Therefore, α-phase which lacks vacancies (like zigzag and armchair directions of BP) is not experimentally stable. Of the mentioned three phases, α and χ_3 have large anisotropy in their crystal directions which are responsible for the anisotropy in optical response of borophene [83, 85]. As discussed in 2, borophene is a metal and can be modeled by Equation 2.46. The parameters predicted in [84] and [85] are summarized in Table 3.1 which can be used to obtain the diagonal components of the dielectric tensor of borophene using Equations 2.47 and 2.47. To the best of our knowledge, empirical value for τ is not reported in literature yet and only a range is estimated. This stems from the fact that currently, it is impossible to isolate borophene monolayers from underlying silver substrates[84] and is not yet experimentally characterized from the recently grown isolated flakes [93]. Nonetheless, it only affects the resonance strength while the resonance wavelengths are the same and we use 60 fs in this paper.

α-borophene is schematically illustrated in Figure 3.1a with marked critical directions. Since we aim to theoretically investigate the anisotropic nature of plasmons here, we chose α-phase which possesses the strongest anisotropy and highest density of electrons. The dispersion relation of α-borophene is calculated in Figure 3.1b. The atomic crystal

Table 3.1. Values used for the Drude model of borophene, reported in [84, 85].

	α -borophene	**β_{12}-borophene**
m_x	$1.4m_0$	$1.4m_0$
m_y	$5.2m_0$	$3.4m_0$
τ (fs)	$10 \sim 65$	$10 \sim 65$
d (nm)	0.3	0.3
n (m^{-2})	4.3×10^{19}	3.3×10^{19}
ε_∞	11	11

and dispersion relation of the χ_3 phase is also provided in Figures 3.1c and d. Figures 3.2a and b demonstrate the dielectric function of borophene in $\hat{x}$ and $\hat{y}$ directions. All the upcoming discussions are applicable for χ_3 as well and hereafter, α-borophene is used in this study.

Figure 3.1b demonstrates the dispersion relation for α-borophene (dotted lines) in two different crystallographic directions, $\hat{x}$ and $\hat{y}$, where $\hat{x}$ direction is chosen to be the one with higher conductivity with Drude parameters taken from those reported by Huang et al. and Mannix et al. [84, 85]. Moreover, the 2DEG counterpart which is estimated in the work of Huang et al. is also provided for comparison. The dispersion relation infers that our calculated dispersion is almost identical to the one reported by Huang et al.; as a result, our model successfully mimics the optical characteristics of first-principle calculations of borophene [84]. It is also evident from 3.1b that the accessible wavelengths for LSPP resonance of borophene reach the visible range.

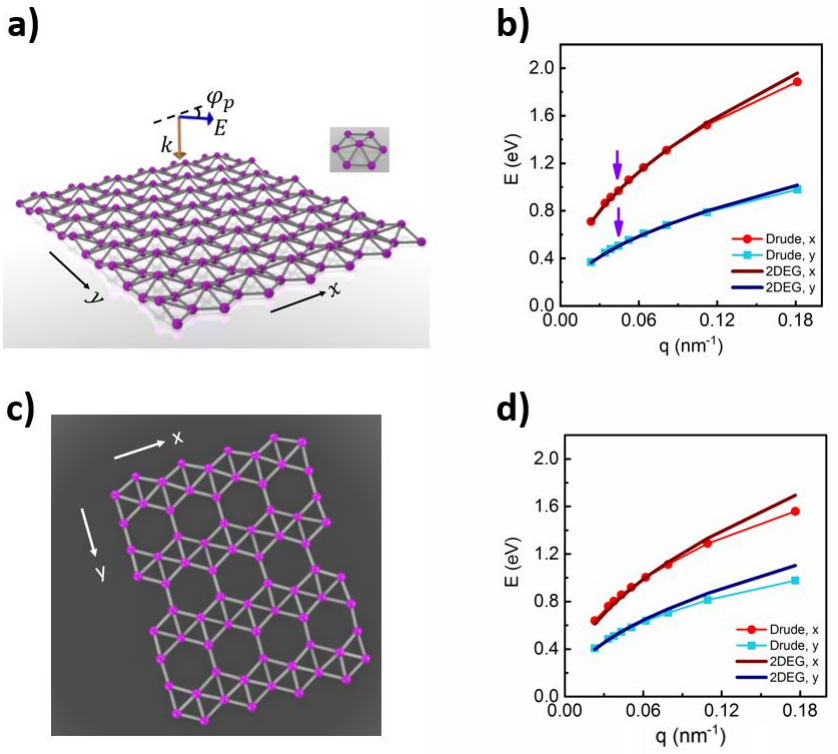

Figure 3.1. Schematic of α-borophene monolayer under impinging light, (b) dispersion relation of free-standing α-borophene in $\hat{x}$ and $\hat{y}$ directions (dotted lines) and their respective 2DEG model for comparison. (c) and (d) same as (a0 and (b) for χ_3-borophene.

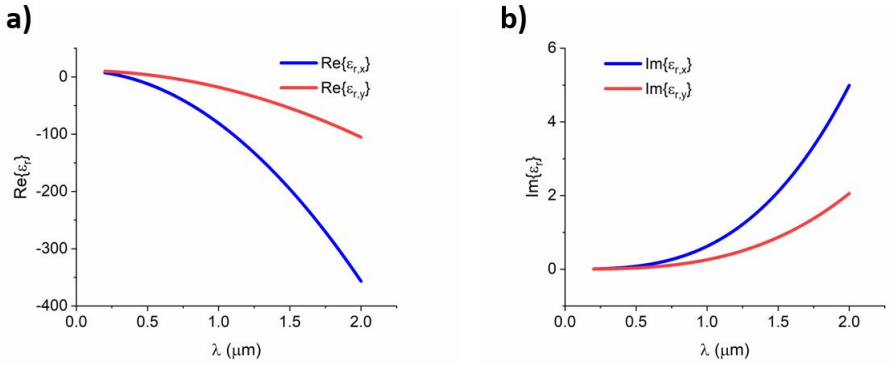

Figure 3.2. (a) Real and (b) imaginary parts of permittivity for a monolayer α-phase borophene in $\hat{x}$ and $\hat{y}$ directions.

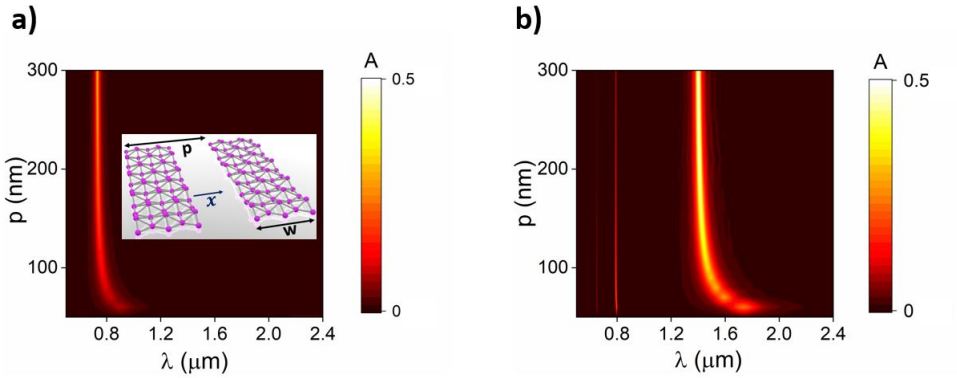

Figure 3.3. Effect of periodicity (p) on absorption (A) versus wavelength (λ) for a free-standing monolayer borophene nanoribbon with w= 50 nm in (a) $\hat{x}$ direction and (b) $\hat{y}$ direction. The arrows in Figure 3.1 (b) represent the resonances in the large periodicity limit of panels (a) and (b) and the discussed parameters for $\hat{x}$ direction are illustrated in the inset of (a).

The simulation of dispersion using TMM method is discussed in Chapter 2. The dispersion here is also calculated using FDTD full-wave simulations. In order to calculate the dispersion relation with FDTD, a free-standing borophene sheet was used in simulations where a planewave is impinging onto the ribbon arrays with polarization perpendicular to the ribbons for each direction ($\hat{x}$ and $\hat{y}$) separately, in order to provide the high momentum required for plasmonic excitation. Two examples for each of the two anisotropic directions for w = 50 nm are plotted in Figure 3.3.

In the plots of Figure 3.3, the resonance frequency remains unaltered due to the suppression of coupling between neighboring ribbons when the periodicity (p) is approximately an order of magnitude larger than w. In order to access the wave-vector values (q) through the selected w values, Fabry-Perot analysis is used. When the ribbon length is finite, electrons (i.e. excited plasmons) oscillate and back-scatter from the edges of the ribbon. Assuming that the ribbon is homogeneous, standing wave patterns

will form that correspond to LSPPs, which are described by $2qw + 2\phi_R = 2n\pi$. In this equation, ϕ_R is the phase picked up through reflection from the edges and n is the mode number. Following the discussion by Nikitin et al. for graphene, an anomalous phase of $\phi_R = -0.75\pi$ is chosen [94], which yields $q = 0.75\pi/w$. The dispersion (dotted lines) is illustrated in Figure 3.1b. The calculated dispersion is also compared to the 2DEG model (solid lines) defined as $\omega = (\sigma e^2 q/2m_j\varepsilon_0)^{0.5}$ which is used to fit to ab-initio calculated dispersion in [84]. Each two sets of dispersion curves are almost equivalent except for large wavevector values (i.e. small ribbon width) which is attributed to inhomogeneous doping in the edges of the ribbon and strong interaction of neighboring ribbons [94]. It is also evident from Figure 3.1b that there exists strong anisotropy in the plasmonic response of borophene. Moreover, Figure 3.3a infers that as the periodicity increases, the interaction between the ribbons gets weaker, the absorption peak blueshifts and the peak value of absorption decreases. This reduction in absorption is due to smaller surface coverage of borophene. This discussion is also valid for y direction illustrated in Figure 3.3b. In this figure, the narrow line at 0.8 μm is the higher order mode LSPP resonance. After assuring that the developed optical model is reliable, it is incorporated to the FDTD software and TMM code to analyze the farfield optical response of borophene. More details on the relation between Drude variables and the optical response of borophene is provided in Appendix A.1.

3.2.3. Anisotropic plasmons

In order to investigate LSPP resonances in borophene further, the effect of ribbon width on absorption is studied where borophene ribbon is placed on an SiO_2 substrate. Figure 3.4a (b) illustrates reflectance versus the waveength and ribbon width in $\hat{x}$ ($\hat{y}$) direction when the periodicity is kept constant at p = 100 nm. As the width of the ribbon (w) increases, the supported LSPPs are realized in longer wavelengths which is expected, and the reflectance peak broadens as a result of the increased optical losses at longer wavelengths [70]. Like Figure 3.3b the higher order plasmonic modes are discernable in Figures 3.4a and b. The spatial electric field distribution data are summarized in Figures 3.4c-e. Figure 3.4c (d) illustrates the real part of the electric field, $\mathcal{E}_x$ ($\mathcal{E}_z$) in a xz cross section for a ribbon with w = 50 nm and p = 100 nm at its corresponding LSPP resonance wavelength, 970 nm. An important implication from the electric field pattern of Figure 3.4c is that only the even modes are accessible for LSPP resonances [94]. This figure also vindicates high field enhancement and localization. Figure 3.4e depicts the total electric field intensity in xz cross section which shows a field intensity enhancement of approximately four orders of magnitude.

In order to shed light on anisotropic LSPPs in borophene, we elaborate on direction-dependent extinction spectra. We calculate absorption of a 2D square patch pattern of borophene on a SiO_2 substrate (Figure 3.5a) while the polarization angle of the impinging light (ϕ_p) is chosen to be 0°, 45° and 90°. The polarization angle is defined with respect to $\hat{x}$ axis. The geometric values are set as w = 30 nm and p = 60 nm. Figure 3.5b shows the absorption in a borophene square patch for the mentioned three polarization values. For ϕ_p = 0°, there is 30% absorption around 1.75 µm which is

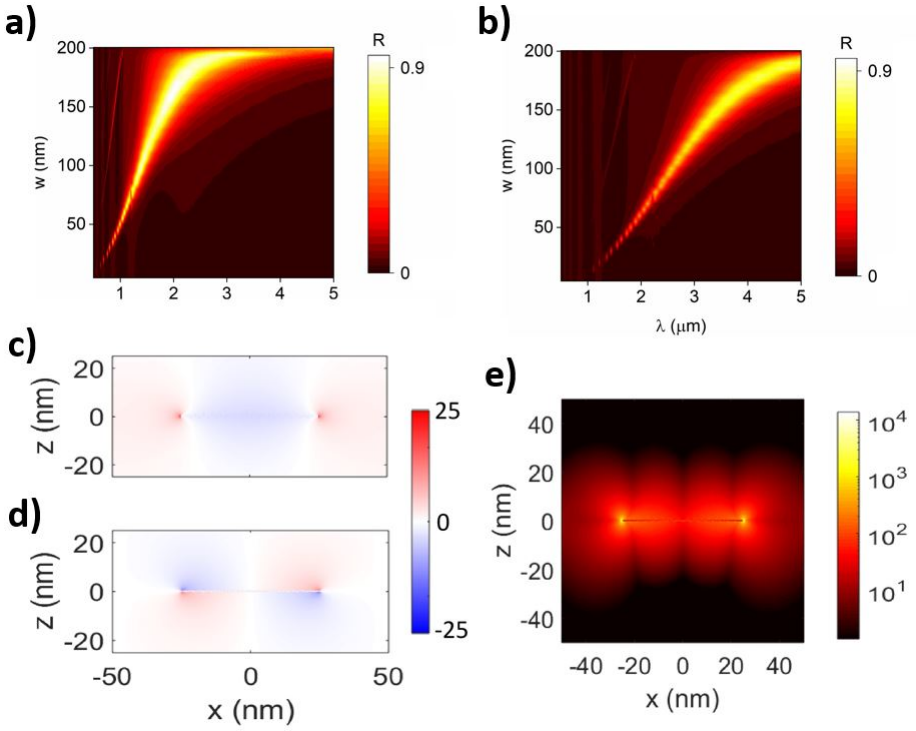

Figure 3.4. Reflection versus width and wavelength for a ribbon with periodicity p = 100 nm patterned in (a) $\hat{x}$ and (b) $\hat{y}$ on a SiO_2 substrate. Real part of (c) $\mathcal{E}_x$ and (d) $\mathcal{E}_y$ in xz cross section for a ribbon with w = 50 nm and p = 100 nm at 970 nm resonance. (e) Total electric field intensity in xz cross section (log scale) at 970 nm resonance.

attributed to the LSPP resonance in the higher conducting $\hat{x}$ direction. When the polarization is set to ϕ_p = 45°, the peak intensity at 1.75 μm drops and a second peak emerges at 2.88 μm which is likewise associated with LSPP resonance in y direction. Finally, when the polarization is (ϕ_p = 90°), the first peak disappears and the LSPP resonance in $\hat{y}$ direction at 2.88 μm becomes dominant. Such a strong dichroism is in line with expectations since borophene is patterned along its principal axes and the diagonal terms of conductivity (i.e. σ_{xy} and σ_{yx}) are zero in the absence of magnetic field. As a result, as long as the polarization of the incident light is aligned with the

in-plane crystal axes, only one of the x or y LSPP resonances can be excited which will be the one parallel to the polarization of the impinging field. These resonances can be tuned significantly by varying geometric or carrier density parameters w, p and n, increase of which would respectively result in blue-shift, red-shift and blue-shift of the resonances corresponding to x and y resonances. These trends are implied in Figures 3.3a-b and Figures 3.4a-b. On the other hand, the two resonances can be excited simultaneously, although with lower intensity, when the polarization of light is not parallel to the optical axes.

Figure 3.5c shows the intensity of the x component of the electric field at its corresponding LSPP resonance λ = 1.75 μm when the polarization is set to 45°. This panel suggests that there is almost two orders of magnitude field enhancement and the signature dipolar response along x direction is also recognizable. The y counterpart is also shown in Figure 3.5a where all the values are the same except for the sampled wavelength which is the LSPP resonance in y direction, λ = 2.88 μm. The absorption peak in Figure 3.5b hits 0.4 in borophene. The polarization-sensitive nature of borophene provides ample opportunities to apply this feature to birefringence applications in visible range. We also note that the intensities of absorption values in both directions can be boosted to near unity values which would render the absorption for ϕ_p = 45° to more than 0.5, by adding a metallic back reflector to form a vertical plasmonic metal-insulator-borophene cavity [70] (Appendix A.2).

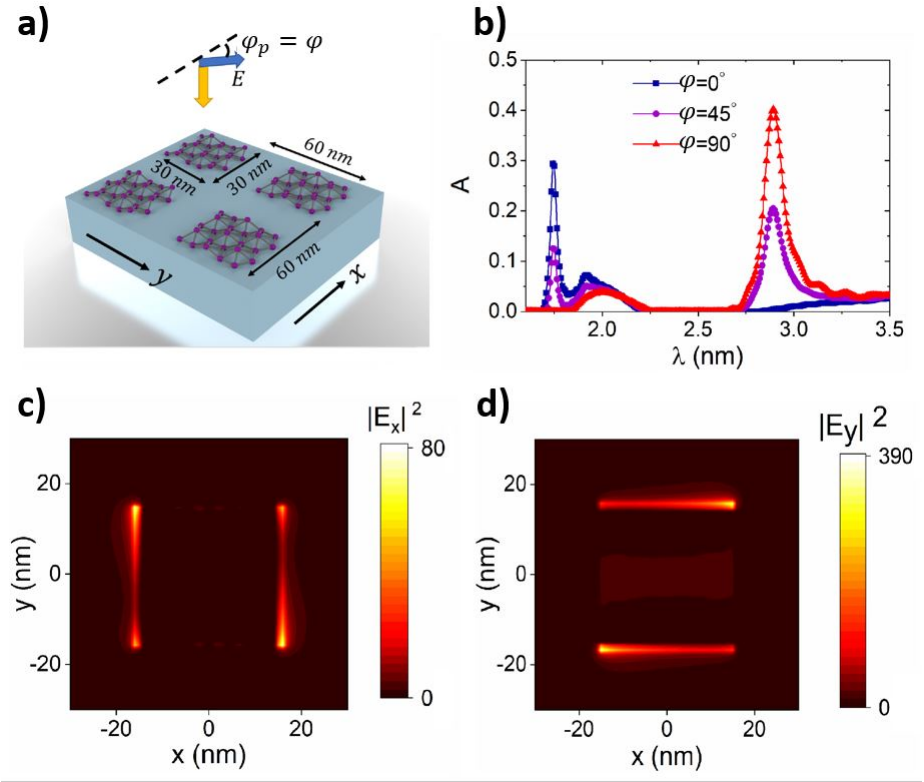

Figure 3.5. Demonstration of dichroism caused by anisotropic LSPPs. (a) Schematic of patterned borophene in square patches of 30 nm side on SiO_2 substrate with a periodicity value of 60 nm, (b) absorption versus wavelength for three different polarization values ϕ_p = 0, 45 and 90°. Field intensity values for ϕ_p = 45° on the surface of borophene square patches (xy cross section) for (c) $\mathcal{E}_x$ at the first ($\hat{x}$) resonance λ = 1.75 μm and (d) $\mathcal{E}_y$ at $\hat{y}$ resonance λ = 2.88 μm.

3.2.4. Anisotropic plasmon-enhanced birefringence

The large dichroism that stems from anisotropic LSPP resonances has significant implications in photonics. Metal-based metasurfaces used to dominate metamaterials birefringence effects that lead to phenomena such as anomalous reflection and refraction [80]. It was the advent of graphene that changed this perspective; many 2D van der Waals materials even in monolayer thickness have strong anisotropy in their plasmonic response

that allows hyperbolic and elliptic plasmons to exist[89]. Even though isotropic graphene can demonstrate giant birefringence if patterned, natural anisotropic 2D materials provide even stronger birefringence when patterned in nanoribbon structure. Here, we will briefly analyze a simple configuration using borophene that can rotate the polarization of light in reflection and transmission mode from which manifests the potential of borophene in photonics applications. The conductance tensor of a continuous anisotropic 2D material like borophene can be described by

$$\bar{\bar{\sigma}} = \begin{bmatrix} \sigma_{xx} & \sigma_{xy} \\ \sigma_{yx} & \sigma_{yy}, \end{bmatrix}, \tag{3.1}$$

where the diagonal conductivity values are calculated using Drude model 2.46. Since all of the patterning examples on borophene are carried out along the principal axes, the off-diagonal elements of conductivity vanish. When borophene monolayer is patterned in nanoribbon configuration, the coupling between the ribbons modifies the diagonal terms. As a result, Lorentz-like terms appear in the diagonal terms. The poles of Lorentz terms will force the conductivity to approach zero, a phenomenon known as sigma near zero [95]. This topological transition point divides the effective conductivity to two regions with different and significant properties [96]. In order to analyze this phenomenon, effective medium theory (EMT) can be used which assumes a capacitive coupling between the two principal axes [97, 98]. This following equation is similar to Equation 2.49 except that here it is applied to the conductivity rather than dielectric function. If borophene is patterned in the $\hat{x}$ direction, the impedance of the nanoribbon region (Z_n) and gap region (Z_g) can be calculated as,

$$Z_n = \sigma^{-1}, \qquad Z_g = \frac{i}{\omega C_c}, \tag{3.2}$$

where Z_n is simply the inverse of the borophene conductivity tensor (since it represents the area covered by borophene). C_c is the near-field capacitive coupling term given by

$$C_c = \frac{2\epsilon_0 p}{0.75\pi} \ln(\csc(\frac{\pi(1-f)}{2})), \tag{3.3}$$

where p is the periodicity of the strips and $f = w/p$ is the filling ratio of borophene within each cell and a phase shift of 0.75π is assumed as discussed in the modeling section. Using Equations 3.1–3.3, the effective conductivity tensor can be derived as $\sigma_{eff} = f(Z_n + fZ_g)^{-1}$. In order to tailor this discussion to borophene, a simple configuration is proposed. A borophene layer is patterned in $\hat{x}$ direction with w = 34 nm and p = 68 nm, similar to the inset of Figure 3.1a except on a SiO_2 substrate. Figures 3.6a and b represent the two diagonal conductivity values for continuous and patterned borophene with the mentioned parameters, between 400 nm and 2000 nm wavelength range. The critical point in Figure 3.6b at 1500 nm marks the distinction between two different regions of operation in the patterned borophene. The real parts of the conductivities in both directions are positive for all of the wavelength values. Our results show two orders of magnitude larger conductivity for $\hat{x}$ direction compared to $\hat{y}$ in the vicinity of resonance, 1550 nm. Below λ = 1500 nm, the imaginary parts of the two conductivity values have similar signs ($\Im m(\sigma_x).\Im m(\sigma_y) > 0$) which represents elliptic region. In the elliptic region, anisotropy exists, and plasmons can evolve in

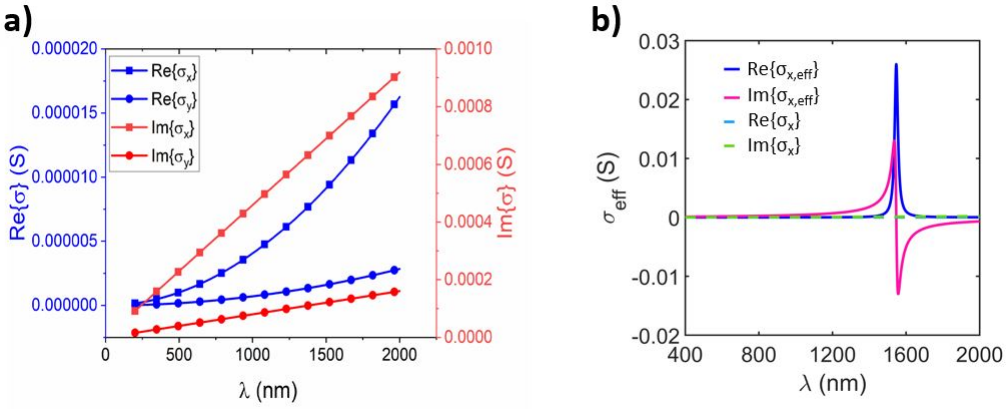

Figure 3.6. Conductivity versus wavelength for (a) continuous borophene, (b) patterned borophene in form of nanoribbons in $\hat{x}$ direction with w = 34 nm and p = 68 nm.

elliptic manner in both directions and wavefronts would form elliptic propagation pattern. Contrarily, when $\lambda > 1500$ nm the imaginary parts of the conductivities have opposite signs ($\Im m(\sigma_x).\Im m(\sigma_y) < 0$) which marks the hyperbolic region [99].

One of the implications of hyperbolic region is that it can support hyperbolic plasmons in the case of a patterned structure which can give rise to polarization ellipse rotation. In order to understand this phenomenon better, simulations have been carried out for the structure whose effective conductivity is shown in Figure 3.6b. Figures 3.7a and 3.6b summarize the polarization ellipse major angle and magnitude ratio of electric field in two different in-plane directions ($\hat{x}$ and $\hat{y}$). These results are recorded for normal incidence with polarization (ϕ_p) set to 45° in the far-field limit. The monitor is also normal to the borophene plane. It is evident from these two panels that at 1550 nm (C-band), the polarization of the reflected and transmitted light is the strongest for the patterned film, reaching 25°. We recognize that the continuous borophene film also demonstrates polarization ellipse rotation in reflectance as much as 15°, however,

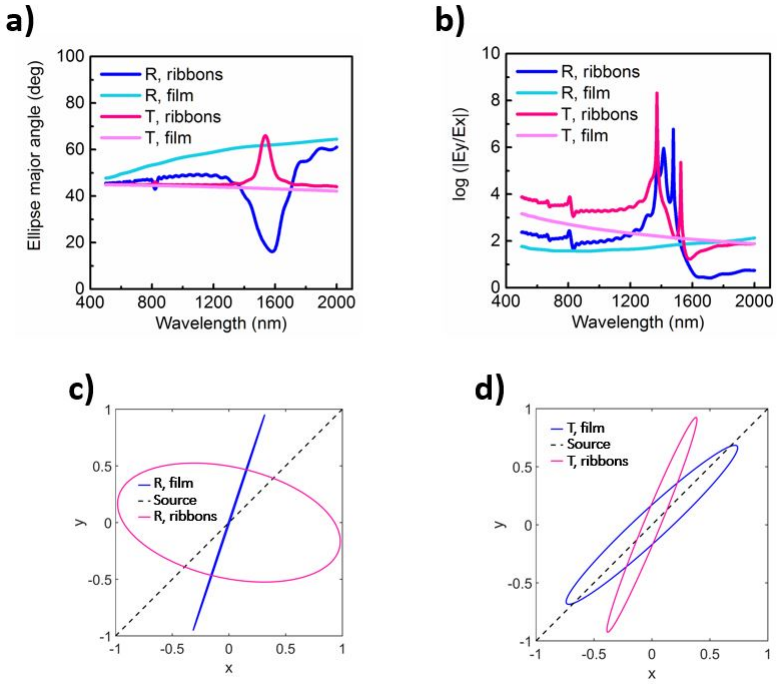

Figure 3.7. Simulated far-field (a) polarization ellipse major angle, and (b) electric field ratio between $\mathcal{E}_y$ and $\mathcal{E}_x$ versus wavelength, when the applied field is linearly polarized with ϕ_p = 45°, in transmission and reflection mode for continuous and patterned (ribbon) borophene. Polarization ellipse of continuous and patterned borophene at 1550 nm in (c) reflection and (d) transmission mode.

the reflected power is less than 8% which demonstrates poor efficiency. In contrast, in the patterned case, the reflection is enhanced above 20% and the polarization rotation is also increased as seen in illustrated in Figure 3.6c which demonstrates the reflected polarization ellipse at 1550 nm, for continuous and patterned borophene layers on SiO_2 substrate. The effect of patterning on polarization rotation is more pronounced in the transmittance mode; the continuous borophene film results in negligible polarization rotation unlike the patterned configuration, where the rotation reaches 17°. Moreover, the hyperbolic region can be passively and actively tuned respectively with geometry

parameters such as w and p and electrostatic gating to modify carrier density. Therefore, this simple structure can significantly rotate the polarization state of the incoming linearly polarized light in one atomic layer thickness which reveals the strength of borophene in dynamically tunable manipulation of phase, amplitude and polarization of impinging light as a whole which is an essential issue in photonics. The metallic 2D borophene in this study can be tailored to the existing wealth of electro-optical tuning mechanisms and quantum well configurations established in the work of Sherrott *et al.* with BP and can lead to next generation of 2D heterostructure photonics [95].

3.3. Naturally birefringent vdW material: α-MoO_3 birefringence for VIS photonics

3.3.1. Motivation

Birefringent crystals and wave-plate and retarder devices such as $CaCo_3$ and quartz are available and reliable in VIS [10]. However, these crystals are grown in bulk form and are not suitable for heterostructure photonics. The complexity of existing nanofabrication techniques and the optical losses of metamaterials limit their application [100]. Plasmon polaritons are shown to be lossy and are not the best candidates for polarization manipulation, as discussed previously in Section 1.3 (Limitations of polaritons). vdW materials, on the other hand, can be grown and transferred onto any desired substrate. The growing library of vdW materials now comprise of both high lattice symmetry isotropic materials and more importantly, anisotropic materials with low lattice symmetry which was a turning point with the introduction of orthorhombic black phosphorus (BP) [70]. Ever since, a myriad of anisotropic vdW crystals with in-plane optical anisotropy have been identified and studied, such as hexagonal boron nitride (hBN), orthorhombic SnSe [51],

monoclinic GaTe [101] and triclinic ReS_2 [52]. The optical response of BP can be actively tuned by electrostatic gating which makes it an outstanding material for polarization-dependent sensor applications [102]. However, BP chemically degrades in ambient, and a capping layer is required to keep the rich electro-optical characteristics of BP intact [103]. α-MoO_3, on the the other hand, is stable and has been adopted for devices. The disadvantage of α-MoO_3 is that it is a weak semiconductor and cannot be tuned with electrostatic gating. Its advantage, on the other hand, is its lossless nature in VIS similar to $CaCo_3$, thanks to its high bandgap ($\sim$ 3.4 eV) [104]. While α-MoO_3 is extensively studied for its outstanding near-field properties in IR and for the first time for its far-field characteristics, it has been studied scarcely for its optical in-plane anisotropy in VIS to the best of our knowledge. Here, we attempt to study optical anisotropy of α-MoO_3 in VIS more rigorously in a FP structure. Figure 3.8a schematically illustrates the sample structure that has been investigated in this study. α-MoO_3 flakes are directly grown on sapphire and are imaged and characterized with linear polarizer and analyzer on the optical beam path. The angles for polarizer and analyzer are ϕ_p and ϕ_a respectively, defined with respect to $\hat{x}$ axis. The $\hat{x}$, $\hat{y}$, and $\hat{z}$ axes respectively represent [100], [001] and [010] crystal directions of α-MoO_3, as established by previous works [105]. The optical images of two flakes in transmission mode are put forth in Figure 3.8b for various ϕ_a values where ϕ_p = -45°. The optical anisotropy is evident due to the color change of flakes under analyzer rotation.

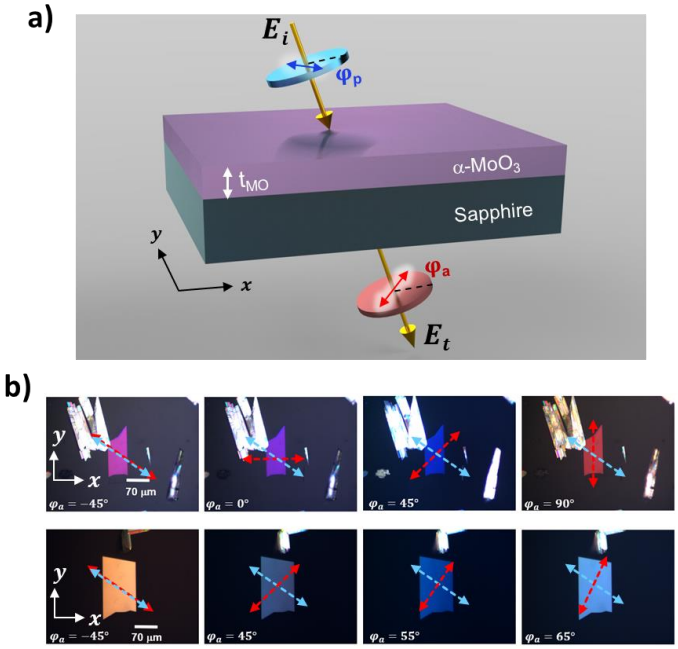

Figure 3.8. (a) Schematic representation of samples and depolarization measurements. (b) Images taken in transmission mode from two α-MoO_3 flakes for various analyzer angles (ϕ_a) when the polarizer angle is set to ϕ_p=-45°. The dashed blue and red arrows respectively represent ϕ_p (polarizer angle) and ϕ_a (analyzer angle). ϕ_a values are also written in the insets of (b). Note that the reflectance intensity is low and the input intensity is not kept constant so that the flakes can be visualized.

3.3.2. Experiments

Fabrication. The multilayer FP structure was fabricated using physical vapor deposition (PVD). Au and Ag for all the samples were deposited on quartz substrates using AJA eBeam Evaporator system and the base and deposition pressures were respectively 9×10^{-7} and 3×10^{-6} Torr. The deposition rate was 0.5 nm s^{-1}. α-MoO_3 flakes were grown using low-pressure physical vapor deposition. For this process, 50 mg of MoO_3 (Sigma-Aldrich) powder was spread evenly within an alumina boat. This boat was placed within a 1-inch diameter quartz tube and at the center of a small

Lindberg tube furnace. A 41 in.^{2} rectangular piece of a quartz wafer was placed face-up downstream in a colder zone of the furnace. This piece was suspended on the top of the alumina boat and was located roughly 4 cm from the center region. The pressure was maintained at 2.8 Torr with a carrier gas of O_2 at a flow rate of 25 sccm. The center of the furnace was then heated to 675 °C over a period of 25 min and then to 700 °C over a period of 5 min. Upon reaching 700 °C, the furnace was immediately opened, thereby quenching the deposition.

Characterization. For the measurement of the samples, an inverted microscope system was used. The system was established up with a Nikon TI inverted microscope equipped with an Andor Actor spectrometer with an electron multiplication charge-coupled device (EM-CCD) camera. A broadband halogen lamp with a linear polarizer and/or analyzer was used to generate polarized broadband illumination. The reflected and transmitted light was collected by a 50× Nikon microscope objective lens in configuration represented in Figure 2.2b.

3.3.3. α-MoO_3 VIS optical model

One of the critical information needed for fitting the optical model of a film is its thickness. Figure 3.9 demonstrates the Atomic Force Microscopy (AFM) data taken from the flakes to determine their thicknesses, for flakes F1 and F3 that will be studied here.

In order to investigate polarization characteristics of α-MoO_3, we need to identify the refractive index for different crystal directions. Despite the availability of the optical model of α-MoO_3 in previous works [106], they have not been reported in thin flakes

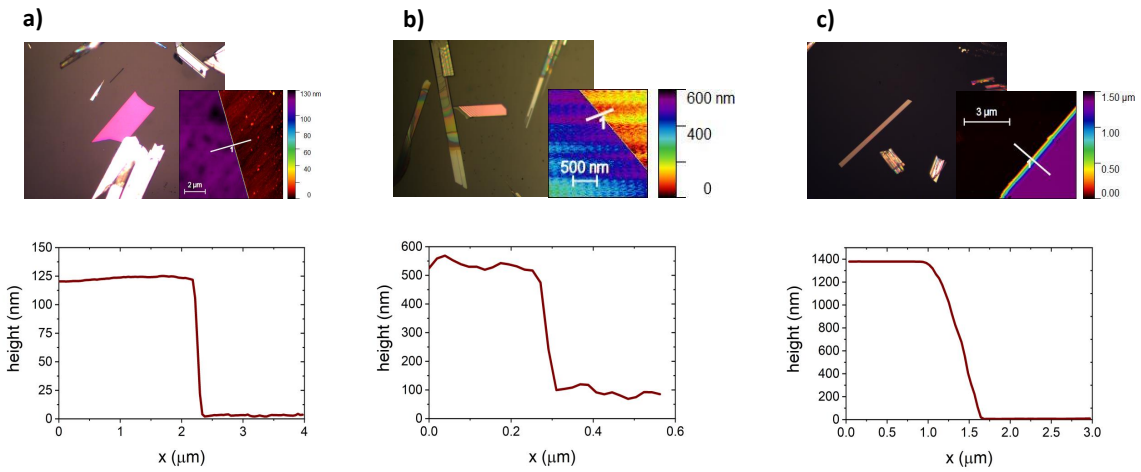

Figure 3.9. (a) Optical image, AFM and line profile representing thicknesses of flakes (a) F1, (b) F2 and (c) F3.

[107]. Thus, the optical model is fine-tuned in this work to match several reflectance/transmittance measurements conducted on several flakes. To obtain a reliable optical model, several transmission and reflection measurements are conducted in three different polarizer-analyzer configurations: a) without polarizers and analyzers, b) with polarizers and no analyzers, and c) with both polarizers and analyzers. Some measurements for cases a and b are provided in Figures 3.10a-d for two different flakes, F1, F2 and F3 with MoO_3 thickness (t_{MO}) values of 124 nm and 1400 nm (Figure 3.9. The measurements are fitted with 2×2 TMM simulation of multilayers (as outlined in Chapter 2.1) to obtain an optical model for three distinct refractive indices of α-MoO_3,

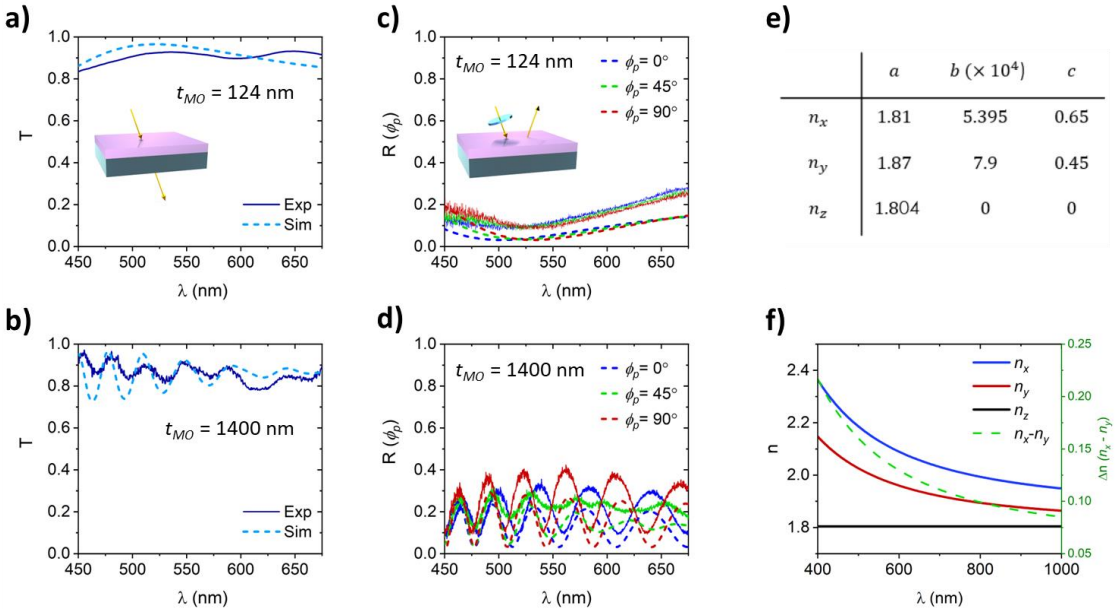

	a	b ($\times 10^4$)	c
n_x	1.81	5.395	0.65
n_y	1.87	7.9	0.45
n_z	1.804	0	0

Figure 3.10. Measured (solid lines) and simulated (dashed lines) total transmittance (T) of flakes (a) F1 and (c) F3. Measured (solid lines) and simulated (dashed lines) polarizer-dependent reflectance ($R(\phi_p)$) of flakes F1 (b) and F3 (d). (e) Cauchy parameter values used to fit the refractive index tensor of α-MoO_3 in visible range. (f) refractive index of α-MoO_3 in x, y and z directions and its in-plane spectral birefringence. The insets of (a) and (c) illustrate the measurement and simulation setup.

$$\bar{\bar{n}} = \begin{bmatrix} n_x & 0 & 0 \\ 0 & n_y & 0 \\ 0 & 0 & n_z \end{bmatrix}. \tag{3.4}$$

The bandgap of α-MoO_3 is in ultraviolet wavelengths and the absorption of α-MoO_3 is negligible in VIS as evident in Figures 3.10a-d. Hence, Cauchy's model (Equation 2.45) can be implemented assuming $Im(\bar{\bar{n}}) = 0 \cdot I_3$ where I_3 is a 3×3 is identity matrix.

The obtained Cauchy parameters are listed in Figure 3.10e and they are also sketched in Figure 3.10f. The x direction is obtained by measuring reflectance of the flakes and observing the optical phonons at [100] direction with Fourier transform infrared spectroscopy (FTIR) [54]. The peaks observed in Figure 3.10a and b can be described by the interference effect. Here, an approximate discussion is provided to have an estimation of the number of the peaks in the measured data and to provide insight into this phenomenon. Due to the Fabry-Perot equation, $\beta + \phi_t = 2m\pi, m = 1, 2, \ldots$ where β is the net spatial phase accumulated by forward or backward traveling incident light inside α-MoO_3, ϕ_t is the total phase accumulated upon transmission at either interface (air/MoO_3 and MoO_3/sapphire) and m is an integer. β can be calculated as $\beta = 2\pi n t_{MO}/\lambda$ where n is the refractive index between 1.8 and 2.3 in VIS (See Figure 3.10f). An approximate value of n = 2 is assumed. The value of $\beta \cdot \lambda$ for F1 (t_{MO} = 124 nm) and F3 (t_{MO} = 1400 nm) is in the order of 1600 and 14000, respectively. The number of the possible FP resonances in VIS (n_{FP}) can be estimated by $n_{FP} = (\beta\lambda)/550\pi$ where 550 nm is chosen as an average resonance wavelength value from the VIS range. $n_{FP} \approx 0.94$ and 8.11 respectively for F1 and F3 which are close to the number of peaks observed in Figure 3.10a and b. in VIS which is clearly 1 for F1 ($1600/m\pi \approx 509$ nm, m = 1). Contrarily, several peaks can be found for a wider range of m values for F3. In the presence of a polarizer (Figure 3.10b and d) interference patterns are present that differ for x- and y-polarized incident lights which is due to the birefringence of α-MoO_3. This difference is more dramatic for F3 due to its high thickness. Thus, the observed oscillations from the measured data follow approximate expectations.

3.3.4. Wave plates in VIS with α-MoO_3

To get a further insight into depolarization of incident light through transmission, having calculated the transmitted fields with TMM, the spectral ellipticity (r) versus flake thickness is simulated. The ellipticity is $r = a/b$ where a and b are respectively the smaller and the bigger diameter of the polarization ellipse in transmission. The result is illustrated in Figure 3.11a where the shades of blue and purple are the extreme cases of $r = 0$ and 1 respectively. In order to match simulations to measurements, three flakes F1, F2 and F3 with different thicknesses of 124 nm, 540 nm and 1400 nm, respectively are measured. The characterization is conducted using one linear polarizer and one linear analyzer (Figure 3.8a and Section 2.2) and the data points are marked on Figure 3.11a for green (λ = 532 nm) and red laser (λ = 633 nm) wavelengths for each flake. Figure 3.11b-d represent polar plot at green and red laser wavelengths for flakes F1, F2 and F3, respectively. The characterization for these plots is carried out with ϕ_p=45° while ϕ_a is varied. The left half of each polar plot with line curve is the simulated result and the right half with circle markers is the measured result. The green and red curves infer the chosen wavelengths of λ = 532 nm and λ = 633 nm, respectively. The dashed blue line in each polar plot represents the incident linearly polarized light with no sample on the beam path. Also, due to the symmetry of the polar plots, only one half of polar plots are demonstrated for measurements and simulations to juxtapose the estimated and measured polarization-sensitive characteristics for comparison. The simulation and measured results are in good agreement as seen in Figure 3.11b-d. Another critical factor in determining the polarization state is the phase difference (δ). δ is the phase difference between y and x components of electric field ($\mathcal{E}_y$ and $\mathcal{E}_x$), $\delta = \angle\mathcal{E}_y - \angle\mathcal{E}_x$

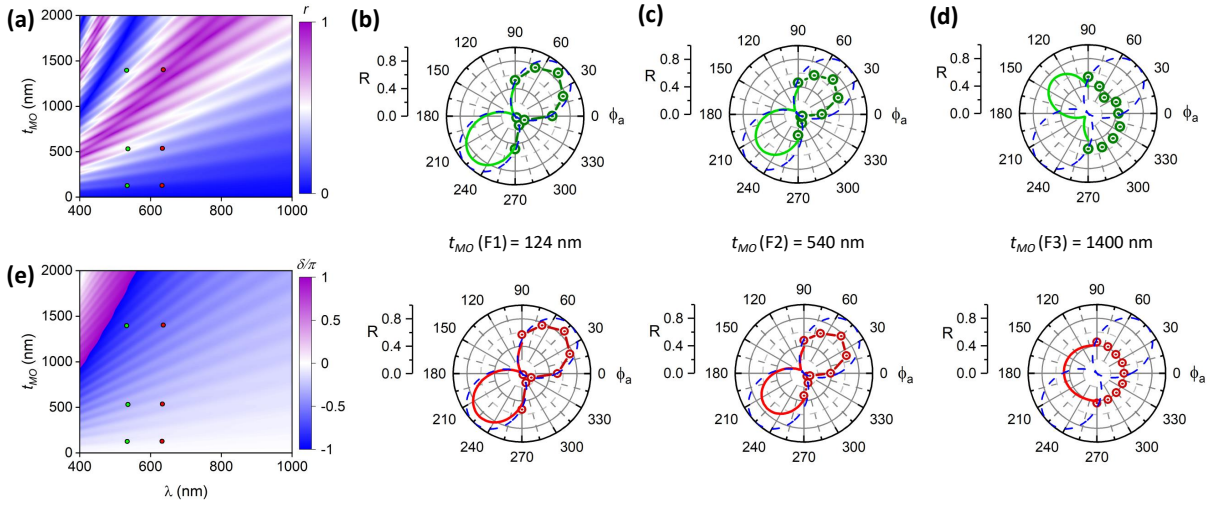

Figure 3.11. (a) Simulated spectral ellipticity (r) versus α-MoO_3 thickness (t_{MO}). Simulated (solid line) and measured (data points) polar plots of reflectance (R) as a function of analyzer angle (ϕ_a) when polarizer angle is kept constant at ϕ_p = 45°, at 532 nm (green) and 633 nm (red) wavelengths for flakes (b) F1 (t_{MO} =124 nm), (c) F2 (t_{MO} =540 nm) and (d) F3 (t_{MO} =1400 nm). The blue dashed line in (b-d) illustrate the source characterization at various ϕ_a values when ϕ_p = 45°. (e) Simulated spectral phase difference $\delta = \delta_y - \delta_x$ as a function of t_{MO} (normalized to π). The dots on (a) and (e) represent the data points from (b-d).

which is embedded in the polarization ellipse equation (Equation 2.20). The simulated spectral phase difference δ/π as a function of t_{MO} is illustrated in Figure 3.11e with experimental data of Figure 3.11b-d marked on it. Figure 3.11b-d imply that various polarization states are obtainable by α-MoO_3 and attest to its strong birefringence. F1 is only 124 nm-thick and the incident polarization is almost sustained. This is expected since the optical path difference is small for such a thin material. At λ = 532 nm (λ = 633 nm), the in-plane birefringence is Δn_{green} = 0.15 (Δn_{red} = 0.12) and the optical

path difference (OPD) for F1 is $OPD = t_{MO}\Delta n_{green}$= 18.6 nm (14.88 nm) leading to a phase difference (i.e. retardation) of $\Delta\beta = (2\pi/\lambda) \cdot OPD = 0.07\pi$ (0.05π) which is negligible and the incident polarization is almost retained. The depolarization is higher for F2 (t_{MO} = 540 nm) where for green (red) wavelengths, OPD = 81 nm (64.8 nm) and $\Delta\beta = 0.3\pi$ (0.2π) and the resulting polarizations will be left-handed elliptical, implied from negative phase differences in Figure 3.11e. The depolarization is the most significant for F3 (t_{MO} = 1400 nm) where at λ = 532 nm (λ = 633 nm), OPD = 210 nm (168 nm) and $\Delta\beta = 0.69\pi$ (0.53π). The $\Delta\beta > 0.5\pi$ at λ = 532 nm and r = 0.3 yields a 90° rotated linear-looking left-handed ellipse with respect to the incident polarization, which demonstrates a half-wave plate action at this wavelength, with a $\Delta\beta$ value close to π. More interestingly, at λ = 633 nm, $\Delta\beta$ is very close to 0.5π and r = 0.89 which is close to 1, implying a left-handed circular polarization for the transmitted light as evident in Figure 3.11d, demonstrating a quarter waveplate action at λ = 633 nm. Birefringence values of 0.15 and 0.12 observed at 532 nm and 633 nm for α-MoO_3 is comparable to the existing commercial birefringent materials such as $CaCO_3$ [10] and much higher than quartz [108]. Figure 3.12 compares the birefringence of α-MoO_3 to some birefringent vdW and bulk crystals.

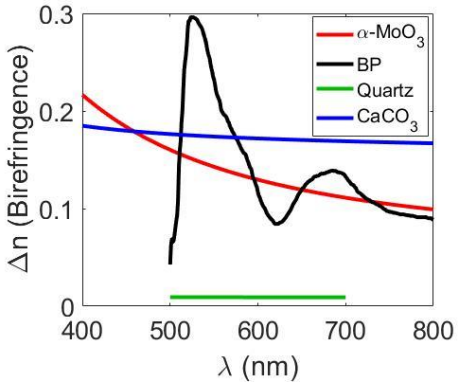

Figure 3.12. Birefringence of α-MoO_3 compared to other materials. Data for other materials taken from [10, 108, 109].

Stokes parameters matrix is a powerful tool to obtain phase difference in measurements. The Stokes (S) parameters with values between 0 and 1 are defined as

$$S = \begin{bmatrix} S0 \\ S1 \\ S2 \\ S3 \end{bmatrix} = \begin{bmatrix} E_{0x}^2 + E_{0y}^2 \\ E_{0x}^2 - E_{0y}^2 \\ 2E_{0x}^2 E_{0y}^2 \cos\delta \\ 2E_{0x}^2 E_{0y}^2 \sin\delta \end{bmatrix}. \tag{3.5}$$

$S0$ represents optical intensity (transmittance in this case). S1 measures the strength of 0° linear polarization ($S1$ = 1) as opposed to 90° linear polarization ($S1$ = -1). $S2$ describes the strength of 45° linear polarization (S2 = 1) as opposed to -45° linear polarization (S2 = -1). Finally, $S3$ represents the strength of right hand circularly polarized

light ($S3 = 1$) as opposed to left hand circularly polarized light ($S3 = -1$) [110]. Having validated the linear polarization characterization on Figure 3.11, the simulated Poincare sphere points for F1, F2 and F3 are illustrated in Figure 3.13 at green (λ = 532 nm) and red (λ = 633 nm) wavelengths. S0 is not provided here since it carries intensity information that has already been discussed in Figure 3.10. For flake F3 at λ = 633 nm, the simulated S parameters ($S1, S2, S3$) = (0.011, -0.057, -0.998) representing almost an ideal LCP light (0, 0, -1) with a transmittance value of T = 88.15%. At λ = 532 nm, F3 the transmitted light (T = 82.52%) has ($S1, S2, S3$) = (0.024, -0.86, -0.509) which is closer to a linearly polarized light (0, -1, 0). The half-wave plate action is more ideal near λ = 480 nm (T = 95.1%) where ($S1, S2, S3$) = (-0.006, -0.999, -0.053) as seen in Figure 3.13b. The simulations also show that the flake F1 demonstrates a -45° linearly polarized transmitted light (T = 90.6%) at the same wavelength with parameters ($S1, S2, S3$) = (0.007, 0.993, -0.11) with r = 0.04. The evolution of the polarization ellipse versus wavelength is depicted for flakes F1, F2 and F3 in Figure 3.13b. As can be seen from Figure 3.13d, different polarization states are achievable.

3.3.5. Twisted bilayer α-MoO_3 heterostructures for polarization tuning

One of the promises of vdW materials is the prospect of forming heterostructures for electronic and photonic applications. Here, we demonstrate that the polarization state of the transmitted light can be tuned by adding an extra parameter, i.e. the rotation angle (α) between the overlapping α-MoO_3 flakes. An example of overlapping flakes is schematically illustrated in Figure 3.14a and photographed on sample (Figure 3.14b). The areas marked on Figure 3.14b as I, II and III refer respectively to bottom flake

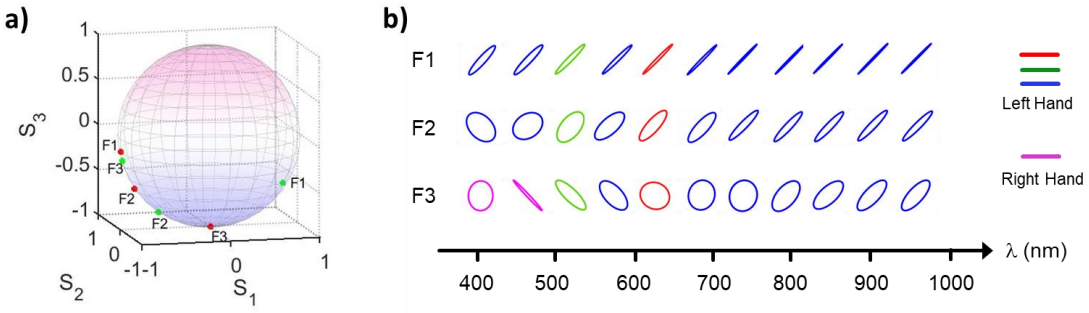

Figure 3.13. (a) Poincare sphere showcasing the data points for F1, F2 and F3 at green and red wavelengths. (b) Polarization ellipse at several wavelengths for flakes F1, F2 and F3. The blue polarization ellipses are left-handed, and the rest are right-handed. The green and red polarization ellipses respectively represent polarization ellipses (left-handed) at 532 nm (green) and 633 nm (red) wavelengths.

($t_{MO,bottom}$ = 570 nm), top flake ($t_{MO,top}$ = 350 nm), and the overlapping region with α = 68° between the flakes (Figure 3.15). In order to characterize the depolarization directly, the ratio of the transmitted cross-polarized light (ϕ_p = -45°) to co-polarized (ϕ_p = 45°) light is measured for regions I, II and III (Figure 3.14c). The dashed curves are the simulation results, and the black dashed curve is for α = 0° ($t_{MO} = t_{MO,bottom} + t_{MO,top}$ = 920 nm). It should be noted that the top flake is suspended and there is a gap of ≈ 570 nm between the top flake and the substrate (see Figure 3.15). The simulations are in reasonable agreement with experimental results.

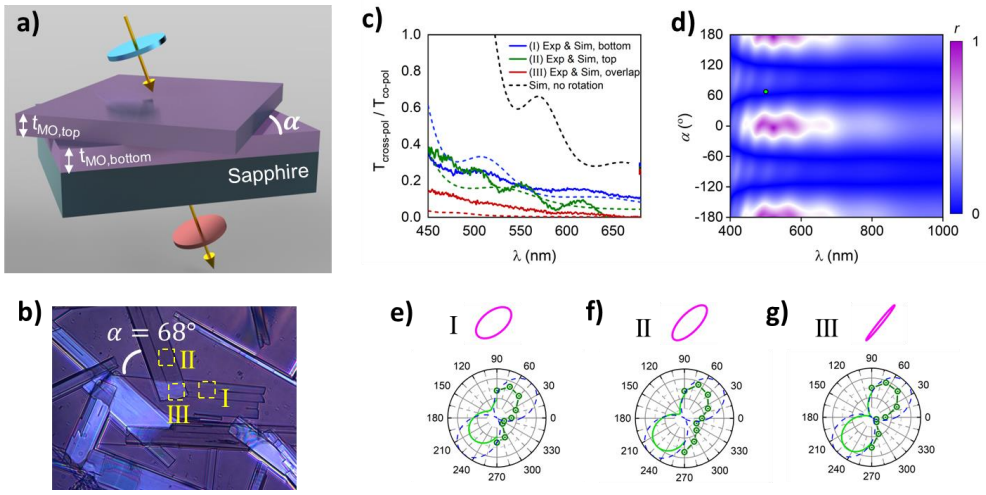

Figure 3.14. (a) Schematic representation of the overlapping flakes along with the experimental setup. (b) Photo of the overlapping flakes under study with marked regions I, II and III representing respectively the bottom flake, top flake, and the overlapping region. (c) The simulated and measured ratio of the cross-polarized to co-polarized transmittance for regions marked in (b) for flake rotation angle α = 68°. The dashed line represents the case where there is no rotation between the flake axes (α = 0). (d) Simulated spectral ellipticity (r) versus α. The green dotted line represents 500 nm data mark. (e-f) The simulated and measured polar plots of reflectance as a function of analyzer angle (ϕ_a) when polarizer angle is kept constant at ϕ_p=45° at regions I, II and III shown in (b) at 500 nm wavelength. The blue dashed line in (e-f) illustrate the source characterization at various ϕ_a values when ϕ_p=45°. The insets in (e-f) are the respective polarization ellipses.

Figure 3.14c shows that there is some depolarization for bottom and top flake which diminishes in the overlap region III. This is due to the fact that the highest contrast of in-plane birefringence happens when the incoming polarization is set to the mid-range polarization values (ϕ_p = ±45°), and the large rotation angle close to ϕ_p = 45°

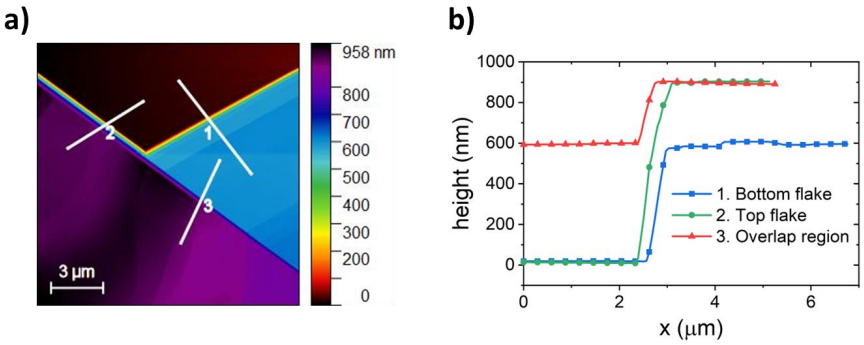

Figure 3.15. AFM and line profile representing thicknesses of bottom, top and overlapping α-MoO_3 flakes.

annihilates the optical path length difference. The spectral ellipticity is simulated as a function of the rotation angle α for two overlapping flakes with $t_{MO,bottom}$ = 570 nm and $t_{MO,top}$ = 350 nm and illustrated in Figure 3.14d. The green mark on Figure 3.14d demonstrates the data gathered from the flake which shows linear polarization. The polarization ellipses along with measured and simulated polar transmittance plots are illustrated in Figure 3.14e. The purple regions in Figure 3.14d locate where the quarter wave plate action happens. It can be inferred from this figure that for small rotation angles α, the quarter wave plate wavelength can be tuned; for example, changing α from -10° to +10°, the quarter wave plate wavelength can be tuned from 523 nm to 564 nm. Such an extra parameter (i.e. α) to engineer polarization can bring new possibilities for optoelectronic devices implemented with vdW materials. α can be

benefitted in multilayer vdW heterostructures to obtain layers of α-MoO_3 with different effective n_x and n_y values using different orientation of the same material.

3.3.6. Polarization-sensitive filters using α-MoO_3

Polarization-sensitive reflection filter. A polarization-sensitive reflection filter is designed with details illustrated schematically in Figure 3.16a. The inset of Figure 3.16a shows the optical image of a cavity containing α-MoO_3 ($h \approx 80$ nm) fully encapsulated on top and bottom by Au films. We intentionally chose optically thick (b = 150 nm) Au as the bottom metal layer to eliminate the transmission. The top Au film is set to be t = 30 nm to balance the light penetration into the planar nanocavity with the material losses. To experimentally verify the polarization-dependent function of the device, we performed polarization-dependent reflectance measurements on a designed α-MoO_3 cavity, as shown in Figure 3.16b. The reflectance spectrum with normally incident light polarized along $\hat{x}$ (defined as $\phi_p = 0°$ polarization) of α-MoO_3 crystal has a resonance peak wavelength at 684 nm due to the resonance of the FP cavity related to the thickness of the α-MoO_3. Since the crystal structure of α-MoO_3 is sensitive to the polarization of the incident light, the peak wavelength of reflectance spectrum shifts to 662 nm when the light polarized along $\hat{y}$ (defined as $\phi_p = 90°$ polarization). One can see the continuous shifting of the peak wavelength of reflectance spectra with the polarization angle changing from the $\hat{x}$ to $\hat{y}$. The TMM simulation of the device is shown in Figure 3.16c which agrees with the experimental observations. By tuning the thickness of α-MoO_3, the polarization device could work across the whole visible range.

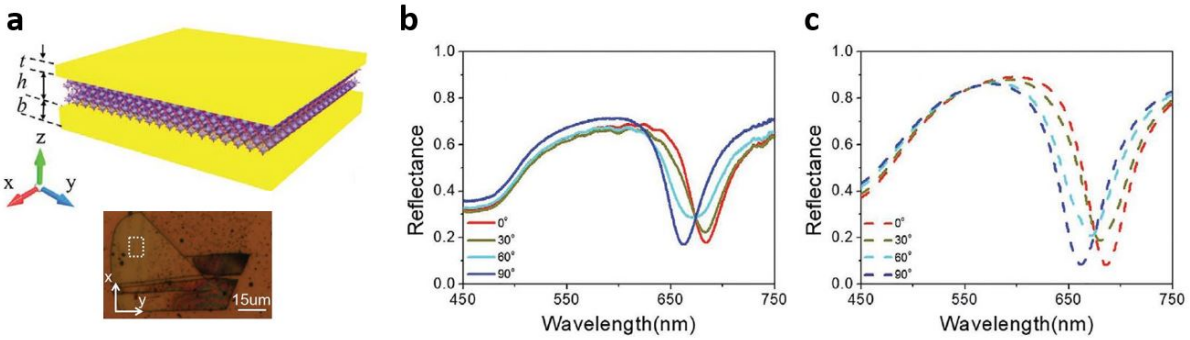

Figure 3.16. (a) Schematic of planar triple-layer metal/α-MoO_3/metal device and optical image of α-MoO_3 polarization reflector with thickness t = 30 nm, h = 80 nm, and b = 150 nm. The white dashed square represent the measured area. (b) Measured and c) simulated reflectance spectra for α-MoO_3 polarization reflector where the incident light is linearly polarized in directions ranging from the $\hat{x}$ to $\hat{y}$ crystal axes (ϕ_p = 0° to 90°) in 30° steps.

Polarization-sensitive transmission filter. When the thickness of the bottom metallic film is reduced, the incident light can propagate through the α-MoO_3 cavities, which allows the α-MoO_3 cavities to act as color filters. We choose Ag as the metallic film on top and bottom for lower optical losses and higher quality factors. Thinner Ag layers lead to higher transmission. However, the experimental procedure, in this case, sets a limit on the minimal film thickness of Ag. Namely, Ag layers thinner than 20 nm do not form continuous layers and tended to delaminate during the α-MoO_3 transfer process. As such, the thicknesses of the top and bottom Ag are set to 20 and 30 nm, respectively. Figure 3.17a, b shows the optical image of α-MoO_3 polarization color filter under transmittance mode for ϕ_p = 0° and 90°, respectively. Since the α-MoO_3 surface is not uniform, multiple colors appear on the optical image. Thus, we choose a small area for the following measurement marked as white dash line square in Figure 3.17a, b. In the measurement area, the thickness of the α-MoO_3 is approximately 260 nm.

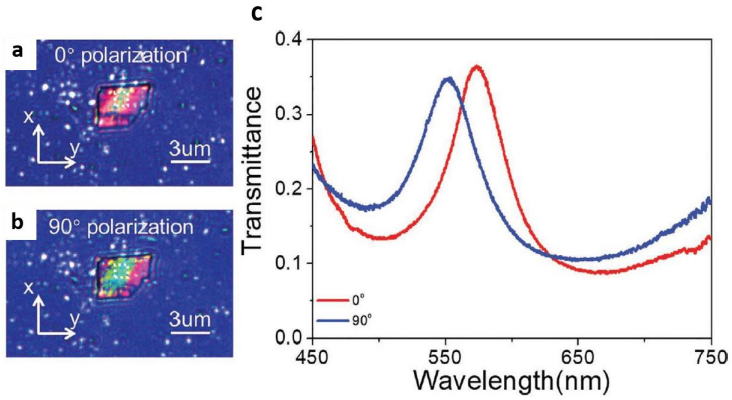

Figure 3.17. Optical image of α-MoO_3 polarization color filter with thickness values t = 20 nm, h = 290 nm, and b = 20 nm for (a) ϕ_p = 0° and (b) ϕ_p = 90°. White dashed squares represent the measured area. The color turns from chartreuse to green when the linear polarization angle (ϕ_p changes from 0° to 90°. (c) Corresponding transmittance spectrum of α-MoO_3 polarization color filter.

As the polarization changes in Figure 3.17a, b, the color in the square shows chartreuse (peak wavelength λ_p = 573 nm) at ϕ_p = 0° ($\hat{x}$) and turns to green (peak wavelength λ_p = 551 nm) at ϕ_p = 90° polarization ($\hat{y}$). Based on the principles of the FP cavity, the thickness of dielectric layer is an important factor determining the resonance peak wavelength. The polarization color filter could be designed to work across the visible range by tuning the thickness of α-MoO_3.

To verify the fitting of the refractive index of α-MoO_3 in the visible range, we fabricated an Ag/α-MoO_3/Ag cavity with several transferred α-MoO_3 flakes whose thicknesses vary from 300 to 500 nm. In this FP structure, the thicknesses of top and bottom Ag layers are set to t = 20 nm and b = 20 nm. Figure 3.18a,c shows the optical image in transmission-mode on $\hat{x}$ polarization and $\hat{y}$ polarization. Transmittance spectra is calculated using TMM as outlined in Chapter 2. Figure 3.18b, d show the plots of transmittance spectra as a function of α-MoO_3 thickness and the wavelength on $\hat{x}$ and

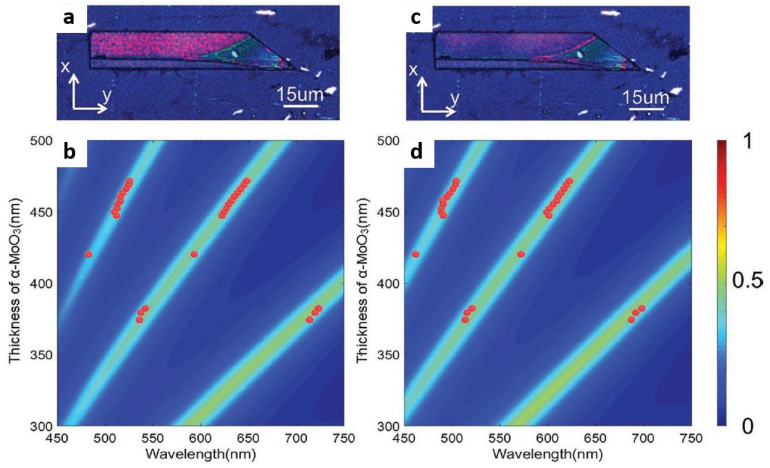

Figure 3.18. Optical image of α-MoO_3 polarization color filter with thickness t = 20 nm, b = 20 nm and h between 300 and 500 nm for (a) ϕ_p = 0° and (c) ϕ_p = 0°. Transmittance spectrum plotted as a function of wavelength and thickness of α-MoO_3 for incident (b) $\hat{x}$ polarization and (d) $\hat{y}$ polarization. The red spheres indicate the peak wavelengths of experimental results extracted from corresponding mapping experiment of several α-MoO_3 polarization color filters.

$\hat{y}$ polarizations, respectively. One can clearly see that the region of highest intensity in the visible regime changes from magenta to violet when the incident light polarization is switched from $\hat{x}$ polarization to $\hat{y}$ polarization owing to anisotropic optical properties of α-MoO_3, which can be represented as a blueshift in transmittance spectra as shown in Figure 3.18b, d.

CHAPTER 4

Anisotropic vdW materials for polarization-dependent photonics in IR

This chapter is mostly adapted from the following published articles:

- Song, X., Abedini Dereshgi, S., Palacios, E., Xiang, Y. and Aydin, K. "Enhanced Interaction of Optical Phonons in h-BN with Plasmonic Lattice and Cavity Modes. " *ACS Applied Materials & Interfaces*, 28 (11), pp.16725-16739 (2021) [27].
- Abedini Dereshgi, S., Folland, T.G., Murthy, A.A., Song, X., Tanriover, I., Dravid, V.P., Caldwell, J.D. and Aydin, K. "Lithography-free IR polarization converters via orthogonal in-plane phonons in α-MoO_3 flakes." *Nature Communications*, 11(1), pp.1-9 (2020) [54].

4.1. Chapter 4 highlights

In this chapter, emerging anisotropic vdW materials, hexagonal boron nitride (hBN) and α-MoO_3 are studied and their rich phononic properties are tailored to polarization-sensitive photonics in IR. hBN is regarded as a milestone in the investigation of light interaction with phonon polaritons in 2D vdW materials, showing significant potential in novel and high-efficiency photonics devices in the mid-infrared region. Here, we investigate a structure composed of Au grating arrays fabricated onto a Fabry-Perot

(FP) cavity composed of hBN, Ge, and Au back reflector layers. The plasmonic FP cavity reduces the required device thickness by enhancing modal interactions and introduces in-plane polarization sensitivity based due to the Au array lattice. Our experiments show multiple absorption peaks of over 90% in the mid-infrared region and band stop filters with 80% efficiency using only a 15 nm hBN slab. Moreover, mode interaction with experimental coupling strengths as high as 10.8 meV in the mid-infrared region is investigated. Anticrossing splitting ascribed to the coupling of optical phonons to plasmonic modes can be tuned by the designed geometry which can be tailored to efficient response band engineering for infrared photonics. We also show that in practical applications involving wet transfer of hBN thin films, the contribution of minor optical phonon modes to resonant peaks should not be ignored, which originate from defects and multicrystallinity in the hBN slab. hBN is also analyzed by highlighting birefringence introduced by grating design on top of it.

α-MoO_3 has been reported as a semiconducting biaxial vdW material capable of sustaining naturally orthogonal in-plane phonon polariton modes in IR. In this study, we investigate the polarization-dependent optical characteristics of cavities formed using α-MoO_3 on Ge-Au stacks to extend the degrees of freedom in the design of IR photonic components exploiting the in-plane anisotropy of this material. Polarization-dependent absorption over 80% in a multilayer Fabry- Perot structure with α-MoO_3 is reported without the need for nanoscale fabrication on the α-MoO_3. We observe coupling between the α-MoO_3 optical phonons and the Fabry-Perot cavity resonances. Using cross-polarized reflectance spectroscopy we show that the strong birefringence results in 15% of the total power converted into the orthogonal polarization with respect to incident wave.

These findings can open new avenues in the quest for tunable polarization filters and low-loss, integrated planar IR photonics and in dictating polarization control, as well as camouflage and radiative cooling devices.

4.2. Birefringent metamaterial: Interaction of anisotropic optical phonons in hBN with plasmonic modes

4.2.1. Motivation

Most research studies on hBN concentrate on the natural hyperbolicity of hBN considering in-plane phonons and the investigation of normal phonon modes in hBN remains scarce Because the out-of-plane phonon modes fall within the atmospheric window of 8-14 μm, improving research on these modes can be consequential for infrared photonics. As an effort to address this matter, we study modal interaction details of normal optical phonons with plasmonic resonance modes and apply our findings to infrared perfect absorber and filter applications. Optical phonons (OPhs) refer to quantum vibrational modes of the composed atoms found in a crystalline material with a lattice basis [111, 112, 113], which is also known as optical normal modes in classical mechanics [114, 115]. While interacting with incident light, phonon polaritons are adopted to describe the hybrid quasiparticles of optical phonons and photons depicting the collective phonon oscillations with hybridized electromagnetic fields. In contrast to hyperbolic phonon polaritons (HPhP) that require momentum matching techniques, the strong coupling of optical phonons can be achieved in a relatively easier way; by direct illumination which can be enhanced by integrating the phonon-supporting material (hBN here) with sub-wavelengt nanostructures. The strong interaction

of phonons with incident light, along with its plasmonic counterpart, plays an important role in the exploration and application of novel high-efficiency and lowloss optical nanodevices, especially in the mid-infrared range [116, 117, 118].

4.2.2. Optical model of hBN.

hBN is uniaxial (in-plane symmetry, $\varepsilon_{xx} = \varepsilon_{yy}$) and its permittivity tensor is has diagonal values ε_{xx} and ε_{zz}. Considering the polycrystalline nature and defects in transferred hBN, not only the main phonon modes of both orientations are considered here but als the minor optical phonons are taken into account. The dielectric function is illustrated below [119] which is a Lorentz model similar to Equation 2.49,

$$\varepsilon_{jj} = \varepsilon_{\infty,j} + \frac{S_{1,j}^2}{\omega_{TO1,j}\omega_{LO1,j} - \omega^2 - i\omega\Gamma_{1,j}} + \frac{S_{2,j}^2}{\omega_{T2,j}\omega_{LO2,j} - \omega^2 - i\omega\Gamma_{2,j}}, \tag{4.1}$$

where j represents the direction $\hat{x}$ or $\hat{z}$, corresponding to the inplane (perpendicular to c-crystal plane) and out-of-plane (parallel to c-crystal axis) axis of the h-BN crystal, respectively. The symbols used here are the same as the ones in Chapter 2. The parameters used for simulations are listed in Table 4.1.

Table 4.1. Corresponding Parameters Used in Equation 4.1 to obtain the permittivity tensor of hBN [119].

	ε_∞	$\omega_{TO1,2}$ (cm)$^{-1}$	$\omega_{LO1,2}$ (cm)$^{-1}$	$S_{1,2}^2$ (cm)$^{-2}$	$\Gamma_{1,2}$ (cm)$^{-1}$	**Phonon mode**
ε_{xx}	4.95	767	778	1.23×10^5	35	2-*Phx*
		1367	1610	3.49×10^6	29	1-*Phx*
ε_{zz}	4.1	783	828	3.26×10^5	8	1-*Phz*
		1510	1595	1.04×10^6	80	2-*Phz*

Other than the two main phonon modes (marked 1-*Phx* or 1-*Phz*) related to strong infrared lattice vibrations, two minor optical phonon peaks (marked 2-*Phx* or 2-*Phz*) are considered as well. These additional modes take several nonideal factors into account, including multicrystallinity misorientation, defects, and wrinkles in the wet-transferred hBN thin film [120, 121]. The wrinkles are also evident in Figure 4.1d.

4.2.3. Experiment and simulation methods

To establish the interaction of optical phonons in hBN with incident electromagnetic and plasmonic modes, resonant Au gratings (40 nm thick) are designed and fabricated on the top of hBN slabs (15 nm), which are integrated onto a Fabry Perot (FP) cavity composed of a germanium (Ge) spacer stacked on a totally reflecting background metal (BGM), as schematically illustrated in Figure 4.1a. Since we aim to study the responses of the plasmonic cavity and optical phonons of hBN, the spacer layer is chosen as Ge which has nondispersive refractive index ($n_{Ge} = 4.007$) within the wavelength range of interest, 5-16 μm [122]. When incident E-field from the top side is polarized perpendicular to Au gratings, the polarization angle ϕ_p is marked as zero. Due to total reflection of the BGM, transmission can be neglected, and absorption is calculated as $A = 1 - R$, where R is reflectance.

Experiment.

Au and Ge Deposition. For both Au and Ge films, physical vapor deposition (PVD) is used. Au deposition is performed in an AJA e-beam evaporator system where base and deposition pressure were 9×10^{-7} and 6×10^{-6} Torr respectively. The deposition rate was set to 0.5 nm/s for Ge deposition and the auto e-beam 500 system was used,

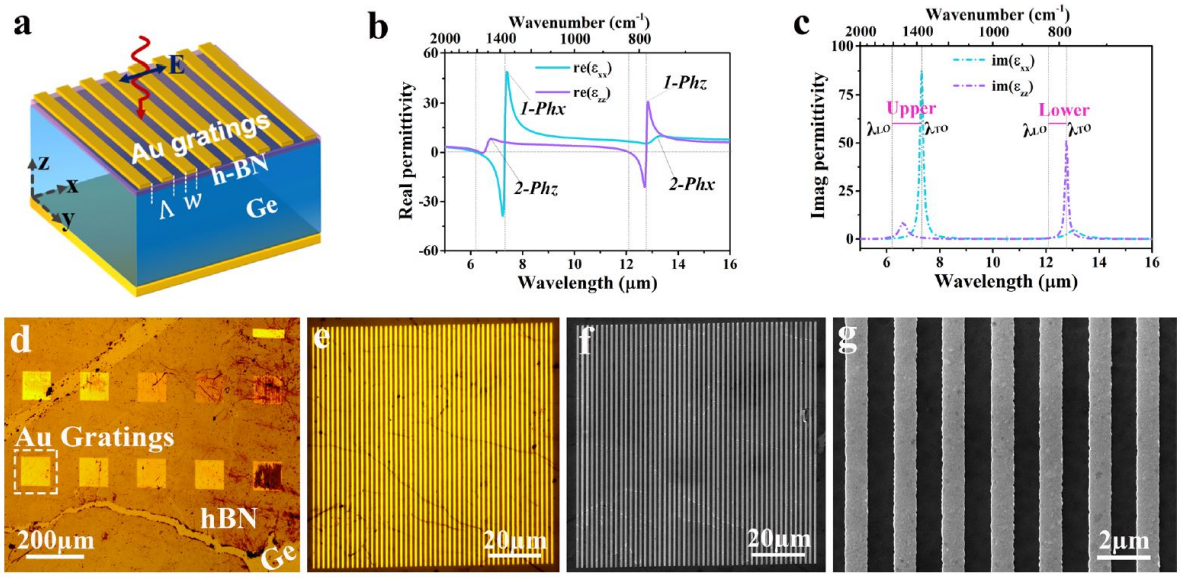

Figure 4.1. (a) Schematic of Au gratings on the hBN slab integrated with a Ge spacer as the FP cavity and background metal are at the bottom. Au gratings are parallel to $\hat{y}$ and the original E-field is polarized perpendicular to Au gratings. (b,c) Real and imaginary parts of the permittivity of h-BN. Here, "1-*Phx*" and "1-*Phz*" refer to the main modes of in-plane and out-of-plane optical phonon modes, while "2-*Phx*" and "2-*Phz*" refer to minor modes, respectively. "upper" and "lower" regions refer to the corresponding upper and lower RS bands. (d) Optical image of Au-grating arrays on a multicrystalline hBN slab with defects and cracks. The Au patch has an area of 100 $\times$ 100 μm^2 with 100 μm space between adjacent patches. (e) Optical image of one specific patch and (f) its corresponding SEM image. (g) Larger magnification of Au-grating morphology in SEM. The thickness of hBN is measured by AFM to be 15 nm.

where base and deposition pressure were 2×10^{-6} and 9×10^{-6} Torr, respectively. The deposition rate of this sublime material was held within 0.13 and 0.17 nm/s during the deposition.

hBN Slab Transfer. Multilayer hBN films grown on copper coil were purchased from Graphene Supermarket. The copper was etched, and the floating hBN was transferred onto the desired substrate [123]. Several rinsing processes in deionized water were

carried out before transformation. After transfer, the samples were dried to make hBN adhere onto the Ge surface and remain unchanged after being immersed in acetone overnight during the subsequent grating fabrication process.

Au Grating Fabrication. For fabrication of Au gratings, first, a double PMMA spin coating was selected as the resist. A spin coatin of PMMA 495-C was followed by PMMA 950-A, both of which were spin-coated for 45 sec at 4000 rpm. The baking time for them was 30 and 90 s, respectively. Afterward, the pattern was introduced to the films using a SEM FEI Quanta 650 e-beam lithography system. After developing for 75 sec, an Au thin film ($\sim$40 nm) was deposited using an Auto e-beam 500 system under similar conditions and the sample was left in acetone overnight for resist removal.

Characterization. Mid-infrared reflectance measurements were undertaken in fourier transform infrared (FTIR) spectrometer, with a Hyperion 2000 IR microscope coupled to a Bruker Vertex 70 FTIR spectrum. The spectra were collected with a 4 cm^{-1} spectral resolution and spatial resolution defined by the internal adjustable aperture of the microscope. The measurement area was within the Au grating region, and the polarization angle was controlled by a built-in polarizer in the incident wave route, similar to Figure 2.2a. The measured spectral range was set from 600 to 2000 cm^{-1} (5-16.6 μm).

Simulation methods.

All of the simulations are carried out with TMM and lumerical FDTD software by importing Equation 4.1 as the optical model of hBN. the coupled oscillator model (Equation 2.44 with ω in cm^{-1}) is used to obtain coupling strength of plasmonic and optical phonon modes.

4.2.4. Coupling of Au grating plasmons to OPhs in hBN

In order to investigate the coupling mechanism of optical phonons from both in-plane and out-of-plane directions in hBN, first the influence of Ge spacers and Au-grating arrays on absorption spectrum is discussed using samples with/without the Au grating array. Au gratings provide a large enhancement of electric field confined in the direction perpendicular to the hBN layer and thus enhance the interaction of photons with both in-plane and out-of-plane optical phonons. Ge spacers with various thicknesses ($t_{Ge} \approx$ 335, 470, and 665 nm) are deposited to investigate absorption properties and coupling mechanisms (Figure 4.2b).

The impact of Ge thickness is illustrated in Figure 4.2, capturing the additional effect of Au gratings on the proposed FP cavity. As shown in Figure 4.2a-c for the structure without Au gratings, a narrow and sharp peak is evident near $\lambda_{TO,upper}$ ($\sim$7.2 μm), corresponding to the resonance of main in-plane optical phonons (1-Phx) excited directly by incident photons. Increasing t_{Ge} up to 1 μm, only a fundamental mode of FP resonance exists in the wavelength range of interest, and higher orders are expected to appear for thicker spacers. The highest absorption can be obtained when the cavity resonance approaches $\lambda_{TO,upper}$ where $\mathcal{R}e(\varepsilon_{xx})$ is near zero. As measured, the absorption is as high as 90% near $\lambda_{TO,upper}$ with a 15 nm hBN layer on the Ge spacer with t_{Ge} = 470 nm. Absorption spectra measured from FTIR agree quite well with those from FDTD simulation. It should be noted that in FTIR measurements, the incident angle is defined by weighted average incident angle of Cassegrain objectives, which is approximately 15° (for 15× Cassegrain objective) yielding a small out-of-plane E-field

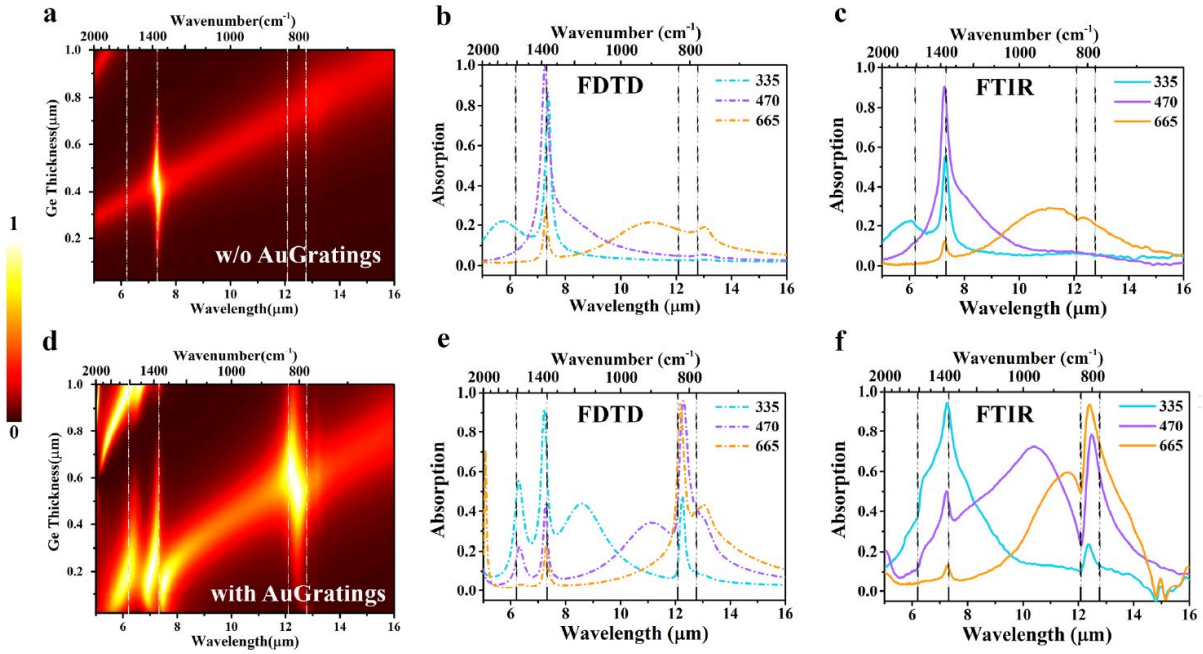

Figure 4.2. Contour map of FDTD simulated absorption as a function of wavelength and Ge thickness (a) without and (d) with Au gratings on the top of hBN slab. (b,c) Simulated and measured absorption spectra of the structure without Au gratings for various Ge thicknesses (t_{Ge}). (e,f) Simulated and measured absorption spectra of the structure with Au gratings on the top for various Ge thicknesses (t_{Ge} = 335, 470 and 665 nm, respectively), as all marked in the insets of (b,c,e,f). In these fabricated samples, hBN thickness t_{hBN} = 15 nm, periodicity Λ = 1.3 μm, grating ratio p = 0.5, and grating width $w = p, \Lambda = 0.65$ μm.

component. The small extinction value from the out-of-plane mode of a thin hBN slab results in negligible absorption under such a minor incident angle.

Once Au-grating arrays parallel to y-axis are introduced, a pronounced anticrossing curve indicating strong coupling enhancement of out-of-plane phonon modes shows up in the lower RS band when t_{Ge} increases. Two other anticross splitting phenomena are observed simultaneously around upper RS bands (Figure 4.2d). These anticrossing

behaviors indicate the coupling of optical phonons from both in-plane and out-of-plane directions with the geometrical modes from structure. The first and second modes in the upper RS band which interact with phonon modes in Figure 4.2d are attributed, respectively, to lattice and cavity plasmonic modes. Due to the enhanced field intensity as a result of the addition of lattice modes [124], the required FP spacer thickness for the strong coupling of in-plane OPhs (1-Phx) is smaller than that for an Au-free condition, which implies a thinner device requirement for strong modal interaction. Besides, the redshift of all resonances with respect to t_{Ge} increase is in coincidence with the situation without the hBN layer As a result of this general redshift, higher order modes red-shift to wavelengths higher than 5 µm and can be noticed in the top left corner of Figure 4.2d when $t_{Ge} > 0.6$ µm.

To validate the effect of t_{Ge} on modal interaction and its corresponding role in strong coupling of phonon modes from both orientations for the structure with Au-grating arrays on the top, samples are fabricated accordingly with selected Ge thicknesses. Absorption values obtained from FDTD and FTIR for samples (t_{Ge} = 380, 470, and 665 nm) with Au gratings are shown in Figure 4.2e,f for comparison. Both resonances verified from FTIR measurements display a reasonable consistency with FDTD simulation results, validating the enhanced coupling of both optical phonon modes. As t_{Ge} increases from 335 to 665 nm, the coupling enhancement from in-plane OPhs (1-Phx) gradually decreases, which, on the contrary, increases for the out-of plane counterpart. At t_{Ge} = 665 nm, the lattice mode approaches the out-of-plane OPh (1-Phz) mode where these modes interact strongly and split within the lower RS band. Figure 4.2f infers a strong absorption in the upper RS band that peaks as high as 94.5% at 7.26 µm when t_{Ge} = 335

nm. There is also an evident 94% absorption at 12.4 μm when t_{Ge} = 665 nm. Other than high absorption in the two extremes of the chosen t_{Ge} values, the thickness between them (i.e., t_{Ge} = 470 nm) yields a strong coupling and splitting of the plasmonic lattice mode with 1-*Phz* modes. This phenomenon gives rise to a bandpass filter action at 12.1 μm in the reflected beam with a full width at half maximum (fwhm) value of 0.64 μm, and the resulting filtering efficiency defined as $\eta = 1 - (R_{min} / R_{max})$ is 71.4%.

Considering the response of both minor in-plane and out-of-plane phonon modes, the multicrystalline morphology and defects of the transferred hBN slab which originate from the wet transfer process, the minor modes too should be taken into account. Thus, the complex dielectric model illustrated in Figure 4.1b,c is adopted in the simulations to model the experiments more accurately. It should be noted that fabricating samples with several t_{Ge} values is toilsome with (PVD), and it is almost impossible to maintain the experiment conditions such as hBN and grating details acceptably identical for all the samples. Therefore, other features are identified to study the mode-coupling phenomena in further detail. The coupling enhancement of OPhs in h-BN from both in-plane and out-of-plane orientations can be tuned by Au-grating parameters such as filling factor (p) and unit periodicity (Λ). In order to examine the coupling features experimentally, several samples with different p and Λ values were fabricated and are reported in the following sections. In our experiments, gratings with various filling factors and periodicities are fabricated on the same sample in order to maintain identical conditions for hBN and Ge layers, and t_{Ge} is chosen to be 470 nm to observe pronounced coupling and absorption peaks for OPh modes in both RS bands. The fabricated array

is kept constant at 100 $\times$ 100 μm^2 to maintain the measurement accuracy, and the gap between adjacent arrays is maintained at 100 μm, as displayed in Figure4.1d.

Figure 4.3a presents the tuning effect of grating filling factor ($p = w/\Lambda$) to coupling enhancement while maintaining the fabricated periodicity constant (Λ = 1.3 μm). Highlighted markers are extracted from the resonant peaks measured by FTIR and agree quite well with the simulated absorption contour. Owing to such a thicker spacer (t_{Ge} = 470 nm), the plasmonic lattice mode is located beyond the upper RS band and red-shifts as the filling factor increases. As a result, the wavelength referring to in-plane OPhs (1-*Phx*) resonance wavelength (marked by triangle $\triangle$) is constant near $\lambda_{TO,upper}$, while the absorption amplitude attenuates as p increases from 0 to 1 due to the covering of hBN with metal in the limit of p = 1. On the other hand, the coupling of out-of-plane OPhs (1-*Phz*) in the lower RS band leads to an obvious anticrossing transition [125] once the resonances shift across $\lambda_{TO,lower}$.

Anticrossing behavior from enhanced coupling of both OPhs is expected when periodicity is modified (Λ = 0.02-4 μm), while keeping the filling factor constant ($p \approx$ 0.4), as shown in Figure 4.3b. Once again, the highlighted markers of FTIR resonant peaks have a good agreement with FDTD simulations. The coupling strength near 12.2 μm in Figure 4.3a can be examined by a fitting oscillator model (Equation 2.44) to track the peaks, modal overlap, and the subsequent splitting of the plasmonic and 1-*Phz* modes. For Figure 4.3a, (Appendix B), the spectral splitting at zero detuning is 1.3 and 1.31 μm for the oscillator model and experimental results, respectively, which correspond to a 10.8 meV (87 cm^{-1}) oscillator strength at 101.3 meV (816.98 cm^{-1})

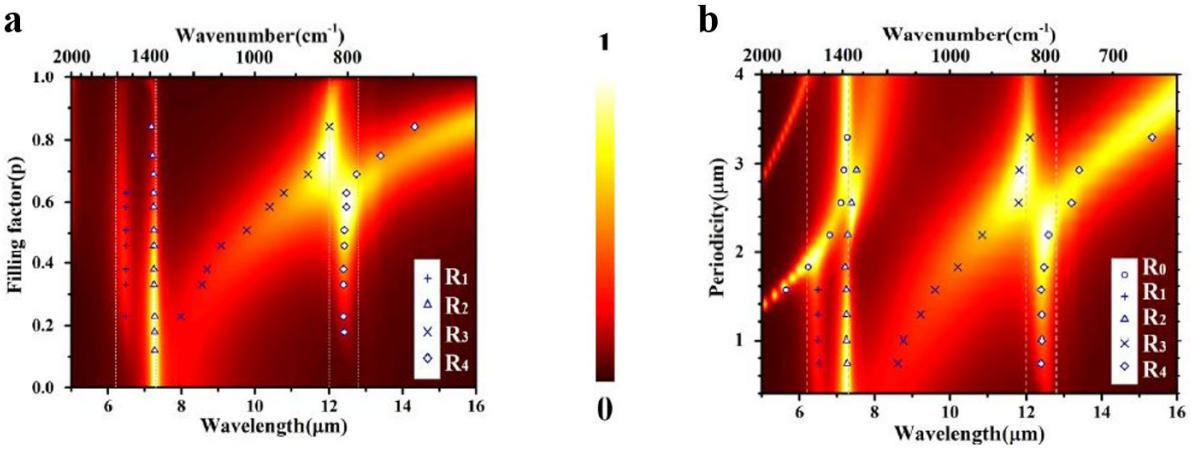

Figure 4.3. Resonance conditions for the FP structure with Au gratings on top. (a) Absorption map of structure versus wavelength and filling factor ($p = w/\Lambda$), with a constant periodicity (Λ = 1.3 μm) and changing grating width w. All the markers are resonant positions obtained experimentally from FTIR measurements. (b) Absorption map of the structure versus wavelength and periodicity Λ (μm), with constant filling factor of Au gratings ($p \approx 0.4$). The contour maps of are calculated with FDTD simulation, and the dots are the extracted resonant positions from FTIR measurement results at t_{Ge} = 470 nm.

central energy. Similarly, for Figure 4.3b where the plasmonic mode interacts with 1-*Phz* mode, the oscillator model estimates a spectral splitting of 1.1 μm which corresponds to a coupling strength of 9.4meV (76 cm^{-1}) at 103.1 meV (831.50 cm^{-1}) central energy. For small filling factor of p = 0.18 in Figue 4.3a, absorption as high as 86% is measured experimentally at 7.26 μm ascribed to 1-*Phx*. On the contrary, at a larger value of p = 0.75, absorption values as high as 89% and 90% are measured at 11.73 and 13.39 μm, due to the overlap of 1-*Phz* and plasmonic lattice resonance modes. This modal overlap and splitting underscore a bandpass filter action at 12.2 μm in reflected beam with a fwhm value of 0.52 μm and filtering efficiency of η = 53.3%. When p = 0.58, at 12.1 μm, η = 68.8%, and fwhm = 0.095 μm. Experimental results of Figure 4.3b for

different Λ values demonstrate similar absorption characteristics. Absorption values reach as high as 94 and 93%, respectively, at 7.38 and 13.33 μm when Λ = 2.6 μm. Both absorption peaks are results of modal overlap, the former between plasmonic cavity and 1-*Phx* modes, and the latter between plasmonic lattice and 1-*Phz* modes. The splitting for 1-*Phx* and plasmonic modes is negligible (i.e., weak coupling) and hence are not fitted to the oscillator model. The overlap of 1-*Phz* and plasmonic modes results in a bandpass filter with fwhm = 0.51 μm and η = 58.8%. For Λ = 1.8 μm, high absorption of 75.4% is also evident at 6.22 μm ascribed to 2-*Phz* OPh mode. At 12.1 μm, this curve demonstrates a bandpass filter action with fwhm = 1.44 μm and η = 80%. These results demonstrate that multiple high absorption peaks at several wavelength values as well as bandpass filter action near λ_{TO} wavelengths are obtainable by tuning the thickness of layers, geometrical parameters of the grating layer and modal overlap engineering.

4.2.5. Minor fabrication and simulation discrepancy

The intensity discrepancy of resonant peaks between measurement and simulation cannot be overlooked, which mainly originate from fabrication processes. Slight deviation in grating width and edge roughness are inevitable due to e-beam lithography and lift-off processes. Therefore, it is challenging to keep the value of p precise and constant in the experimental stage, and here, we have taken this effect into account by an error margin of $p = 0.4 \pm 0.05$ for nonidealities in the discussion section. Furthermore, wrinkles and defects in the transferred hBN thin film play a critical role in dictating the ultimate quality of Au gratings, which contributes to the two extra minor phonon

modes considered in the dielectric constants of hBN. Moreover, the imaginary part of the Ge layer is predominantly determined by the e-beam evaporation process which gives an amorphous film. In the case of thicker Ge films, larger pinholes may occur, which can explain the discrepancy between measured and simulated third peak (R^3) located between $\lambda_{TO,upper}$ and $\lambda_{TO,lower}$.

4.2.6. Plasmonically enhanced anisotropy in hBN

To study the polarization-dependence of hBN and verify the contribution of specific phonon modes to total absorption, power absorption per unit volume (P_{abs}) and its corresponding distribution in hBN and the whole structure are investigated through simulations. The absorption from both orientations is optimized to be as high as possible, with the parameters being defined in the caption of Figure 4.4. In general, Pabs for the whole structure from 5 to 16 μm looks the same as the absorption spectrum.Figure 4.4a suggests that incident energy is dissipated mainly in the hBN slab and the role of optical modes from in-plane (hBNx) and out-of-plane (hBNz) orientations in absorption is clear in the resonant peaks. In addition, P_{abs} distributions at the cross section of the hBN slab are illustrated in Figure 4.4b,c. The distribution of fields for OPhs from both orientations is enhanced at grating edge domains in opposite directions at 7.2 and 12.7 μm, respectively, exhibiting outward and inward propagation behavior correspondingly. This distinction is due to the difference in the dielectric constants in $\hat{x}$ and $\hat{z}$ directions in these two wavelengths, which demonstrates the strong anisotropy of hBN visually. The enhanced fields shown in this figure result in remarkably high absorption values in a 15 nm hBN layer as previously discussed.

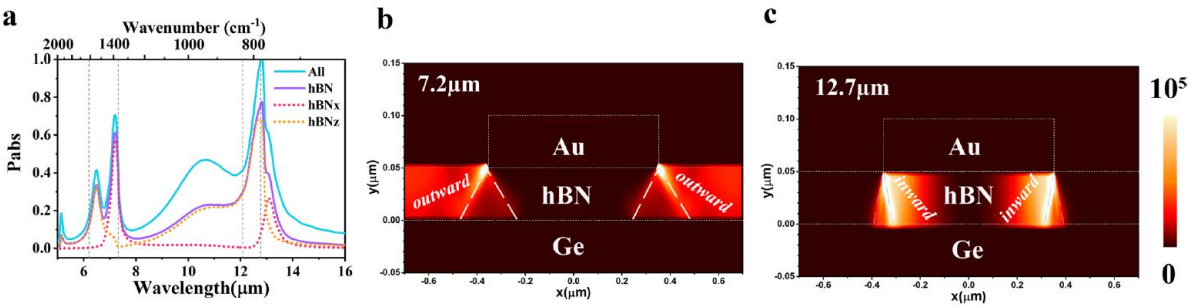

Figure 4.4. (a) Comparison of P_{abs} in the whole structure (blue line, marked as "All") and in the hBN layer (purple line, marked as "hBN") and P_{abs} originating from in-plane (red dotted line, marked as "hBNx") and out-of-plane (orange dotted line, marked as "hBNz") phonons in the hBN layer only. (b,c) The Pabs distribution in in-plane and out-of-plane orientations at the cross section, showing the distribution of the fields at the two OPhs resonant wavelengths 7.2 and 12.7 μm, respectively. Here, the structure has the following parameters: t_{Ge} = 500 nm, t_{hBN} = 50 nm, Λ = 1.4 μm and p = 0.5.

The polarization sensitivity of the discussed resonances is investigated, as displayed in Figure 4.5, which is another advantage of patterned layer besides enhanced modal interaction, which dictates polarization sensitivity. Strong interaction of OPhs of hBN from both orientations can be excited when incident E-field is perpendicular to Au gratings (polarization angle $\phi_p = 0$). However, the enhanced interaction vanishes when polarization switches parallel to Au gratings ($\phi_p = 90$), which is ascribed to a suppressed coupling in this scenario where gratings act as reflectors rather than field enhancement hotspots [126]. In this case, the z component of E-field is negligible due to almost normal incidence, and no scattering takes place in gratings and the OPh modes cannot be excited efficiently. The coupling of minor out-of-plane OPh (2-*Phz*) is enhanced when the polarization angle increases from 0 to 90 and attenuates from 90 to 180 for t_{Ge} = 650 nm. These results suggest that the coupling of main optical phonons from both

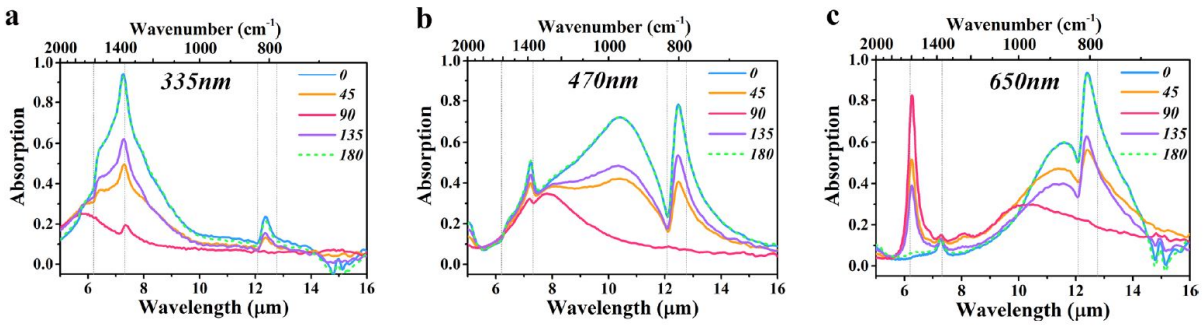

Figure 4.5. Polarization sensitivity measurement results of samples with t_{Ge} = 335 (a), 470 (b), and 650 (c) nm. "0" stands for the case where polarization is perpendicular to Au gratings (ϕ_p = 0), and "90" represents polarization along to Au gratings (ϕ_p = 90). For fabricated samples, t_{hBN} = 15 nm, Λ = 1.3 μm, p = 0.5, and $w = p\Lambda$ = 0.65 μm.

in-plane and out-of-plane is insensitive to the oblique incidence, which has significant potential in practical applications.

4.3. Naturally birefringent vdW material: Lithography-free IR polarization-sensitive photonics with α-MoO_3

4.3.1. Motivation

Infrared wavelength range encompasses an atmospheric window between 3 to 5 and 8 to 14 μm that can be critical for deep space sensing applications. However, realizing these components in infrared (IR) remains challenging due to the scarcity of material systems that exhibit strong birefringence in this frequency range. Bulky polarizers and wave plates used for the second atmospheric window in infrared (8 - 14 μm) have been reported in the past decades, the most notable ones being ZnSe and ZnS wire grid polarizers [14, 15] that are standard optical components for polarimetry in infrared. Besides ZnSe and ZnS, there are reports of other bulky elements such as silicides

(WSi) [16] and birefringent polymers [17]. Analoguous to their VIS counterparts, these wave plates are bulky and cannot be grown on arbitrary substrates and are not a viable option on-chip IR photonics. In this chapter, vdW materials are identified as a solution for on-chip IR photonics thanks to strong dispersion near their optical phonon resonances, using both metamaterial-introduced birefringence and naturally birefringent vdW materials.

In Chapter 4 it was shown that hBN does not have in-plane anisotropy and in-plane anisotropy can be achieved within hBN via fabrication [127, 27]. In the context of hyperbolic plasmon polaritons (PPs) in vdW materials, graphene and black phosphorus (BP) are the most widely studied materials. While graphene does not support in-plane anisotropy, simulation efforts have demonstrated that introducing anisotropy through asymmetric patterning achieves in-plane birefringence [128]. BP supports weak in-plane anisotropy and hence birefringence in IR [50, 129, 53]. In order to enhance anisotropy, BP can be patterned to support anisotropic plasmons which are shown to modify the polarization of the reflected or transmitted beam at IR frequencies [70, 130], similar to the case of borophene for VIS-NIR in Chapter 3. However, adding a substrate significantly deteriorates the amount of polarization rotation, as well as the intensity of the output, especially for the reflected beam [129]. In order to boost the in-plane anisotropy and ameliorate the effect of the substrate, BP was considered in the free-standing form, rendering such devices impractical. Besides, in case of patterned vdW materials, due to the fast scattering times associated with ligh-telectron (Ohmic) and light-crystal vibration coupling, losses are inherently high for PPs and PhPs [13]. Natural in-plane hyperbolicity present in the vdW α-MoO_3, featuring three distinct

RS bands, results in a variety of different hyperbolic behaviors in the long-wave IR [105, 131]. The OPhs supported by MoO_3 offer a platform to dictate the polarization in this spectral range. OPhs can be excited by direct illumination and obliterate the requirement of costly lithography techniques. Here, we experimentally demonstrate that the in-plane hyperbolicity of α-MoO_3 supports polarization-dependent resonant absorption (polarization filter) by optical phonons (OPh) and polarization conversion and wave plate action in IR when integrated into a FP cavity.

4.3.2. α-MoO_3 optical model and the FP configuration

The strong anisotropy in α-MoO_3, originating from lattice anisotropy, gives rise to three distinct lattice modes along the three orthogonal principle crystal directions leading to its naturally occurring in-plane hyperbolicity. α-MoO_3 is an orthorhombic crystal featuring three different symmetries for oxygen atoms that give rise to the biaxial optical properties (Figure 4.6a) [105, 132]. Since α-MoO_3 can be exfoliated along the [010] crystal direction, this is dubbed the $\hat{z}$ direction (optical axis). Following the established convention of crystallographic directions in the literature, the $\hat{x}$ and $\hat{y}$ directions represent the [100] and [001] directions, respectively[105].

Since OPhs dominate the optical characteristics of α-MoO_3 in the mid-infrared, the complex permittivity can be described by phenomenological Lorentz function using Equation 4.2 which is repeated below. The parameters are taken from [133], summarized in Table 4.2.

$$\varepsilon_{jj} = \varepsilon_{\infty,j} \prod_{m=0}^{n} \left(\frac{\omega_{LO,jm}^2 - \omega^2 - i\omega\Gamma_j}{\omega_{TO,jm}^2 - \omega^2 - i\omega\Gamma_j}\right), \qquad j = x, y, z. \tag{4.2}$$

Table 4.2. Corresponding Parameters Used in Equation 4.2 to obtain the permittivity tensor of α-MoO_3 [133].

	ε_∞	m	$\omega_{TO,m}$ $(\text{cm})^{-1}$	$\omega_{LO,m}$ $(\text{cm})^{-1}$	Γ_{jm} $(\text{cm})^{-1}$
ε_{xx}, [100]	5.78	1	506.7	534.3	49.1
		2	821.4	963	6
		3	998.7	999.2	0.35
ε_{yy}, [001]	6.07	1	544.6	850.1	9.5
ε_{zz}, [010]	4.47	1	956.7	1006.9	1.5

As is the case for all polar crystals, the RS bands are bracketed by longitudinal (LO) and transverse (TO) optic phonons in each direction. The complex permittivity of α-MoO_3 is illustrated in Figure 4.6b and c, which outline the three successive RS bands in directions identified in Figure 4.6a as x, y, and z. First, we will analyze a FP structure composed of the layers demonstrated in Figure 4.6d (Au, Ge and α-MoO_3), characterized with a polarizer in the path of the incident beam.

4.3.3. Experiment and simulation

Multilayer structure fabrication. The multilayer FP structure was fabricated using physical vapor deposition (PVD) technique. Au was deposited using AJA eBeam Evaporator system and the base and deposition pressures were, respectively, 2×10^{-6} and 9×10^{-6} Torr. The deposition rate was 0.5 nm/s. Ge was similarly deposited using Auto eBeam evaporation system with base and deposition pressure of 2×10^{-6} and 5

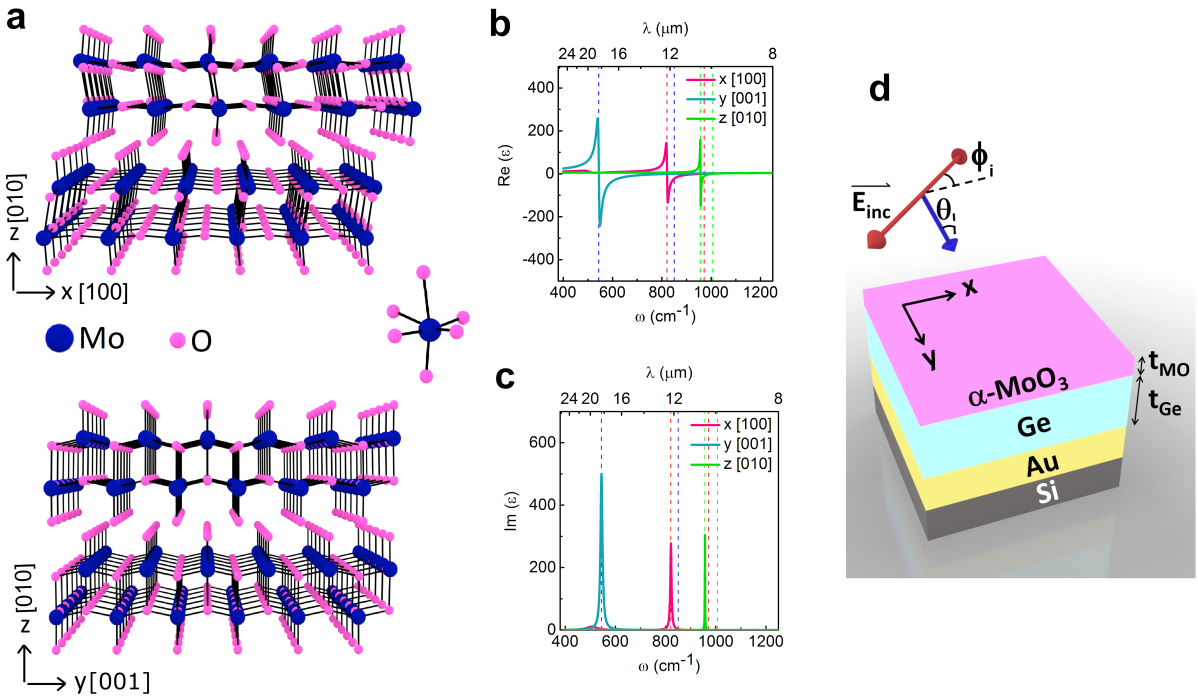

Figure 4.6. Optical characteristics of α-MoO3 and the structure under study. (a) Schematic representation of atomic orientation in the bulk structure of α-MoO_3 in xz and yz planes, (b) real and (c) imaginary parts of the dielectric function for α-MoO_3. (d) Schematic illustration of the investigated multilayer structure.

$\times 10^{-6}$ Torr. The deposition rate of this sublime material was held within 0.13 and 0.17 nm/s during the deposition.

α-MoO_3 fabrication and transfer. α-MoO_3 flakes were grown using low pressure PVD. For this process, 50 mg of MoO_3 (Sigma-Aldrich) powder was spread evenly within an alumina boat. This boat was placed within a 1-inch diameter quartz tube and at the center of a small Lindberg tube furnace. A 41 $inch^2$ rectangular piece of SiO_2/Si wafer (300 nm oxide thickness) was placed face-up downstream in a colder zone of the furnace. These pieces were suspended on top of an alumina boat and

were located roughly 4 cm from the center region. The pressure was maintained at 2.8 Torr with a carrier gas of O_2 at a flow rate of 25 sccm. The center of the furnace was then heated to 675 °C over a period of 25 min and then to 700 °C over a period of 5 min upon reaching 700 °C, the furnace was immediately opened, thereby quenching the deposition. A polycarbonate-based process was used to transfer the deposited flakes from the SiO_2/Si substrate to several different substrates. This process involved coating the SiO_2/Si substrate with a polycarbonate solution (5% polycarbonate to 95% chloroform by weight) at 2000 rpm for 60 s and baking at 120 °C for 1 min The substrate was then placed in water to allow the polycarbonate film and deposited α-MoO_3 flakes to naturally delaminate from the film. The polycarbonate film was then removed from the water and allowed to dry. Once dry, the polycarbonate film was placed onto the target substrate and baked at 170 °C for 15 min Finally, the target substrate was soaked overnight in chloroform and rinsed in isopropyl alcohol immediately thereafter to dissolve the polycarbonate film and leave only the α-MoO_3 flakes.

FTIR characterization. Mid-infrared reflectance measurements were taken with Hyperion 2000 IR microscope coupled to a Bruker Vertex 70 FTIR spectrum. For the FP structures MCT detector with KRS5 polarizer was used. The Cassegrain objective was 36× and the aperture dimensions were 50 by 50 μm^2 and the spectra were taken with 22.5° polarization steps. The polarizers used for the depolarization experiments were KRS5 wire grid polarizer from pike technologies and HDPE wire grid polarizer.

Simulation. The reflectance and E-field mode simulations were done using the TMM method outlined in Chapter 2 and FDTD solver.

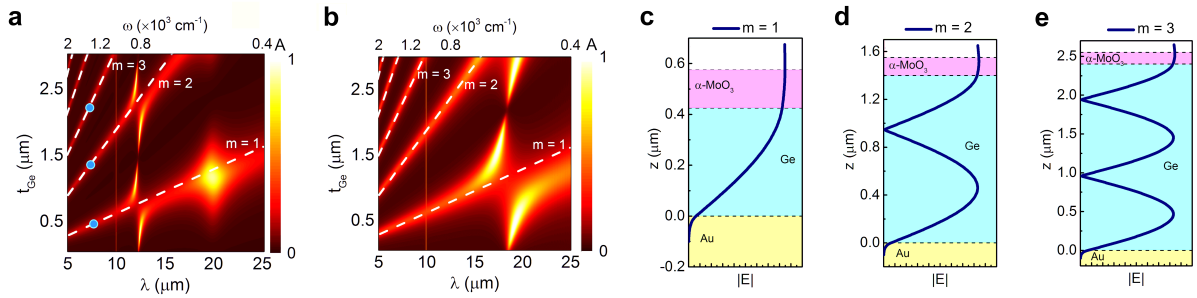

Figure 4.7. Dispersion of α-MoO_3 FP cavity with t_{Ge}. a Simulated dependence of total absorption on wavelength/frequency and Ge thickness (t_{Ge}) where α-MoO_3 thickness is kept constant at t_{MO} = 0.15 μm for (a) $\hat{x}$ (ϕ_p = 0°) and (b) $\hat{y}$ ($\hat{y}$ =90°) phonons. Simulated electric field magnitude $|\mathbf{E}|$ in the cross section of the studied multilayer system for t_{MO} = 0.15 μm and (c) t_{Ge} = 0.42 μm (m = 1), (d) t_{Ge} =1.4 μm (m=2) and (e) t_{Ge}= 2.4 μm (m = 3). Note that the scales in panels (c)-(e) are not the same due to the t_{Ge} difference. The dashed lines in panels (a) and (b) represent the FP mode orders. The dots on panel a mark the mode profile simulations of panels (c)-(e).

4.3.4. Polarization-dependent absorption

A simple FP structure like the one illustrated in Figure 4.6 can be used to shed light on the extraordinary IR characteristics of α-MoO_3. Ge is chosen to form the cavity due to its infrared transparency and lack of significant optical dispersion or loss within the frequency range of interest [122]. The absorption in the structure (equivalent to that of α-MoO_3, A_{MO}) is simply $A = A_{MO} = 1 - R$. Following the established tradition in this report, the polarization of the impinging radiation ($\phi_i = \phi_p$) is defined with respect to the $\hat{x}$. The impact of the Ge thicknesses (t_{Ge}) on the spectral absorption of the FP structure is illustrated in the TMM simulation results presented in Fig 4.7a.

The results for x-optical phonons (OPh_x) and y-optical phonons (OPh_y) are, respectively, provided in Figure 4.7a and b. It can be inferred from these two panels that as t_{Ge} increases, the absorption ascribed to FP modes (white dashed lines) redshifts up to

a certain thickness, they overlap with OPh_x (OPh_y) and an anti-crossing between the OPh and FP modes occurs. There are several higher-order FP modes that are marked by dashed lines that show similar behavior as that of the fundamental FP mode ($m = 1$). In Figure 4.7a and b oblique lines with steeper slopes represent higher-order FP cavity mode. In order to verify the FP modes, electric field magnitude ($|\mathbf{E}|$) simulations are provided in Figure 4.7c-e. A hypothetical vertical line at ω = 1300 cm^{-1} ($\lambda \approx 8$ μm) in Figure 4.7a or b would pass through 3 different modes marked on Figure 4.7a with blue dots. These dots represent m = 1, 2, and 3 FP modes, respectively, at three different t_{Ge} values, t_{Ge} = 0.42, 1.4, and 2.4 μm. The simulated $|\mathbf{E}|$ for the mentioned t_{Ge} values in the cross-section of the multilayer structure is illustrated in Figure 4.7c-e that verify the mode number engraved in the number of nodes within Ge layer. The electric field is similar for xz and yz cross sections. Also evident from Figure 4.7a and b are the x and y phonons, respectively, at 820 cm^{-1} (12.2 μm) and 550 cm^{-1} (18.2 μm), as well as their forbidden-crossing with the discussed cavity modes. The vertical absorption lines observed in the vicinity of 10 μm (ω = 1000 cm^1) in Figure 4.7a and b represent the OPh_z modes, which can be stimulated with off-normal excitation. For the purpose of our simulations this was achieved by setting the incident angle (θ) to 25°. This value of the incident angle is defined by the weighted average incident angle of the Cassegrain objectives used for FTIR measurements and OPh_z resonances are threfore expected to be excited in our experiments. Unlike OPh_x and OPh_y, OPh_z modes are orthogonal to the FP modes and thus they can be supported at the same frequency without strong modal interactions (e.g., anticrossing behavior).

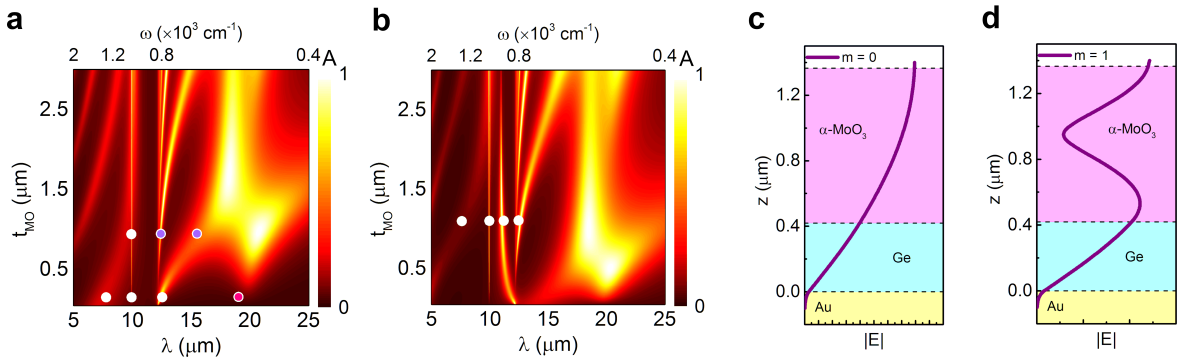

Figure 4.8. Dispersion of α-MoO_3 FP cavity with t_{MO}. Simulated absorption versus wavelength/frequency and α-MoO_3 thickness (t_{MO}) in the multilayer structure for constant Ge thickness (c) t_{Ge}= 0.42 μm and (d) t_{Ge} = 0.85 μm where $\phi_p = 0°$. Simulated electric field magnitude $|\mathbf{E}|$ in the cross section of the studied multilayer system for t_{MO} = 0.15 μm and t_{Ge} = 0.42 μm at (c) $\omega = 660\ \text{cm}^{-1}$ ($m = 1$) and (d) $\omega = 805\ \text{cm}^{-1}$ (m= 2). The dots in panels (a) and (b) mark the peaks in the absorption spectra of the fabricated samples, S1, S2, and S3 and the purple dots also represent the data points for the simulated field profiles in panels (c) and (d). The pink dot is the OPh_y mode which is excited when incident polarization $\phi_p = 90°$.

In order to observe the traces of OPh modes and distinguish them from the FP cavity modes in reflection (or absorption) results, two values of t_{Ge}, 0.42 and 0.85 μm, are identified from simulation results of Figure 4.7a. For t_{Ge} = 0.42 μm, absorption based on OPh modes is expected as opposed to t_{Ge} = 0.85 μm, where coupling of OPh modes to the FP mode m = 1 is anticipated (consider two horizontal line cuts from Figure 4.7a at the mentioned t_{Ge} values). At these two values of t_{Ge}, we also simulate the spectral characteristics of absorption in α-MoO_3 as a function of t_{MO} in Figure 4.8a, b when $\phi_p = 0°$.

An important take-away from Figure 4.8a and b simulations is the increased number of supported OPh modes in α-MoO_3 for larger t_{MO} values. As t_{MO} increases in Figure

4.8a, higher-order modes of OPhs also become accessible. At $\omega > 1000$ cm^{-1} ($\lambda < 10$ μm) since α-MoO_3 is highly dispersive, linear dependence of spectral absorption on t_{MO} is not expected. The oblique lines in this frequency range are FP-like (similar to Figure 4.7a and b) which are a result of cavity formed by air-MoO_3-Ge layers. As t_{MO} increases, these lines become increasingly nonlinear as they approach the RS bands. This is expected since the onset of RS bands is concomitant to substantial changes in the dielectric function, namely the vicinity of $\omega_{LO,z}$, $\omega_{LO,x}$, and $\omega_{LO,y}$. When 800 cm^{-1} $< \omega <$ 1000 cm^{-1} FP modes in α-MoO_3 cannot be supported in xz cross-section since the real part of the permittivity is negative in this range. Contrarily, for $\omega <$ 800 cm^{-1}, FP mode formed by air-MoO_3-Ge overlaps with m=1 OPh_x mode and the hybrid mode redshifts and higher-order OPh_x appears at 820 cm^{-1}. The hybrid mode with fundamental OPh_x and higher order OPh_x modes are marked with purple dots in Figure 4.8a and their corresponding $|\mathbf{E}|$ profiles are illustrated in Figure 4.8c and d. In these figures, field profiles for the m = 1 and m = 2 when t_{MO} = 0.95 μm and t_{Ge} = 0.42 μm at ω = 660 cm^{-1} ($\lambda \approx$ 15 μm) and ω = 805 cm^{-1} ($\lambda \approx$ 10 μm) are presented in Figure 4.8c, d, respectively, that support the presented mode discussion. Contrarily, in Figure 4.8b where t_{Ge} = 0.85 μm, Ge is thick enough to support FP modes formed by MoO_3-Ge-Au layers at $\omega <$ 820 cm^{-1} ($\lambda >$ 12 μm). Consequently, the m = 1 FP mode of Ge also interacts with the prior overlapping modes, m = 1 OPh_x and m = 1 FP of α-MoO_3. As a result of the three interacting modes (instead of two in the case of Figure 4.8a), an additional extinction peak appears near $\omega <$ 900 cm^{-1} which shows opposite trend to that of redshifting hybridized m = 1 OPh_x and m = 1 FP of α-MoO_3. The splitting observed around 18 μm is due to the OPh_x mode near this wavelength. At

xz cross-section, since α-MoO_3 is highly dispersive and has negative real permittivity values at fequencies between $\omega_{LO,z}$ and $\omega_{TO,x}$, the FP mode of α-MoO_3 is not present in this range. Contrarily, at $\omega < \omega_{TO,x}$ for xz cross-section (ϕ_p = 0°), α-MoO_3 has positive real permittivity values and its corresponding FP mode is feasible and it hybridizes with OPh_x modes. For yz cross-section (ϕ_p = 90°), similar behavior is expected except that the FP mode for α-MoO_3 is supported at $\omega < \omega_{TO,y}$.

In order to verify our predictions of the coupled FP-OPh modes in α-MoO_3 experimentally, three samples like the one schematically illustrated in Figure 4.6d were fabricated; sample S1 with t_{Ge}=0.42 μm and t_{MO}=0.15 μm, sample S2 with t_{Ge}=0.42 μm and t_{MO}=0.95 μm and sample S3 with t_{Ge}=0.85 μm and t_{MO}=1.1 μm. The spectral absorption measurements of these samples are presented in Figure 4.9 a-c, respectively.

Our FTIR spectra show that sample S1 (t_{Ge} = 0.42 μm and t_{MO} = 0.15 μm) supports polarization dependent absorption, as shown in Figure 4.9a as a function of ϕ_i between 0° to 180° in steps of 22.5°. In this figure, the peak at 800 cm^{-1} (12.5 μm) results from absorption from OPh_x in α-MoO_3, due to its presence at 0 and 180°. At $\phi_p = \phi_i$ = 90°, another peak in the vicinity of 550 cm^{-1} becomes apparent, corresponding to OPh_y (Figure 4.9a highlighted with blue arrow). The absorption peak at 1000 cm^{-1} originates from OPh_z excited as a result of the off-normal incident angle of the Cassegrain objective lens of FTIR. Finally, the broad peak located at a frequency higher than the z-LO phonons corresponds to the fundamental FP mode. The absorption tied to OPh_x reaches over 80% for ϕ_i = 0° and the corresponding full width at half maximum (FWHM) is 26 cm^{-1} (0.4 μm) centered at ω = 811 cm^{-1}. These results are consistent with values observed from the other two samples as shown in Figure 4.9b and c. In Figure 4.9b

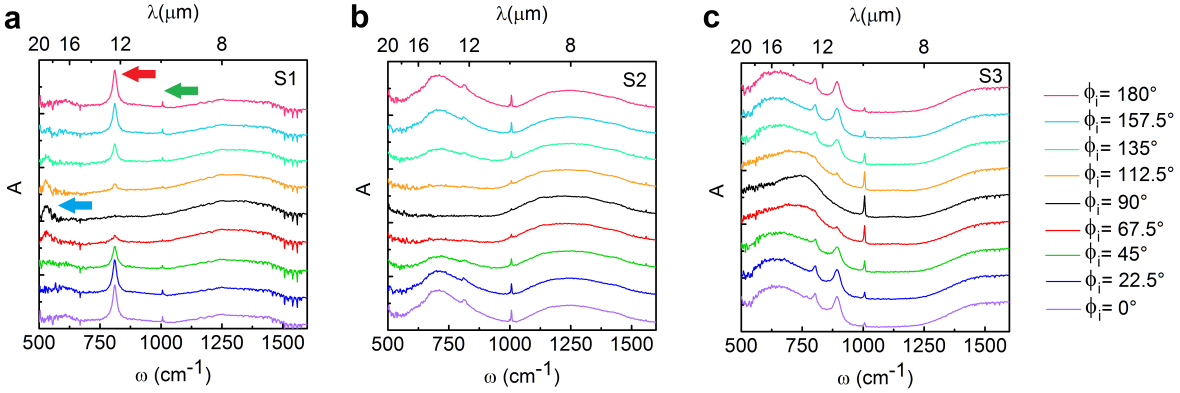

Figure 4.9. Experimental polarization-dependent absorption spectra of α-MoO_3. Polarization-dependent absorption spectra of fabricated samples with different Ge and α-MoO_3 thickness (t_{Ge} and t_{MO}, respectively), schematically illustrated in Figure 4.6 with thick Au, (a) S1, t_{Ge} = 0.42 μm and t_{MO} = 0.15 μm, (b) S2, t_{Ge} = 0.42 μm and t_{MO} = 0.95 μm, and (c) S3, t_{Ge} = 0.85 μm and t_{MO} = 1.1 μm. Incident polarization ($\phi_i = \phi_p$) is varied (bottom to top) from 0° to 180° in 22.5° revolution and illumination angle θ = 25° from FTIR. The green, red and blue arrows in (a) emphasize, respectively the OPh_z, OPh_x, and OPh_y. The peaks observed in each sample are marked on Figure F.3MOa, b.

(sample S2 with t_{Ge} = 0.42 μm and t_{MO} = 0.95 μm) we observe two peaks in the RS band near 750 cm^{-1}; the narrow one at 811 cm^{-1} is the higher order mode of the OPh_x (m = 2) and the broader one is the hybridized m = 1 OPh_x and m = 1 FP of α-MoO_3 that redshifts and broadens as t_{MO} increases. These two mode values are marked on Figure 4.8a (purple dots) and the corresponding field profiles outlining m = 1 and 2 are put forth in Figure 4.8c and d. The strong polarization dependence of these peaks confirms that they cannot be attributed to the Ge cavity, which due to its isotropic, cubic crystal structure exhibits no polarization dependence. Finally, the thickness parameters for the sample S3 (t_{Ge} = 0.85 μm and t_{MO} = 1.1 μm) is designed so that the fundamental cavity mode is red-shifted to longer wavelengths (lower frequency), to the vicinity of OPh_x modes. As a result, the m = 1 FP mode overlaps with m = 1 OPh_x and

m = 1 α-MoO_3 FP modes and coupling is evident by the splitting that occurs in the absorption spectra of Figure 4.9c. Thus, two distinct peaks at 811 and 720 cm^{-1} are present for the three coupled modes compared to only two for sample S2, which is in line with our predictions of the modal overlap. Finally, the dots on simulation results of Figure 4.8a, b mark the observed peaks in experimental results (Figure 4.9 4a-c) and they agree well with simulations. The experimental results demonstrate strong polarization-dependent absorption; Figure 4.9a represents 80% absorption and our simulations estimate 100% in the absence of experiment non-idealities.

From a more general perspective, Figure 4.9c indicates that one can tune absorption to over 70% (100% in simulations) approximately at 900 and 820 cm^{-1} demonstrating dual-band polarizationdependent perfect absorption action. Due to the flake roughnesses and small flake dimensions compared to the wavelength of test, the experimental results exhibit lower absorption peaks than simulations. The results presented in this section are also evidences of strong birefringence observed by polarization-sensitive absorption and filtering action, particularly at $\omega_{TO,x}$. The polarization filtering contrast, defined as $\Delta R = [R(\phi_i = 90) - R(\phi_i = 0)]/R(\phi_i = 0)$, is $\Delta R \approx 70\%$ for Sample S1 at 811 cm^{-1}. Benefitting modal overlap engineering by tuning the thickness of α-MoO_3 and Ge layers, polarization filtering can be realized at several frequency values other than $\omega_{TO,x}$, particularly at 705 and 892 cm^{-1} for samples S2 and S3, respectively. Theoretical values for filtering efficiency are above 90% for all of the absorption peaks.

4.3.5. Discrepancy of measurements and simulations

A few discrepancies are evident in the experimental results compared to FDTD and TMM simulations. For all the samples (Figure4.9a-c), OPh_z resonances distinctly reside close to 1000 cm^{-1} and show wide variations in intensity. We attribute this to the roughness of α-MoO_3 flakes as well variations in the high frequency dielectric constant, which will result in some difference in intensity as the polarization state is rotated. The rough surface acts to diffract the radiation, which in turn gives rise to **E** components aligned along the optical axis ($\hat{z}$) to excite OPh_z. In Figure 4.9c, the OPh_z absorption peak at 1006 cm^{-1} (9.94 μm) reaches to 53% and the FWHM and quality factor are 8.5 cm^{-1} (0.084 μm) and 119, respectively. The higher intensity of OPh_z peaks for samples S2 and S3 compared to S1 are due to the thicker α-MoO_3 flakes in these samples. Another major consequence of roughness is the suppression of OPh_y in samples S2 and S3 in all samples. In order for this mode to be observed, a flake should have negligible roughness in comparison to 18 μm free-space wavelength of the OPh_y. The largest flake dimensions are on the order of 30 to 40 μm, which together with the surface roughness of the α-MoO_3 flakes studied, hinder the observation of clear, high quality OPh_y and lower frequency OPh_x signals.

4.3.6. Wave plates in IR with α-MoO_3

A crucial outcome of in-plane anisotropic OPhs is strong intrinsic birefringence. Whilst ω_{TO} frequencies were tailored to absorbers and polarization filters in the previous section, off-resonance frequencies ($\omega \neq \omega_{TO}$) where absorption drops, are suitable for waveplates and polarization conversion applications. The multiple RS bands of

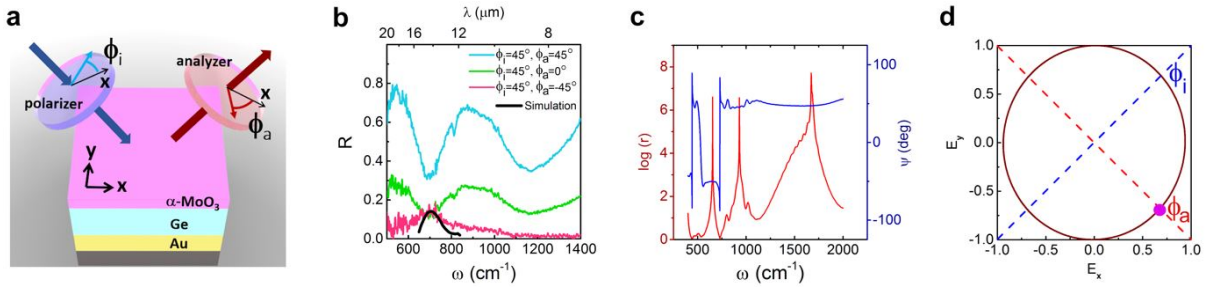

Figure 4.10. RS band enhanced birefringence in α-MoO_3. a Schematic of depolarization experiment, (b) reflectance of sample S2 for different analyzer values ϕ_a when polarizer is set to ϕ_i = 45°, the black curve is the simulated intensity for ϕ_a = -45°. (c) Simulated polarization ellipse characteristics, ellipticity (r) and polarization ellipse major axis angle (ψ). (d) Simulated polarization ellipse of reflected beam at ω = 727 cm^{-1} which represents circularly polarized light. The purple dot represents an example of the $|\mathbf{E}|$ value from the reflected polarization ellipse at ω = 727 cm^{-1} used for obtaining the black simulation curve in panel b.

α-MoO_3 gives rise to unique polarization rotation capabilities for IR photonics. In order to demonstrate its potential, we have carried out a simple, proof-of-concept experiment as illustrated in Figure 4.10a, on sample S2. In the FTIR experiment, one linear polarizer is placed on the path of incident beam (polarizer) and one in the path of the reflected beam, before the detector (analyzer), similar to Figure 2.2c schematics. These linear polarization angles are defined with respect to $\hat{x}$ axis and are represented with $\phi_i = \phi_p$ and ϕ_a, respectively (Figure 4.10a). The experimental reflectance results for ϕ_i = 45° and different values of ϕ_a is provided in Figure 4.10b.

In Figure 4.10b, when $\phi_i = \phi_a$ = 45°, we observe the reflectance pattern similar to Figure 4.9b ($R = 1 - A$) except that the intensity is lower since a proportion of the power is lost as the reflected beam filters out any polarization other than ϕ_a (Equation 2.18. Keeping ϕ_i = 45° and modifying to ϕ_a = 0° results in decreased reflected intensity, which is expected, again due to filtering of the polarization. The most interesting

scenario unfolds when analyzer is cross-polarized to have 90° phase difference with the incident beam (ϕ_i = 45°, ϕ_a = -45°). If the material were isotropic, the reflected cross-polarized signal would vanish, however, there is reflected intensity that peaks at 727 cm^{-1} as high as 15% from this sample. This infers significant depolarization taking place in the sample and justifies significant polarization rotation associated with the in-plane anisotropy within the lowest frequency RS band. Whilst in principle the addition of a quarter wave plate would allow us to characterize the polarization state of this reflected beam, accurate quarter wave plates are not commercially available covering this spectral range. Therefore, we rely on FDTD and TMM simulations, replicating the experimental configuration, to shed light on the spectral depolarization characteristics of the reflected beam. Sample S2 has been simulated using identical experiment conditions to show that our cavity design supports a range of different polarization states and polarization ellipse rotations, specifically, circularly polarized reflected light from a linearly polarized incident beam. The far-field polarization ellipse characteristics of the structure for reflected beam is extracted and fitted to the ellipse equation, $E_x/E_{0x}^2 + E_y/E_{0y}^2 - 2(E_xE_y/E_{0x}E_{0y})\cos(\delta) = \sin(2\delta)$, where $\delta = \delta_y - \delta_x$ is the phase difference between the phases of electric field vectors in $\hat{y}$ and $\hat{x}$ directions and $2E_{0x}$ and $2E_{0y}$ are the major and minor axes of the polarization ellipse. Circularly polarized reflectance requires the phase difference between E_x and E_y (δ) to be 90° and their amplitude ratio to be 1 to satisfy a circle equation. Figure 4.10c illustrates the logarithmic scale of the ellipticity ($r = E_{0y}/E_{0x}$), i.e., the ratio of major to minor axes of the polarization ellipse (blue curve). In this plot, spikes represent linearly polarized light, where the logarithmic ratio is presented; otherwise, the spikes at linear

polarization points would compromise the legibility of other data points. In particular, this logarithmic plot approaches zero at ω = 727 cm^{-1}, representing almost equal E_{0x} and E_{0y} amplitudes with exact ratio of r = 1.066. The red curve in Figure 4.10c represents the angle of major axis of the polarization ellipse with respect to x axis (ψ). The step near ω = 730 cm^{-1} for this curve has a significant implication; the polarization ellipse and hence field amplitudes extend for both axes, until near 727 cm^{-1}, the major axis is abruptly changed from values close to 45° to the ones near -45°. During this transition, there exists a frequency at which major and minor axes are equal in amplitude and the phase difference between E_x and E_y approaches 90°. This happens at 727 cm^{-1} where $\delta_y - \delta_x$ = -89.16°. Thus, at ω = 727 cm^{-1}, α-MoO_3 changes the linearly polarized incident light to a circularly polarized reflected beam, the polarization ellipse of which is illustrated in Figure 4.10d, representing left-handed circularly polarized light. In order to draw a connection between simulation and experiment we record the spectral ratio of the total electric field in ϕ_a = -45° direction (dashed red line in Figure 4.10d) to the electric field of the incident intensity (ϕ_i = 45°, blue dashed line in Figure 4.10d) from the simulations. In other words, the magnitude of the normalized electric field ($|\mathbf{E}|$) is recorded in the intersection of reflected polarization ellipse with analyzer ϕ_a = -45° at several frequency points (purple dot in Figure 4.10d is an example at ω = 727 cm^{-1}). Afterwards, the normalized field value is squared to represent intensity and is multiplied to the spectral reflectance curve measured for sample S2 in Figure 4.9b when ϕ_i = 45° ($R = 1 - A$, where A is the dark green curve in Figure 4.9b for ϕ_i = 45°). The result is the black curve in Figure 4.10b which follows the peak trend of the experimental pink curve. Figure 5b shows that 15% of the incident

beam is converted to cross-polarized state. Hence, linearly polarized incident light is modified to circularly polarized reflected light at ω = 727 cm^{-1} from measurements, exhibiting quarter-wave plate action at IR frequencies.

Quarter-wave plate frequency can be tuned by adjusting the thickness of layers in this FP structure. With the aim of obtaining circularly polarized radiation in the reflected beam, the spectal polarization ellipse major axis angle (ψ) versus Ge thicness (t_{Ge}) and α-MoO_3 thickness (t_{MO}) are provided, respectively in Figure 4.11a and c. The transformation of ψ between positive and negative values marks a transformation that can support quarter-wave plate action. The transitions lay between the blue and red regions in Figure 4.11a and c. A quality factor can be defined to track the behavior of circular polarization as follows,

$$Q_{circ} = \ln\left(\frac{1}{|\pi/2 - |\delta|| + |1 - |r||}\right). \tag{4.3}$$

Equation 4.3 takes the two conditions of cicular polarization into account such that Q_{circ} becomes very large when the phase difference between E_y and E_x is 90° (δ = $\pi/2$) and the magnitude ratio of the two mentioned orthogonal fields is 1 (r=1). The logarithmic scale is used to improve the clarity of the resulting acceptable data points. In order to single out the most reliabl conversions, δ and r are only allowed to deviate from the ideal circularly polarized case by an error margin of 5%. The results for sweeping t_{Ge} and t_{MO} are, respectively, demonstrated in Figure 4.11b and d, which are in agreement with the previously simulated results with FDTD (Appendic C). As observed earlier, the lines in Figure 4.11b and d are all located within the borders of

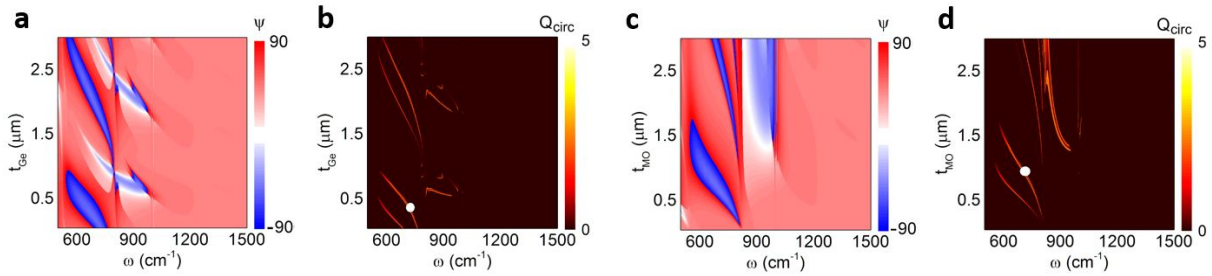

Figure 4.11. Quarter-wave plate using α-MoO_3 FP structure. (a) Spectral polarization ellipse major axis angle (ϕ) versus Ge thickness (t_{Ge}) and (b) spectral quarter-wave plate action quality factor (Q_circ) versus t_{Ge}, with α-MoO_3 thickness t_{MO} = 0.95 μm and incident angle θ = 25° and ϕ_i = 45°. (c) ψ versus t_{MO} and (d) Q_{circ} versus t_{MO}, with t_{Ge} = 0.42 μm and θ = 25° and ϕ_i =45°. The white dots in panels b and d are the experiment data points representing the circularly polarized reflected beam in Figure 4.10d.

the negative and positive ψ transformations in Figure 4.11a and c. We also note that significant depolarization to states other than circular also takes place in this polarization conversion (Appendic C). The mentioned discrepancy is attributed to the rough surface of α-MoO_3 flakes, minimization of which is canonical for efficien polarization conversion applications. In the case of smooth α-MoO_3 flakes, using simulated reflectance curve from sample S2 for ϕ_i = 45° instead of the experimental one, we predict conversion efficiency of over 90% as the ideal limit where all the non-ideal effects are absent. The observed reflectance in experiments, however, suggests a combination of different polarizations that obstructs high efficiency for single polarization in the output. Besides, other polarization rotation and states are also attainable by this configuration. As an example, the ellipticity demonstrates spikes (large r) which represent linearly polarized reflected beam. At ω = 655 cm^{-1}, r = 736, and ψ = -50.4° whic infers that for the reflected beam, linear polarization state of the incident beam is maintained and is rotated by -95.4°.

Pushing quarter-wave plates to a thinner limit. The flake thicknesses required for quarter and half-wave plate actions are more than an order of magnitude smaller than the wavelength of interest. OPhs render the refractive index of α-MoO_3 dispersive. The limit for thinner flakes for polarization conversion action can be pushed further if the frequency of operation is set closer to the OPh resonances. In such a scenario, however, there exists a trade-off between thin flake and loss of power since OPhs absorb light (Figure 4.12). It is worth pointing out that for an α-MoO_3 layer on Ge substrate (i.e., absence of Au layer), the required α-MoO_3 thickness values are approximately two times higher compared to the FP structure proposed in this study. In addition, due to the existence of transmittance in the absence of Au layer, it is more challenging to satisfy the amplitude condition of half-wave plate action which sets more limitations on the accessible frequency and thickness values for circularly polarized radiation. The reflected power in the absence of Au layer is at least 15% less which demonstrates the significance of FP structure for higher efficiency, thinner requirement for samples and the availability of more thickness parameters for tuning (t_{MO} and t_{Ge} in contrast to only t_{MO} for the structure in the absence of Au). The polarization characteristics can also be tuned with the incident polarization angle.

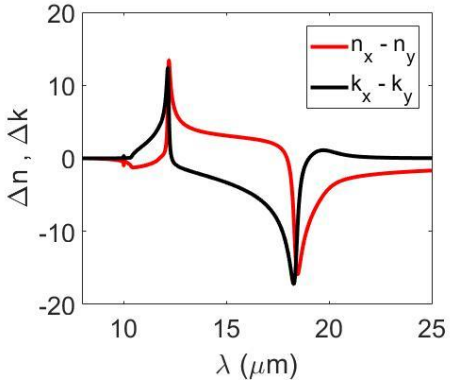

Figure 4.12. Spectral birefringence and dichroism of α-MoO_3 in IR
.

CHAPTER 5

IR Polarization-dependency of MOCVD-grown Ga_2O_3 Thin Films

This chapter is mostly adapted from the following a submitted article.

5.1. Chapter 5 highlights

The phonon modes of materials contain critical information on the quality of the crystals. Phonon modes also offer a wide range of polarization-dependent resonances in infrared that can be tailored to applications that require large dielectric function contrast in different crystal directions. Here, we investigate the far-field characteristics of MOCVD-grown Ga_2O_3 thin films. With a combination of cross-polarization FTIR and AFM characterization techniques, we propose an easy and non-invasive route to distinguish $\alpha$and βphases of Ga_2O_3 and study the quality of these crystals. Using numerical methods and cross-polarization spectroscopy, the depolarization characteristics of β-Ga_2O_3 is examined and depolarization strength values as high as 0.95 and 3.3 are measured respectively for 400 and 800 nm-thick β-Ga_2O_3. The strong birefringence near optical phonon modes of an 800 nm β-Ga_2O_3 on sapphire substrate is used to obtain several polarization states for the reflected light in the second atmospheric window 8-14 µm. We anticipate that our findings open a new path for material characterization and wave plate design for mid-IR range and offer novel possibilities for the future of IR on-chip photonics thanks to the compatibility of β-Ga_2O_3 with standard nanofabrication technology.

5.2. Motivation

Crystal symmetry dictates the optical, electrical, mechanical, and thermal properties of a material. While high-symmetry crystals have been applied to several photonic applications. The low symmetry crystals have opened new possibilities for polarization control, leading to groundbreaking achievements such as display [8] and spectroscopy [5] technologies. Over the recent decade, reduced symmetry has been introduced to high-symmetry crystals using metamaterials to access and modify polarization at arbitrary wavelength ranges [134, 135, 136]. Using patterned periodic unit cells that are much smaller than the wavelength of interest, hence satisfying effective medium theory [55, 137, 138], several applications such as polarization converters [134], wave-plates [139, 140], holography [141, 142] and chirality [143, 144] have been investigated. Novel phenomena such as topological physics [145, 146] have also been facilitated with low-symmetry crystals. Metamaterials, however, are prone to fabrication errors and require expensive and low-yield fabrication techniques as discussed previously.

Naturally occurring low-symmetry materials have recently emerged as possible candidates for anisotropic optical applications [54, 105] in IR. Specifically, in-plane anisotropy from orthorhombic [51], monoclinic [101] and triclinic [52] structures has led to near- and far-field polarization-sensitive applications [54, 102, 147] . More recently, shear polaritons have been demonstrated with a β-Ga_2O_3 substrate in IR [148, 149]. Ga_2O_3 has potential applications in UV photodetectors [150, 151, 152], transparent electrodes [153] and high-power transistors [154, 155, 156]. In the past few years, a few works have reported successful growth of $\varkappa$and βphases of Ga_2O_3 using metal organic chemical vapor deposition (MOCVD) techniques [157, 158, 159]. Although the

optical properties of β-Ga_2O_3 is extensively studied for substrates in VIS and IR [160, 161, 162, 163], the MOCVD-grown thin films of ϰ- and β-Ga_2O_3 have not been studied in detail for IR and are only characterized in VIS [164].

Besides UV applications, thin Ga_2O_3 films are promising candidates for the fast-growing IR photonics and can give rise to novel phonon polariton and polarizing devices and can provoke intriguing topological photonics studies [54, 149]. Since IR hosts lattice phonon modes, investigating materials in IR are also critical for understanding the crystal structures by identifying their unique phonon modes and shed light on the quality of these crystals. Hence, in this chapter, we shed light on the IR optical characteristics of this material, specifically in the second atmospheric window 8-14 μm, based on dispersion due to the optical phonons of Ga_2O_3. We shed light on the differences of optical response of ϰ-Ga_2O_3 and β-Ga_2O_3 and study the depolarization characteristics of reflected light from them. We also report on the differences of MOCVD-grown thin films of ϰ-Ga_2O_3 and β-Ga_2O_3 compared to the existing commercial β-Ga_2O_3 substrates. This study concludes by characterizing the polarization strength of the MOCVD-grown thin films of β-Ga_2O_3 for IR polarization-dependent optics.

5.3. Experiment and simulation

5.3.1. Fabrication

ϰ-Ga_2O_3 (also referred to as ε-Ga_2O_3) has a hexagonal lattice which consists of twin orthorhombic domains rotated by 120° [160, 153]. For this study, β-Ga_2O_3 is fabricated by in-situ thermal annealing of MOCVD-grown ϰ-Ga_2O_3 on sapphire substrate (Figure 5.1a) and has a monoclinic crystal symmetry, hence, demonstrates in-plane anisotropy.

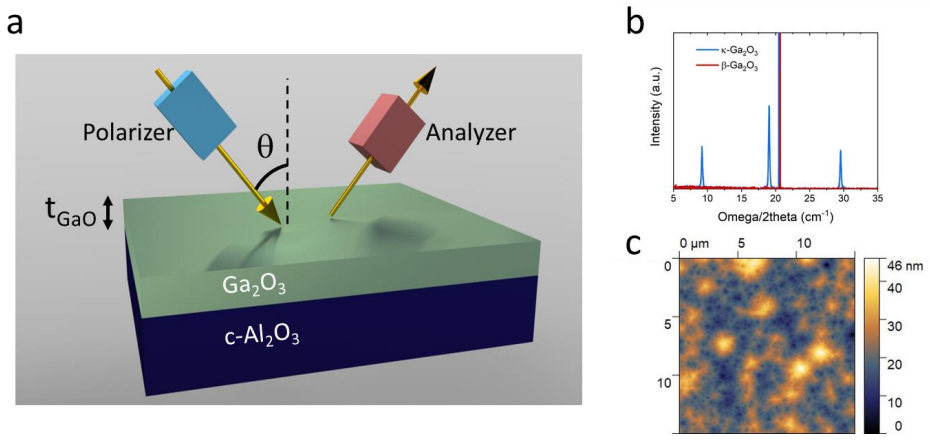

Figure 5.1. (a) schematic representation of samples and the measurement scheme. (b) XRD characterization of $\varkappa$-Ga_2O_3 and β-Ga_2O_3 grown on sapphire substrate. (c) AFM surface roughness map of a 15 µm $\times$ 15 µm area on a 400 nm $\varkappa$-Ga_2O_3.

The samples under study in this work are Ga_2O_3 films grown on c-plane sapphire (c-Al_2O_3) substrates and are studied using polarizers and analyzers as illustrated in Figure 5.1a and in Figure 2.2c.

Ga_2O_3 fabrication. Epitaxial growth of Ga_2O_3 was conducted on c-plane sapphire using an AIX200/4 reactor. The growth temperature was fixed at 690 °C, and the pressure during the growth was 50 mbar and H_2 was used as the carrier gas. Pure H_2O and Trimethyl-Ga (TMGa) were used as O and Ga precursors, respectively, while Silane gas (SiH_4) was utilized as a dopant. Regarding in situ annealing, $\varkappa$-Ga_2O_3 thin films went through annealing process shortly after the growth without exposure to the ambient air. In situ annealing under N_2 condition is preferable to do precise control

of the heating and cooling time, which helps to prevent Ga_2O_3 films from generating undesirable results such as detrimental cracks, usually caused by rapid temperature changes.

5.3.2. Characterization

FTIR normal incidence measurements. The normal incidence measurements are carried out using a Hyperion 2000 IR microscope coupled to a Bruker Vertex 70 FTIR spectrum. MCT detector was used for detection. The Cassegrain objective was 15× and the aperture dimensions were 150×150 μm^2 and the spectra were taken with 22.5° polarization steps. The linear polarizer and analyzer were ZnSe mid-IR polarizers. A total of 128 interferograms were acquired for each measurement, with a spectral resolution of 2 or 3 cm^{-1}.

FTIR high incidence angle measurements. The high incidence angle reflectance spectra have been measured using a last generation FTIR interferometer (Invenio-R, Bruker). The detector is based on deuterated triglycine sulfate (DTGS) photo-voltaic element (spectral range 6000-400 cm^{-1}). A total of 128 interferograms were acquired for each measurement, with a spectral resolution of 2 cm^{-1}. A sample area of 3×3 mm^2 was selected during IR data acquisition using knife edge apertures. Incidence angle was set to 45°. Polarization state of incident light was selected using a KRS-5 holographic wide range IR polarizer with 22.5° polarization steps.

5.3.3. Simulation

The simulations were carried out by 4×4 TMM simulations (Section 2.3) and also a free MATLAB-developed code by Passler et. al. [60].

5.4. Ga_2O_3 crystal characterization with anisotropic optical phonons by cross-polarization spectroscopy

Figure 5.1b represents the XRD characterization of $\varkappa$-Ga_2O_3 and β-Ga_2O_3. Orthorhombic-structured Ga_2O_3 exhibits three different XRD peaks corresponding to (002), (004) and (006) planes of $\varkappa$-phase while new peaks begin to evolve around 19° and 42° when it becomes the monoclinic Ga_2O_3 films, which was achieved through the in-situ annealing process at 1000 °C. Detail information regarding the phase of Ga2O3 can be found in previous works [157, 165]. Figure 5.1c shows an AFM taken on a 15 µm × 15 µm area surface on a 400 nm β-Ga_2O_3 which shows good surface quality and a formation of a smooth Ga_2O_3 film.

Two samples ($\varkappa$-Ga_2O_3 and β-Ga_2O_3) with t_{GaO} = 450 nm are characterized using FTIR with a single linear polarizer (ϕ_p) on the incidence beam path (Figure 5.2a). The z-direction is taken to be the out-of-plane direction and x-direction is defined parallel to the (001) direction of the monoclinic β-Ga_2O_3 crystal. At normal incidence (θ = 0°, shown in the inset of Figure 5.2a) the reflected light off the $\varkappa$-Ga_2O_3 sample (Figure 5.2a) for co- and cross-polarized analyzer (respectively ϕ_a = 45° and ϕ_a = -45°) shows broadened dips between 650 cm^{-1} to 900 cm^{-1}. Within this range, the underlying c-plane sapphire essentially acts as a mirror due to its Reststrahlen (RS) band, and has

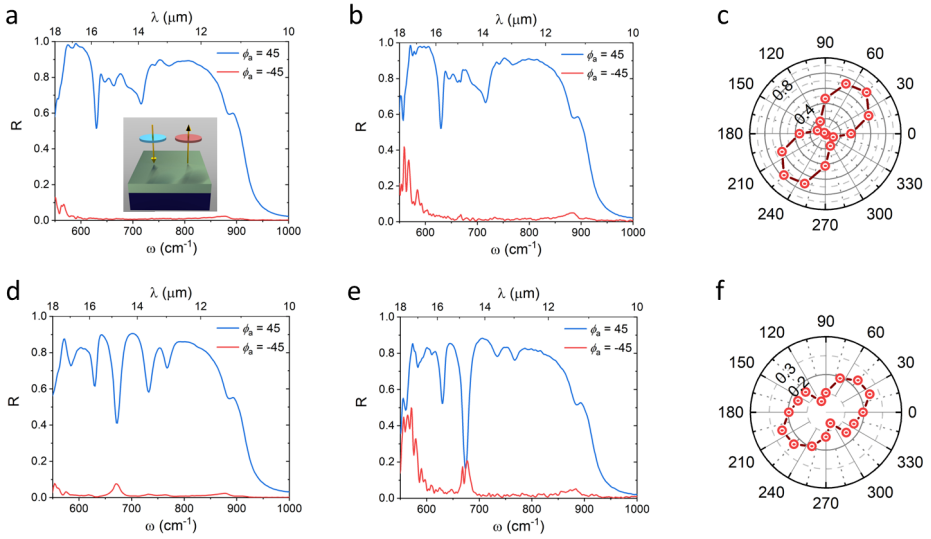

Figure 5.2. Spectral co- and cross-polarization (respectively, ϕ_a = 45° and ϕ_a = -45°) reflectance at polarizer value of ϕ_p = 45° for 450 nm $\varkappa$-Ga_2O_3 on sapphire with (a) open and (b) 100 μm × 100 μm knife aperture. Spectral co- and cross-polarization reflectance at ϕ_p = 45° for 450 nm β-Ga_2O_3 on sapphire with (d) open and (e) 100 μm × 100 μm slit. Polar plot of the reflected light with ϕ_p = 45° versus ϕ_a for (c) $\varkappa$-Ga_2O_3 and (f) β-Ga_2O_3 at 677 cm^{-1}. The inset of (a) illustrates the measurement configuration.

two optical phonon modes, with one optical phonon dip in z-direction at 885 cm^{-1} and an in-plane optical phonon dip at 630 cm^{-1}.

In Figure 5.2a, the broadened dip at 715 cm^{-1} is due to several merged optical phonon modes and is a signature of $\varkappa$-Ga_2O_3 and shows no polarization dependence. There is also a weak out-of-plane optical phonon mode at 774 cm^{-1}. The cross-polarized reflectance for $\varkappa$-Ga_2O_3 is flat and there is no indication of in-plane optical anisotropy. The dip at 880 cm^{-1} originates from longitudinal optical phonons ($P_\perp$) of sapphire. $P_\perp$ is excited for z-direction phonons, contrary to transverse optical phonons ($P_\parallel$) that get

excited for in-plane phonons [54]. While $P_{\perp}$ dip should not be observed at a perfect normal incidence, the existence of this signal is attributed to the Cassegrain objective of Hyperion system which renders the incidence angle slightly off-normal (13° for 15× objective) [54].

β-Ga_2O_3 (Figure 5.2d), one the other hand, has three well-defined optical phonon dips. The optical phonon modes at 673 cm^{-1} and 732 cm^{-1} are in-plane phonon modes and the dip at 768 cm^{-1} is the out-of-plane (z) optical phonon mode Contrary to α-Ga_2O_3, the in-plane dip at 673 cm^{-1} and the out-of-plane dip at 768 cm^{-1} for β-Ga_2O_3 sample demonstrate weak polarization dependence and the cross-polarized reflectance does not vanish. The resonance axis of the optical phonons in monoclinic crystal of β-Ga_2O_3 can be characterized with an angle (α) with respect to the x-axis which defines the lattice oscillation direction. x direction is assumed to be parallel to the crystal direction a in monoclinic lattices. The two optical phonon modes of β-Ga_2O_3 at 673 cm^{-1} and 732 cm^{-1} originate from optical phonon oscillations at α = 5° and α = 47.8°, respectively [161]. The optical phonon at 673 cm^{-1} is almost parallel to the x-direction phonons (hence the name P_x) while the optical phonon mode at 732 cm^{-1} is almost equally split between x and y directions (P_{xy}). The optical modes accessible in the frequency range for sapphire and β-Ga_2O_3 are summarized in Table 5.1 [60]. The optical phonon absorption takes place near ω_{LO} and ω_{TO} respectively for out-of-plane (z) and in-plane frequencies and only these resonances are listed in Table 5.1 for clarity. The parameter α is the angle that the phonon mode oscillation direction makes with x axis where x is parallel to the crystal direction a [161].

Table 5.1. Optical phonon modes (P) observed within 550 cm^{-1} to 1000 cm^{-1} in a β-Ga_2O_3 on sapphire sample [161].

Film	Symbol	ω_{TO}(cm^{-1})	ω_{LO}(cm^{-1})	α(°)
β-Ga_2O_3	P_y	572.52		106
	P_x	692.44		5.1
	P_{xy}	743.48		47.8
	P_z		795.7	
c-Al_2O_3	$P_\perp$		625	
	$P_\perp$		900	

MOCVD-grown thin films of κ-Ga_2O_3 and β-Ga_2O_3 are likely to have crystal defects which can be more significant compared to β-Ga_2O_3 substrates [166]. Since the lattice imperfections play a crucial role in phonon spectroscopy, it is important to identify lattice directions and the corresponding anisotropic phonon responses. More recently, Xu et. al. showed that κ-Ga_2O_3 has orthorhombic crystal structure twin boundaries that form 60° angles, and the adjacent domains with similar crystallinity are at most a few hundred nanometers [158]. This is verified by limiting the knife aperture of FTIR to a 100 μm^2 area in reflectance measurements of Figures 5.2b and e for κ-Ga_2O_3 and β-Ga_2O_3, respectively. The limited (Figure 5.2b) and open aperture (Figure 5.2a) results for κ-Ga_2O_3 are almost identical. The only difference is the increased noisy signal toward the low frequency extreme of the measurement range due to lower signal to noise ratio in limited aperture measurements compared to open aperture ones. Contrarily, the limited aperture measurements for β-Ga_2O_3 (Figure 5.2e) show differences compared to open aperture measurements of Figure 5.2d. Specifically, the peak for cross-polarized (red curve) measurement near 680 cm^{-1} (P_x from Table

5.1) in Figure 5.2e is significantly modified. The depolarization strength is defined as the ratio of the cross-polarized reflectance to the co-polarized reflectance $\eta_{depol} = R_{cross-pol}/R_{co-pol}$ and is measured to be η_{depol} (ω = 674 cm^{-1}) = 0.95. The limited aperture measurements from different areas on the sample show different cross-polarized peaks. This points to the possibility of twin boundaries on the surface in that when the aperture is open, more twin boundaries are present with different monoclinic crystal orientations that average out the polarization-dependency of these measurements. The AFM measurements from a 400 nm β-Ga_2O_3 sample shows faint lines which cannot be identified under FTIR and hence, the crystal orientation cannot be clearly determined. The analyzer angle (ϕ_a)-dependent polar plot of reflectance (at ϕ_a = 45°), taken with limited aperture from χ-Ga_2O_3 and β-Ga_2O_3 are respectively provided in Figures 5.2e and f. The result for β-Ga_2O_3 in Figure 5.2f shows depolarization while the result for χ-Ga_2O_3 in Figure 5.2c is identical to the incident linearly polarized light and shows no depolarization.

The fractions of twin boundaries present in a thin film strongly depend on annealing temperature and film thickness, and thicker films intensify such fractions in twin boundaries [167]. To investigate the twin boundaries and their connection to the IR optical response, a thicker β-Ga_2O_3 film (800 nm) is grown on sapphire. The AFM characterization on this sample shows dramatic fractures on the surface (Figures 5.3a and b) which are even evident under microscope. It is clear from Figure 5.3a that several twin boundaries are parallel (similar crystallinity), and each of these groups form angles of 60° angles with one another, in line with previous studies [158].

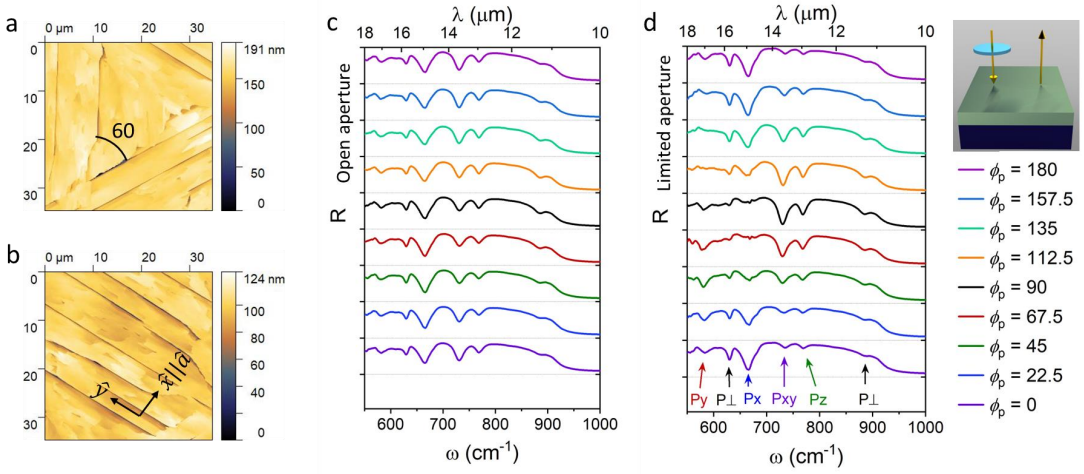

Figure 5.3. (a) and (b) AFM surface image of an 800 nm β-Ga_2O_3 on sapphire. Experimental reflectance measurement of a β-Ga_2O_3 with t_{GaO} = 800 nm on sapphire for various polarizer angles (ϕ_p) and no analyzer, (b) without and (c) with an area limiting knife aperture. The inset on the right illustrates the measurement schematically.

Removing analyzer from the measurements in FTIR (inset of Figure 5.3) can clearly demonstrate polarization-dependence of the optical phonon dips, especially P_x which has only α = 5° to the x-direction. Figures 5.3c and d illustrate reflectance for several linear polarizer angles respectively for open aperture and 100 μm^2 aperture. The polarizer is swept between ϕ_p = 0° and 180° with steps of 22.5°. When the aperture is open (Figure 5.3c), the measured reflectance and all of the dips are polarizer-independent. For higher incidence angles, the dips can be intensified In this case, a combination of different orientations with boundaries forming 60° angles is measured. Therefore, the reflectance is essentially an average of several orientations of β-Ga_2O_3 rotated around

its optical axis and no in-plane anisotropy is observed. When the knife aperture is used (Figures 5.3d), the reflectance shows strong polarization dependency. The dip attributed to P_x (marked on Figures 5.3d) is the strongest at $\phi_p = 0°$ and starts to decay until it vanishes at $\phi_p = 90°$, and it gradually grows back when ϕ_p is increased to $\phi_p = 180°$. The opposite is valid for P_y near 570 cm^{-1}. It is worth pointing out that the x direction in limited aperture measurements is parallel to the short edge of the similar-looking twin boundaries (Figures 5.3b). All the optical phonon modes from Table 5.1 are also identified in Figures 5.3d.

5.5. β-Ga_2O_3 for polarization control in IR

To shed light on the depolarization characteristics of β-Ga_2O_3, we have done measurements with a linear polarizer in the incident light path and a linear polarizer (analyzer) in the path of the reflected light for 800 nm β-Ga_2O_3 as well. The thicker film is chosen to enhance depolarization due to the increased optical path of the incident light through the thicker β-Ga_2O_3 layer. This measurement has been carried out at normal incidence (insets of Figure 5.4d). Figure 5.4a illustrates the co-polarized (blue curve, $\phi_p = 45°$, $\phi_a = 45°$) and cross-polarized (red curve, $\phi_p = 45°$, $\phi_a = -45°$) reflectance measured at normal incidence for the sample with 800 nm β-Ga_2O_3 at limited aperture. The dotted lines are the open aperture counterparts that are analogous to the 400 nm β-Ga_2O_3 measurements (Figure 5.3d) and as expected, do not show significant depolarization. The blue and red curves in Figure 5.4b are the corresponding reflectance simulation results, which are in good agreement with the measured values of Figure 5.4a. All the

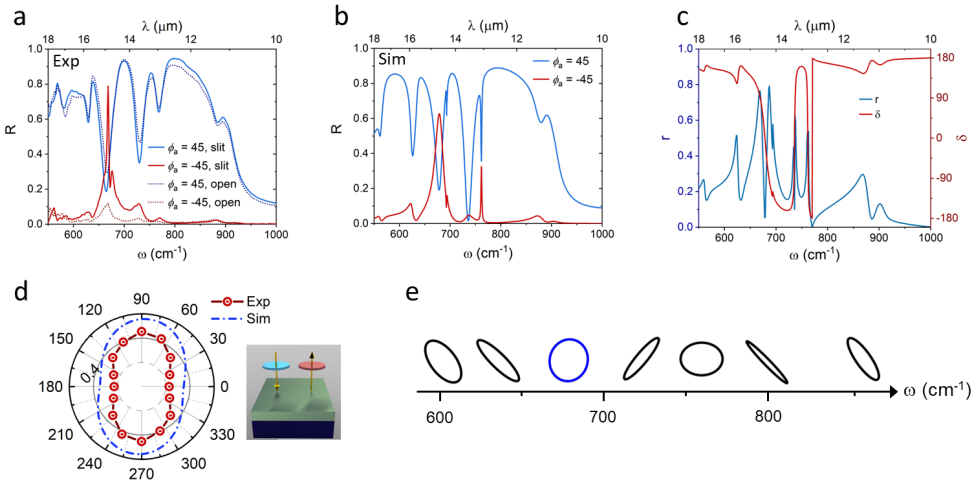

Figure 5.4. (a) Experimental and (b) simulated spectral reflectance of β-Ga_2O_3 with t_{GaO} = 800 nm on sapphire. The polarization is set to ϕ_p = 45° and the analyzer is set to co- and cross-polarized values (ϕ_a = 45° and ϕ_a = -45°). The dotted data in (a) represent the data with no limiting knife aperture. (c) Spectral ellipticity (r) and phase difference (δ). (d) Measured polar plot of the reflected light at 675 cm^{-1} and the simulated polar plot at 688 cm^{-1} as a function of analyzer angle (ϕ_a). (e) Various reflected polarizations attainable with a β-Ga_2O_3 (t_{GaO} = 800 nm) on sapphire. The inset of (d) illustrates the experiment configuration. (e) Polarization ellipses simulated at various ω values. The blue polarization ellipse represents the simulated dashed curve from (d) at 688 cm^{-1}.

previously discussed optical phonon modes in Figures 5.3d and e are also evident in this measurement as well.

The most important takeaway from Figure 5.4a is the cross-polarized reflectance peak observed at 673 cm^{-1} ascribed to P_x of β-Ga_2O_3 which shows the flow of 78% of the reflected power to the cross-polarized reflectance and infers significant depolarization of the reflected light. The depolarization strength is measured to be η_{depol} (ω = 680

cm^{-1}) = 3.2 and the simulated value is η_{depol} (ω = 680 cm^{-1}) = 3.1, at their maximum values. Also evident in cross-polarized reflectance (red solid curve) in Figure 5.4a are two negligible peaks at P_z and P_{xy} of β-Ga_2O_3. The depolarization at 675 cm^{-1} is summarized in Figure 5.4d (red curve) which plots the polar dependence of reflected light on ϕ_a, where the linear polarizer is set to ϕ_p = 45° and the linear analyzer (ϕ_a) is swept from 0° to 360° with steps of 22.5°. The polarization of the incident linearly polarized light (ϕ_p = 45°) is rotated 45°. The electric fields in x and y direction are out of phase since the bowtie does not reach zero at knots. The intensity is dropped due to the absorption of the P_x mode of β-Ga_2O_3. Figure 5.4b shows simulated co- and cross-polarized spectral reflectance curves for 900 nm β-Ga_2O_3 and agrees with the experimental curves in Figure 5.4a. The only difference is that the simulated curve is approximately 10 cm^{-1} off compared to the experimental observations. This discrepancy is ascribed to the slight differences of the MOCVD-grown β-Ga_2O_3 compared to the single-crystal substrate. The dielectric model used here belongs to β-Ga_2O_3 substrate [161, 167]. The simulated polar plot of the reflected light at 688 cm^{-1} (dashed blue line in Figure 5.4d) is shown along with its corresponding experimental one and the two polar plots agree well.

Having modeled the structure with simulations, we can speculate the polarization state of the reflected light building up on our simulations. The blue curve in Figure 5.4c shows the simulated ellipticity (r) defined as the ratio of the electric field amplitudes in x and y directions (E_x and E_y). The phase difference (δ) of is defined ($\delta = \angle E_y - \angle E_x$) which is illustrated as the red curve in Figure 5.4c. These two curves demonstrate that various polarization states are obtainable near optical phonon modes due to the

increased birefringence near these resonance frequencies. A few of the reflected polarization states are summarized in Figure 5.4e and the polarization ellipse corresponding to Figure 5.4d is highlighted in blue, which has ellipticity $r = 0.47$ and phase difference $\delta = -95°$.

CHAPTER 6

Tunable polarization-dependent photonics with α-MoO_3 in IR: Conclusion and future directions in IR photonics

This chapter includes some results adapted from the following published article: Abedini Dereshgi, S., Larciprete, M., Centini, M., Murthy, A.A., Tang, K., Wu, J., Dravid, V.P. and Aydin, K. "Tuning of Optical Phonons in α-MoO_3-VO_2 Multilayers." *ACS Applied Materials & Interfaces*, (2021) [55].

6.1. Chapter 6 highlights

VO_2 is a phase change material that transitions from insulator to metal with applied heat. This material has been applied to several photonic and optical devices to introduce tunability to these systems. Using VO_2 as a sandwiched layer between a α-MoO_3 layer on top and a bottom reflector, gives rise to tunable polarization-dependent photonic devices with α-MoO_3. Despite recent studies on the effect of the phase change of VO_2 on tuning near-field optical response of phonon polaritons in the infrared range, active tuning of optical phonons (OPhs) using far-field techniques has been scarce. Here, we investigate the tunability of OPhs of α-MoO_3 in a multilayer structure with VO_2. Our experiments show the frequency and intensity tuning of 2 cm^{-1} and 11% for OPhs in the [100] direction and 2 cm^{-1} and 28% for OPhs in the [010] crystal direction of α-MoO_3. Using the effective medium theory and dielectric models of each layer, we verify these findings with simulations. This chapter is concluded by

highlighting future routes with preliminary results on tunable polarization response that can modify linearly polarized incident light to both linear and circular states by temperature tuning of VO_2. Our simulations reveal tunability of the response of the proposed multilayer system with heat that can toggle between quarter- and half-wave plate action in infrared These findings can open new avenues in the quest for tunable polarization filters and low-loss, integrated planar IR photonics and in dictating polarization control, as well as camouflage and radiative cooling devices.

6.2. Motivation

Marrying the tunability of VO_2 and the rich optical response of vdW materials through intricate designs, researchers have successfully demonstrated devices with tunable optica responses [168, 169]. In near-field optics the heterostructures of VO_2 with α-MoO_3 and hBN have led to the realization of tunable hyperbolic phonon polaritons in both intensity and frequency through scattering-type scanning near-field optical microscopy characterization [170, 171]. However, reports on the far-field tunability of the optical response of hyperbolic materials with VO_2 do not exist to the best of our knowledge. Here, we experimentally demonstrate that the in-plane hyperbolicity of α-MoO_3 supports polarization-dependent resonant absorption (polarization filter) by optical phonons (OPh) and polarization conversion in the mid-infrared when integrated into a FP cavity. Replacing the cavity spacer with VO_2, we also experimentally demonstrate the tunability of OPhs and cavity modes in α-MoO_3 with the IMT of VO_2 through far-field FTIR measurements in a multilayer structure. Replacing the cavity spacer with VO_2, we also experimentally demonstrate the tunability of OPhs and cavity modes in

α-MoO_3 with the IMT of VO_2 through far-field FTIR measurements in a multilayer structure. We report that the polarization, frequency and intensity of the reflected signal can be actively modulated. We report that by engineering these devices, the polarization, frequency and intensity of the reflected signal can be actively modulated as future directions for on-chip IR photonics.

6.3. Optical model of VO_2

Phase-change materials have proven to be an indispensable tool in the area of optical modulation, offering repeatable and active modulation. Since the first revelation of its dynamic phase-change properties in 1959 [172], the interest in the active modulation properties of VO_2 has been thriving. When the temperature applied to VO_2 increases beyond a critical point (T_c), insulator-to-metal transition (IMT) takes place, which renders its monoclinic (insulator) phase rutile (metallic [173, 174]. While the microscopic dynamics of this intriguing phase transition for VO_2 remains elusive [**r.VOrev**], the experimental implementation of it in devices has been successful in the recent decade. The lower T_c required for the IMT of VO_2 tha that of other phase-change materials [**r.VOrev**, 173], along with a variety of possible routes to achieve IMT (thermally [175], electrically [176], mechanically [177], and optically [178]), has provided ample opportunities to tailor the IMT of VO_2 to numerous applications. The essence of optical modulation in the mentioned photonic applications is the IMT of VO_2, which marks a sizeable change in the refractive index of this material. Some of the notable applications include optical diodes [179], tunable metamaterials [180, 181], thermal emitters [174, 182], and infrared absorbers [183]. Marrying the tunability of VO_2 and the rich optical

response of vdW materials through intricate designs, researchers have successfully demonstrated devices with tunable optical responses.

The IMT process for VO_2 starts with metallic islands that expand as temperature is increased, which can be modeled with the effective medium theory (EMT) where the metallic islands, *i.e.* hot (Hot) phase, are incorporated into a host of insulator, *i.e.* room temperature (RT) phase, of VO_2. The dielectric function of VO_2 changes from RT extreme to Hot extreme as a function of temperature continuously as the metallic islands grow with tempearature. Therefore, using the Hot phase dielectric function of VO_2 as inclusion (ε_i), and its RT phase dielectric function as host (ε_h), the effective dielectric function of VO_2 can be modeled at a given temperature in direction $\hat{j}$ using Equation 2.40 restated here,

$$\varepsilon_{eff,j} = \varepsilon_h + f\frac{\varepsilon_h(\varepsilon_i - \varepsilon_h)}{\varepsilon_h + (1-f)L_j(\varepsilon_i - \varepsilon_h)}. \tag{6.1}$$

The filling ratio (f or FF) is the ratio of metallic islands to the host RT VO_2 which has a correlation to the temperature. The insulator and metal phases of VO_2 are taken from Wan *et al.*. The filling factor (f) is the in-plane filling ratio of the metallic islands to the insulator host within the VO_2 film, which approaches 1 as the temperature is increased. Given the in-plane (transverse) isotropy of VO_2, the EMT yields in-plane and out-of-plane permittivities ($\varepsilon_x = \varepsilon_y \neq \varepsilon_z$). Since the heating is applied in steps of 10 °C with long wait times (slow heating steps), the inclusions are disk-like in shape (Figure 2.4), with the disk axis parallel to the optical axis ($\hat{z}$ direction). This translates to $L_x = L_y \approx 0$ and $L_z \approx 1$ [137].

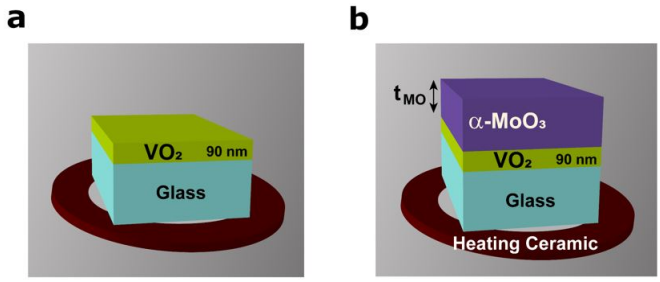

Figure 6.1. Schematic illustration of FP samples under study for tuning of OPhs (a) without and (b) with the α-MoO_3 flake.

6.4. Tuning of Optical Phonons in α-MoO_3-VO_2 FP Multilayers

The structure in Figure 4.6d is modified slightly and Ge is replaced with VO_2 to tune the OPh response of the system using the IMT of VO_2. First, a system without the back reflector is studied. The structure is a multilayer system composed of a 90 nm VO_2 film on a SiO_2 substrate (Figure 6.1a) and an α-MoO_3 flake which is transferred onto VO_2-SiO_2 (Figure 6.1b). The temperature-dependent reflectance measurements are carried out using the FTIR system where the sample is placed onto a heating ceramic, as illustrated in Figure 6.2a,b. The measured spectral reflectance curves for different temperature values are depicted in Figure 6.2a,b as solid curves for samples without (Figure 6.1aa) and with the α-MoO_3 flake (Figure 6.1ab), respectively.

The mentioned dielectric models are employed to TMM method to simulate the reflectance curves for three distinct temperature values, that is, RT, 60 °C, and 90 °C. The simulation results for the sample without the α-MoO_3 layer are depicted in Figure 6.2a, b (dashed curves), which agree well with the experimental results. The polarization is set to $\phi_p = 0$ since only OPh_x is within measurement range. SiO_2 is also modeled using Lorentz oscillator equation. As the temperature is increased,

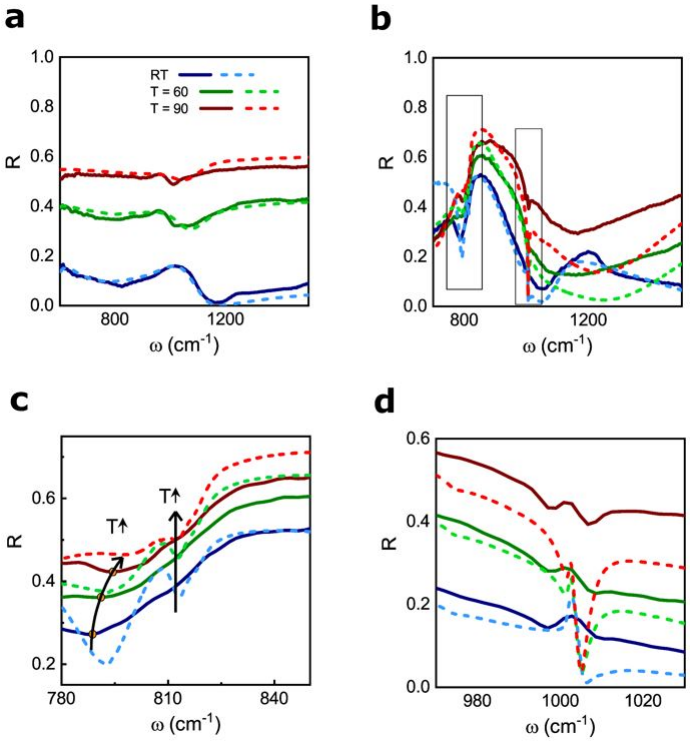

Figure 6.2. Simulated (dashed) and measured (solid) spectral reflectance for the sample (a) without and (b) with the α-MoO_3 flake. Zoomed-in selections from (b) near (c) 800 cm^{-1}1, representing OPh_x and FP modes, and (d) 1000 cm^{-1}, representing OPh_z and SiO_2 substrate phonon modes. The zoomed-in selections are represented by rectangles with black solid lines in (b). The arrows in (c) demonstrate the change of resonances (FP and OPh_x) as the applied temperature is increased.

the IMT takes place, and the reflectance increases due to the metallic nature of VO_2 after the IMT. This dramatic change in spectral reflectance occurs around 70 °C, which corresponds to the VO_2 phase transformation being triggered [184]. From the reflectance curves for the sample with α-MoO_3 (Figure 6.2b), we observe a shift in the reflectance intensity for OPhs in the [100] direction (OPh_x) at 812 cm^{-1} [54]. Also evident from Figure 6.2b is a larger dip in reflectance for the room-temperature (RT) curve at 789

cm^{-1}, which corresponds to the FP mode due to the thick α-MoO_3 layer (air-α-MoO_3-VO_2 stack) which dissipates in the VO_2 layer. This mode blue-shifts (moves to a higher frequency) as the temperature increases due to the modified phase shift imparted on the reflected light off of the α-MoO_3-VO_2 interface. There is a small dip at 1008 cm^{-1}, evident in Figure 6.2b, which is due to the OPhs in the [010] direction of α-MoO_3 (OPh_z). For $\omega < 1000$ cm^{-1}, the reflectance dips are attributed to the OPhs of SiO_2.

Figure 6.2c and d illustrates a close-up view of the FP and OPh_x modes. As temperature rises from RT to 90 °C (Hot), the measured FP mode demonstrates a frequency shift of 4 cm^{-1} from 789 to 794 cm^{-1} and an intensity change of 0.15 from 0.27 to 0.42. The simulated values suggest a similar shift of 7 cm^{-1} in frequency and 0.26 in intensity. The measured OPh_x mode at 812 cm^{-1} demonstrates an intensity shift of 0.11 and a frequency shift of 2 cm^{-1}. Although the simulations show a frequency shift of 0.94 cm^{-1} for the OPh_x mode, such a small shift is too close to the highest resolution of our FTIR system, which is 2 cm^{-1}, which can explain the higher shift observed in measurements. Small frequency shifts are also expected in the literature for thin layers [185]. The OPh_z mode (997 cm^{-1}) in Figure 6.2d demonstrates a frequency shift of 2 cm^{-1} and an intensity shift of 0.28 when the temperature increases from RT to Hot. The simulations suggest a frequency shift of 1.2 cm^{-1}. The highest observed frequency shift is for the FP (or the Etalon) mode trapped inside α-MoO_3 and dissipated to VO_2. The average thickness of the measurement area for the α-MoO_3 layer is 1.27 μm.

To further verify the observed modes and shifts in the original FP structure with back reflector, another sample is fabricated with layers consisting of Pt (100 nm), VO_2 (90 nm), and α-MoO_3 from the bottom to the top, as illustrated in Figure 6.3a. This

structure includes a 220 nm α-MoO_3 layer. Using Pt as a bottom reflector layer isolates the observed reflectance from the effects of glass phonon modes near 997 cm^{-1}. Figure 6.3b demonstrates the simulated spectral reflectance versus FF (which is temperature-dependent) plot that clearly outlines the observed OPh_x and OPh_z modes, respectively, near 810 and 1006 cm^{-1}. Due to the thinner α-MoO_3 layer in this sample, FP modes do not exist. Figure 6.3c, d demonstrates the measured (solid) an simulated (dotted) spectral reflectance at three different temperature values. The experimental OPhx mode (dip) in Figure 6.3c demonstrates a blue shift of 2 cm^{-1} and an intensity shift of 0.1 as temperature is increased to hot from RT (inset o Figure 6.3c). Simulated shifts are 0.53 and 0.08 cm^{-1}. Figure 6.3 demonstrates the measured and simulated spectral reflectance curves for the same sample without α-MoO_3, which agree well. The difference between the simulation and measurement mainly arises for the intensity of the resonances, which is expected due to the sharpness of these resonances and the limiting resolution of FTIR spectra. In this study, the chosen thickness values for α-MoO_3 and VO_2 were not th optimum case and were chosen as the reported values due to the fabrication and transfer challenges that are concomitant to current VO_2 and α-MoO_3 growth techniques. The frequency and intensity tuning can be further enhanced by modifying the thicknesses of the layers.

6.5. *Future work*: Active polarization modulation with VO_2

In a continuation to the frequency and reflectance intensity tuning, we are planning to analyze active polarization tuning in FP system (Figure 6.3a) marrying the phase change characteristics of VO_2 with the birefringence of α-MoO_3. In order to do this, a

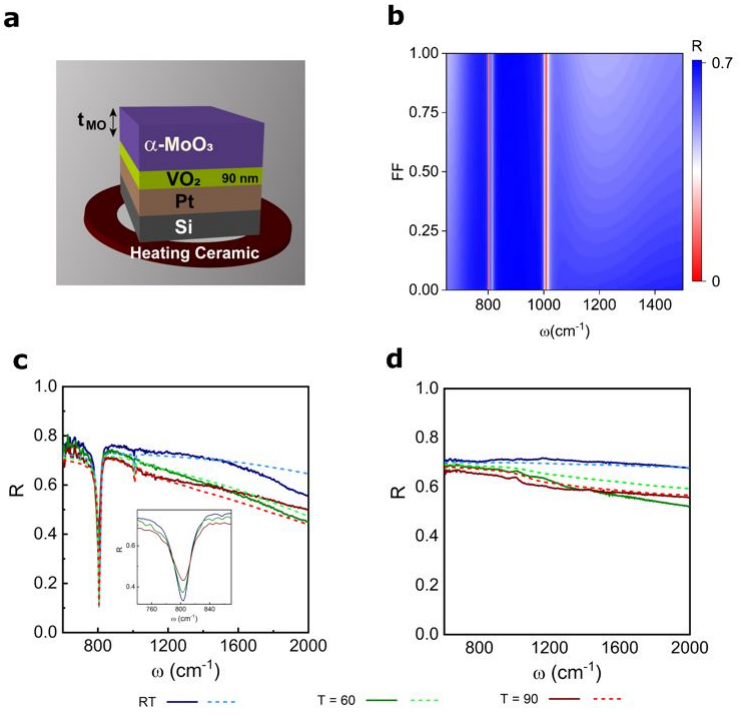

Figure 6.3. (a) Schematic illustration of the sample under investigation and (b) spectral reflectance of this sample vs filling ratio (FF). The simulated (dashed) and measured (solid) spectra reflectance of the sample in (a) for three applied temperature values, (c) with and (d) without the α-MoO_3 flake on the top. The inset of (c) is a close-up view of the measured OPh_x resonance mode.

better control over the thickness of the mentioned layers necessitates. While controlling the thickness of α-MoO_3 can be challenging in its early development stages as it is, a thicker VO_2 can still provide flexibility in the design of active retarding device. To that end, preliminary simulations are put forth here. Considering two extreme cases of polarization, linear and circular, TMM is solved to obtain solutions for such polarization rotation. it is worth mentioning again that changing the temperature dinamically changes the refractive index of VO_2 dynamically, where temperature is linked to dielectric function through the parameter f in Equation 2.40. Therefore, the design variables

are $\phi_i(=\ \phi_p), t_{MO}, t_{VO}, f$ and λ. All these parameters are left as variables to form a library of possible designs to obtain linear to circular polarization transition. For this optimization, ellipticity (r) is chosen as the figure of merit, where $r = 1$ and $r = 0$ respectively represent circular and linear polarizations in reflected beam. In order to pick acceptable solutions, an error margin of 10% is defined meaning $0.9 < r < 1$ and $0 < r, 0.1$ are defined as acceptable ellipticity values for circular and linear polarization, respectively. Figure 6.4a shows all of the data points and Figure 6.4b shows some of the solution points that satisfy the defined conditions for r. Figure 6.4c represents the polarization ellipse of one of the solution points. The parameters for the solution point in Figure 6.4c is summarized in Table 6.1 which indicates that for t_{MO} = 250 nm and t_{VO} = 325 nm, increasing the temperature from f = 0.2 to f = 1 (Hot), the polarization ellipse changes from circular to linear at 12.7 µm, with ellipticity values of r = 0.9318 and r = 0.0047, respectively. Other information such as electric field values and reflectance values (R) are also provided in Table 6.1.

The simulation results demonstrate thermo-optical polarization modulation from circular to linear, among other polarization states in between that are accessible. These findings reveal the possibility to manipulate phase, amplitude and polarization of light in visible, near-infrared and infrared and provides insight into tunable manipulation of the properties of light using emerging vn der Waals materials. We envisage that our findings can open new avenues in the quest for tunable polarization filters and low-loss, integrated planar photonics and in dictating polarization control, as well as camouflage and radiative cooling devices of the next generation.

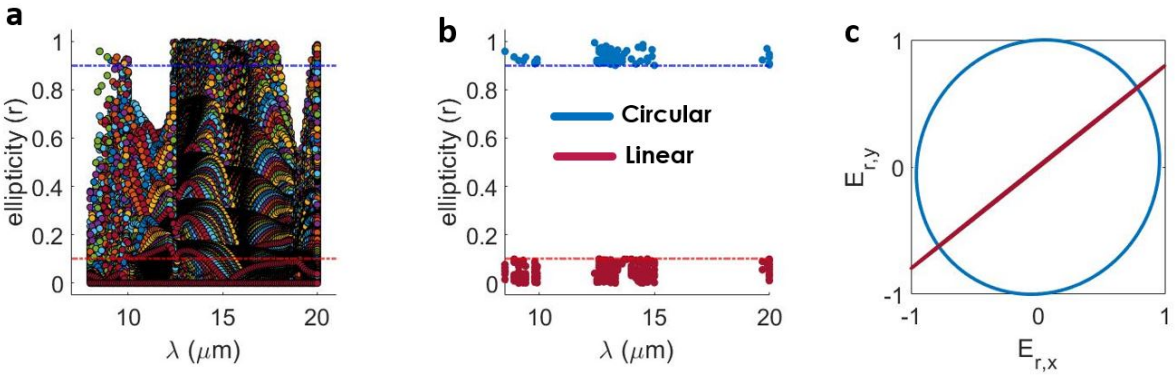

Figure 6.4. Thermo-optical polarization modulation. (a) All of the TMM simulated data points for actively tuning the polarization. (b) Solutions of the TMM which convert the polarization of reflected light from linear to circular or vice versa. (c) Polarization ellipse of one of the solution data points; blue curve is for the lower tempere ($f = 0.2$) circular state and red is for the higher temperature ($f = 1$, i.e. Hot) linear state.

Table 6.1. Solution of TMM parameters for circular to linear polarization conversion of Figure 6.4c in a α-MoO_3-VO_2-Pt structure.

ϕ_p		30	
t_{MO} (nm)		250	
t_{VO} (nm)		325	
λ (μm)		12.7	
Circular		Linear	
f	**0.2**	f	**1**
r	**0.9318**	r	**0.0047**
E_x	0.2	E_x	1
E_y	0.2	E_y	1
R	0.29	R	0.24

Bibliography

[1] Charles Moore McIntyre and SE Harris. "Achromatic wave plates for the visible spectrum". In: *JOSA* 58.12 (1968), pp. 1575–1580.

[2] He Yang et al. "Optical waveplates based on birefringence of anisotropic two-dimensional layered materials". In: *Acs Photonics* 4.12 (2017), pp. 3023–3030.

[3] Bahaa EA Saleh and Malvin Carl Teich. *Fundamentals of photonics*. john Wiley & sons, 2019.

[4] Xiaodong Xun and Robert W Cohn. "Phase calibration of spatially nonuniform spatial light modulators". In: *Applied optics* 43.35 (2004), pp. 6400–6406.

[5] J Badoz et al. "Sensitive devices to determine the state and degree of polarization of a light beam using a birefringence modulator". In: *Journal of Optics* 8.6 (1977), p. 373.

[6] Manuel JLF Rodrigues et al. "Resonantly increased optical frequency conversion in atomically thin black phosphorus". In: *Advanced Materials* 28.48 (2016), pp. 10693–10700.

[7] Mengxin Ren et al. "Giant nonlinear optical activity in a plasmonic metamaterial". In: *Nature communications* 3.1 (2012), pp. 1–6.

[8] Jun Amako and Tomio Sonehara. "Kinoform using an electrically controlled birefringent liquid-crystal spatial light modulator". In: *Applied Optics* 30.32 (1991), pp. 4622–4628.

[9] Johannes F De Boer et al. “Two-dimensional birefringence imaging in biological tissue by polarization-sensitive optical coherence tomography”. In: *Optics letters* 22.12 (1997), pp. 934–936.

[10] Gorachand Ghosh. “Dispersion-equation coefficients for the refractive index and birefringence of calcite and quartz crystals”. In: *Optics communications* 163.1-3 (1999), pp. 95–102.

[11] Jiaming Hao et al. “Manipulating electromagnetic wave polarizations by anisotropic metamaterials”. In: *Physical review letters* 99.6 (2007), p. 063908.

[12] Alexander N Grigorenko, Marco Polini, and KS Novoselov. “Graphene plasmonics”. In: *Nature photonics* 6.11 (2012), pp. 749–758.

[13] Tony Low et al. “Polaritons in layered two-dimensional materials”. In: *Nature materials* 16.2 (2017), pp. 182–194.

[14] JB Young, HA Graham, and EW Peterson. “Wire grid infrared polarizer”. In: *Applied Optics* 4.8 (1965), pp. 1023–1026.

[15] Chinhua Wang and Haowen Lu. “Ultra-broadband linear polarizer based on subwavelength nanocavity structure in infrared region”. In: *First Optics Frontier Conference*. Vol. 11850. SPIE. 2021, pp. 22–29.

[16] Itsunari Yamada et al. “Mid-infrared wire-grid polarizer with silicides”. In: *Optics letters* 33.3 (2008), pp. 258–260.

[17] Md Didarul Islam et al. “Design of High Efficient Mid-Wavelength Infrared Polarizer on ORMOCHALC Polymer”. In: *Macromolecular Materials and Engineering* 305.5 (2020), p. 2000033.

[18] Thomas G Folland and Joshua D Caldwell. *Precise control of infrared polarization using crystal vibrations*. 2018.

[19] A Fratalocchi, C Conti, and G Ruocco. "Three-dimensional ab initio investigation of light-matter interaction in Mie lasers". In: *Physical Review A* 78.1 (2008), p. 013806.

[20] Xiang Zhang et al. *Plasmon lasers at deep subwavelength scale*. US Patent 8,509,276. 2013.

[21] Mohammadreza Khorasaninejad et al. "Metalenses at visible wavelengths: Diffraction-limited focusing and subwavelength resolution imaging". In: *Science* 352.6290 (2016), pp. 1190–1194.

[22] Yeong Hwan Ko et al. "Perfectly-reflecting guided-mode-resonant photonic lattices possessing Mie modal memory". In: *Optics express* 29.17 (2021), pp. 26971–26982.

[23] Katie E Chong et al. "Polarization-independent silicon metadevices for efficient optical wavefront control". In: *Nano letters* 15.8 (2015), pp. 5369–5374.

[24] Wisnu Hadibrata et al. "Inverse design and 3D printing of a metalens on an optical fiber tip for direct laser lithography". In: *Nano letters* 21.6 (2021), pp. 2422–2428.

[25] Hasan Kocer et al. "Nano shell impact on Huygens' metasurface dipolar resonances and optical response". In: *JOSA B* 38.9 (2021), pp. C127–C135.

[26] Koray Aydin et al. "Broadband polarization-independent resonant light absorption using ultrathin plasmonic super absorbers". In: *Nature communications* 2.1 (2011), pp. 1–7.

[27] Xianglian Song et al. “Enhanced Interaction of Optical Phonons in h-BN with Plasmonic Lattice and Cavity Modes”. In: *ACS Applied Materials & Interfaces* (2021).

[28] Nasrin Razmjooei et al. “Resonant reflection by microsphere arrays with AR-quenched Mie scattering”. In: *Optics express* 29.12 (2021), pp. 19183–19192.

[29] Ataollah Kalantari Osgouei et al. “Active tuning from narrowband to broadband absorbers using a sub-wavelength VO2 embedded layer”. In: *Plasmonics* 16.4 (2021), pp. 1013–1021.

[30] Mark L Brongersma, Naomi J Halas, and Peter Nordlander. “Plasmon-induced hot carrier science and technology”. In: *Nature nanotechnology* 10.1 (2015), pp. 25–34.

[31] Ataollah Kalantari Osgouei et al. “Visible light metasurface for adaptive photodetection”. In: *Journal of Physics D: Applied Physics* 55.47 (2022), p. 475103.

[32] Bing Shen et al. “Ultra-high-efficiency metamaterial polarizer”. In: *Optica* 1.5 (2014), pp. 356–360.

[33] Pin Chieh Wu et al. “Near-Infrared Active Metasurface for Dynamic Polarization Conversion”. In: *Advanced Optical Materials* 9.16 (2021), p. 2100230.

[34] Stefan A Maier and Harry A Atwater. “Plasmonics: Localization and guiding of electromagnetic energy in metal/dielectric structures”. In: *Journal of applied physics* 98.1 (2005), p. 10.

[35] Zubin Jacob. “Hyperbolic phonon–polaritons”. In: *Nature materials* 13.12 (2014), pp. 1081–1083.

[36] Diego Correas-Serrano, Andrea Alù, and J Sebastian Gomez-Diaz. "Plasmon canalization and tunneling over anisotropic metasurfaces". In: *Physical Review B* 96.7 (2017), p. 075436.

[37] S Dai et al. "Subdiffractional focusing and guiding of polaritonic rays in a natural hyperbolic material". In: *Nature communications* 6.1 (2015), pp. 1–7.

[38] Alexander Poddubny et al. "Hyperbolic metamaterials". In: *Nature photonics* 7.12 (2013), pp. 948–957.

[39] Peining Li et al. "Hyperbolic phonon-polaritons in boron nitride for near-field optical imaging and focusing". In: *Nature communications* 6.1 (2015), pp. 1–9.

[40] Xiao Lin et al. "All-angle negative refraction of highly squeezed plasmon and phonon polaritons in graphene–boron nitride heterostructures". In: *Proceedings of the National Academy of Sciences* 114.26 (2017), pp. 6717–6721.

[41] Jacob B Khurgin. "How to deal with the loss in plasmonics and metamaterials". In: *Nature nanotechnology* 10.1 (2015), pp. 2–6.

[42] Charlotte I Evans et al. "Quantifying remote heating from propagating surface plasmon polaritons". In: *Nano letters* 17.9 (2017), pp. 5646–5652.

[43] Joseph B Herzog, Mark W Knight, and Douglas Natelson. "Thermoplasmonics: quantifying plasmonic heating in single nanowires". In: *Nano letters* 14.2 (2014), pp. 499–503.

[44] Mahmood Aliofkhazraei. *Handbook of nanoparticles*. Springer, 2016.

[45] Urcan Guler, Vladimir M Shalaev, and Alexandra Boltasseva. "Nanoparticle plasmonics: going practical with transition metal nitrides". In: *Materials Today* 18.4 (2015), pp. 227–237.

[46] Sergey Kruk and Yuri Kivshar. "Functional meta-optics and nanophotonics governed by Mie resonances". In: *Acs Photonics* 4.11 (2017), pp. 2638–2649.

[47] Alexander N Grigorenko, Marco Polini, and KS Novoselov. "Graphene plasmonics". In: *Nature photonics* 6.11 (2012), pp. 749–758.

[48] Fengnian Xia, Han Wang, and Yichen Jia. "Rediscovering black phosphorus as an anisotropic layered material for optoelectronics and electronics". In: *Nature communications* 5.1 (2014), pp. 1–6.

[49] Nannan Mao et al. "Optical anisotropy of black phosphorus in the visible regime". In: *Journal of the American Chemical Society* 138.1 (2016), pp. 300–305.

[50] He Yang et al. "Optical waveplates based on birefringence of anisotropic two-dimensional layered materials". In: *Acs Photonics* 4.12 (2017), pp. 3023–3030.

[51] Shuli Zhao et al. "Controlled synthesis of single-crystal SnSe nanoplates". In: *Nano research* 8.1 (2015), pp. 288–295.

[52] Daniel Wolverson et al. "Raman spectra of monolayer, few-layer, and bulk ReSe2: an anisotropic layered semiconductor". In: *ACS nano* 8.11 (2014), pp. 11154–11164.

[53] Sina Abedini Dereshgi, Zizhuo Liu, and Koray Aydin. "Anisotropic localized surface plasmons in borophene". In: *Optics express* 28.11 (2020), pp. 16725–16739.

[54] Sina Abedini Dereshgi et al. "Lithography-free IR polarization converters via orthogonal in-plane phonons in α-MoO 3 flakes". In: *Nature communications* 11.1 (2020), pp. 1–9.

[55] Sina Abedini Dereshgi et al. "Tuning of Optical Phonons in α-MoO3–VO2 Multilayers". In: *ACS Applied Materials & Interfaces* (2021).

[56] Chenwei Wei et al. “Polarization Reflector/Color Filter at Visible Frequencies via Anisotropic α-MoO3”. In: *Advanced Optical Materials* 8.11 (2020), p. 2000088.

[57] S Dai et al. “Graphene on hexagonal boron nitride as a tunable hyperbolic metamaterial”. In: *Nature nanotechnology* 10.8 (2015), pp. 682–686.

[58] Constantine A Balanis. *Advanced engineering electromagnetics*. John Wiley & Sons, 1999.

[59] I Abdulhalim. “Analytic propagation matrix method for linear optics of arbitrary biaxial layered media”. In: *Journal of Optics A: Pure and Applied Optics* 1.5 (1999), p. 646.

[60] Nikolai Christian Passler and Alexander Paarmann. “Generalized $4\times$ 4 matrix formalism for light propagation in anisotropic stratified media: study of surface phonon polaritons in polar dielectric heterostructures”. In: *JOSA B* 34.10 (2017), pp. 2128–2139.

[61] Vadim A Markel. “Introduction to the Maxwell Garnett approximation: tutorial”. In: *JOSA A* 33.7 (2016), pp. 1244–1256.

[62] Ari Sihvola. “Metamaterials and depolarization factors”. In: *Progress In Electromagnetics Research* 51 (2005), pp. 65–82.

[63] Hiroshi Kakiuchida et al. “Optical properties of vanadium dioxide film during semiconductive–metallic phase transition”. In: *Japanese Journal of Applied Physics* 46.2L (2007), p. L113.

[64] Joshua A Mason et al. “Strong coupling of molecular and mid-infrared perfect absorber resonances”. In: *IEEE Photonics Technology Letters* 24.1 (2011), pp. 31–33.

[65] Shaunak Mukherjee et al. “Fanoshells: nanoparticles with built-in Fano resonances”. In: *Nano letters* 10.7 (2010), pp. 2694–2701.

[66] Huiqin Zhang et al. “Hybrid exciton-plasmon-polaritons in van der Waals semiconductor gratings”. In: *Nature communications* 11.1 (2020), pp. 1–9.

[67] Xiaohua Wu, Stephen K Gray, and Matthew Pelton. “Quantum-dot-induced transparency in a nanoscale plasmonic resonator”. In: *Optics express* 18.23 (2010), pp. 23633–23645.

[68] Rovena Pascu and Maria Dinescu. “Spectroscopic ellipsometry”. In: *Romanian Reports in Physics* 64.1 (2012), pp. 135–142.

[69] Andrei Nemilentsau, Tony Low, and George Hanson. “Anisotropic 2D materials for tunable hyperbolic plasmonics”. In: *Physical review letters* 116.6 (2016), p. 066804.

[70] Zizhuo Liu and Koray Aydin. “Localized surface plasmons in nanostructured monolayer black phosphorus”. In: *Nano letters* 16.6 (2016), pp. 3457–3462.

[71] Joshua D Caldwell et al. “Sub-diffractional volume-confined polaritons in the natural hyperbolic material hexagonal boron nitride”. In: *Nature communications* 5.1 (2014), pp. 1–9.

[72] Xiao Lin et al. “All-angle negative refraction of highly squeezed plasmon and phonon polaritons in graphene–boron nitride heterostructures”. In: *Proceedings of the National Academy of Sciences* 114.26 (2017), pp. 6717–6721.

[73] Ekmel Ozbay. “Plasmonics: merging photonics and electronics at nanoscale dimensions”. In: *science* 311.5758 (2006), pp. 189–193.

[74] Jon A Schuller et al. “Plasmonics for extreme light concentration and manipulation”. In: *Nature materials* 9.3 (2010), pp. 193–204.

[75] Amir Ghobadi et al. “Visible light nearly perfect absorber: an optimum unit cell arrangement for near absolute polarization insensitivity”. In: *Optics express* 25.22 (2017), pp. 27624–27634.

[76] Sina Abedini Dereshgi et al. “Plasmonically enhanced metal–insulator multistacked photodetectors with separate absorption and collection junctions for near-infrared applications”. In: *Scientific reports* 7.1 (2017), pp. 1–8.

[77] Philipp Reineck et al. “A solid-state plasmonic solar cell via metal nanoparticle self-assembly”. In: *Advanced Materials* 24.35 (2012), pp. 4750–4755.

[78] Luc Duempelmann et al. “Four-fold color filter based on plasmonic phase retarder”. In: *ACS Photonics* 3.2 (2016), pp. 190–196.

[79] Rupert F Oulton et al. “A hybrid plasmonic waveguide for subwavelength confinement and long-range propagation”. In: *nature photonics* 2.8 (2008), pp. 496–500.

[80] Nanfang Yu and Federico Capasso. “Flat optics with designer metasurfaces”. In: *Nature materials* 13.2 (2014), pp. 139–150.

[81] Brian Edwards et al. “Experimental verification of plasmonic cloaking at microwave frequencies with metamaterials”. In: *Physical review letters* 103.15 (2009), p. 153901.

[82] Jianing Chen et al. “Optical nano-imaging of gate-tunable graphene plasmons”. In: *Nature* 487.7405 (2012), pp. 77–81.

[83] Baojie Feng et al. “Direct evidence of metallic bands in a monolayer boron sheet”. In: *Physical Review B* 94.4 (2016), p. 041408.

[84] Yuefei Huang, Sharmila N Shirodkar, and Boris I Yakobson. “Two-dimensional boron polymorphs for visible range plasmonics: a first-principles exploration”. In: *Journal of the American Chemical Society* 139.47 (2017), pp. 17181–17185.

[85] Andrew J Mannix et al. “Synthesis of borophenes: Anisotropic, two-dimensional boron polymorphs”. In: *Science* 350.6267 (2015), pp. 1513–1516.

[86] Baojie Feng et al. “Experimental realization of two-dimensional boron sheets”. In: *Nature chemistry* 8.6 (2016), pp. 563–568.

[87] Chao Lian et al. “Integrated plasmonics: Broadband dirac plasmons in borophene”. In: *Physical Review Letters* 125.11 (2020), p. 116802.

[88] Baojie Feng et al. “Dirac fermions in borophene”. In: *Physical review letters* 118.9 (2017), p. 096401.

[89] D Correas-Serrano et al. “Black phosphorus plasmonics: anisotropic elliptical propagation and nonlocality-induced canalization”. In: *Journal of Optics* 18.10 (2016), p. 104006.

[90] Brian Kiraly et al. “Borophene synthesis on Au (111)”. In: *ACS nano* 13.4 (2019), pp. 3816–3822.

[91] Andrew J Mannix et al. “Synthesis of borophenes: Anisotropic, two-dimensional boron polymorphs”. In: *Science* 350.6267 (2015), pp. 1513–1516.

[92] Andrew J Mannix et al. “Borophene as a prototype for synthetic 2D materials development”. In: *Nature nanotechnology* 13.6 (2018), pp. 444–450.

[93] Pranay Ranjan et al. “Freestanding borophene and its hybrids”. In: *Advanced Materials* 31.27 (2019), p. 1900353.

[94] A Yu Nikitin, Tony Low, and Luis Martin-Moreno. “Anomalous reflection phase of graphene plasmons and its influence on resonators”. In: *Physical Review B* 90.4 (2014), p. 041407.

[95] Michelle C Sherrott et al. "Anisotropic quantum well electro-optics in few-layer black phosphorus". In: *Nano letters* 19.1 (2018), pp. 269–276.

[96] OV Kotov and Yu E Lozovik. "Enhanced optical activity in hyperbolic metasurfaces". In: *Physical Review B* 96.23 (2017), p. 235403.

[97] JS Gomez-Diaz, M Tymchenko, and A Alù. "Hyperbolic metasurfaces: surface plasmons, light-matter interactions, and physical implementation using graphene strips". In: *Optical Materials Express* 5.10 (2015), pp. 2313–2329.

[98] Kaveh Khaliji et al. "Tunable plasmon-enhanced birefringence in ribbon array of anisotropic two-dimensional materials". In: *Physical Review B* 95.20 (2017), p. 201401.

[99] JS Gomez-Diaz and Andrea Alu. "Flatland optics with hyperbolic metasurfaces". In: *ACS Photonics* 3.12 (2016), pp. 2211–2224.

[100] Saman Jahani and Zubin Jacob. "All-dielectric metamaterials". In: *Nature nanotechnology* 11.1 (2016), pp. 23–36.

[101] Fucai Liu et al. "High-sensitivity photodetectors based on multilayer GaTe flakes". In: *ACS nano* 8.1 (2014), pp. 752–760.

[102] Souvik Biswas et al. "Broadband electro-optic polarization conversion with atomically thin black phosphorus". In: *Science* 374.6566 (2021), pp. 448–453.

[103] Yohannes Abate et al. "Recent progress on stability and passivation of black phosphorus". In: *Advanced Materials* 30.29 (2018), p. 1704749.

[104] M Dhanasankar, KK Purushothaman, and G Muralidharan. "Optical, structural and electrochromic studies of molybdenum oxide thin films with nanorod structure". In: *Solid state sciences* 12.2 (2010), pp. 246–251.

[105] Weiliang Ma et al. “In-plane anisotropic and ultra-low-loss polaritons in a natural van der Waals crystal”. In: *Nature* 562.7728 (2018), pp. 557–562.

[106] Luc Lajaunie et al. “Strong anisotropic influence of local-field effects on the dielectric response of α-MoO 3”. In: *Physical Review B* 88.11 (2013), p. 115141.

[107] M Dhanasankar, KK Purushothaman, and G Muralidharan. “Optical, structural and electrochromic studies of molybdenum oxide thin films with nanorod structure”. In: *Solid state sciences* 12.2 (2010), pp. 246–251.

[108] Arijit Saha, Kallol Bhattacharya, and Ajoy Kumar Chakraborty. “Achromatic quarter-wave plate using crystalline quartz”. In: *Applied optics* 51.12 (2012), pp. 1976–1980.

[109] Nathan Youngblood et al. “Layer-tunable third-harmonic generation in multilayer black phosphorus”. In: *ACS Photonics* 4.1 (2017), pp. 8–14.

[110] Beth Schaefer et al. “Measuring the Stokes polarization parameters”. In: *American Journal of Physics* 75.2 (2007), pp. 163–168.

[111] Stavroula Foteinopoulou et al. “Phonon-polaritonics: enabling powerful capabilities for infrared photonics”. In: *Nanophotonics* 8.12 (2019), pp. 2129–2175.

[112] Guangwei Hu et al. “Phonon polaritons and hyperbolic response in van der Waals materials”. In: *Advanced Optical Materials* 8.5 (2020), p. 1901393.

[113] Marta Autore et al. “Boron nitride nanoresonators for phonon-enhanced molecular vibrational spectroscopy at the strong coupling limit”. In: *Light: Science & Applications* 7.4 (2018), pp. 17172–17172.

[114] David J Shelton et al. “Strong coupling between nanoscale metamaterials and phonons”. In: *Nano letters* 11.5 (2011), pp. 2104–2108.

[115] R Geick, CH Perry, and GJPR Rupprecht. “Normal modes in hexagonal boron nitride”. In: *Physical Review* 146.2 (1966), p. 543.

[116] Ke Li et al. “Graphene plasmon cavities made with silicon carbide”. In: *ACS omega* 2.7 (2017), pp. 3640–3646.

[117] Mark S Anderson. “Surface enhanced infrared absorption by coupling phonon and plasma resonance”. In: *Applied Physics Letters* 87.14 (2005), p. 144102.

[118] Yuchen Yang et al. “Hybrid long-range hyperbolic phonon polariton waveguide using hexagonal boron nitride for mid-infrared subwavelength confinement”. In: *Optics express* 26.20 (2018), pp. 26272–26282.

[119] R Geick, CH Perry, and GJPR Rupprecht. “Normal modes in hexagonal boron nitride”. In: *Physical Review* 146.2 (1966), p. 543.

[120] Lisa V Brown et al. “Nanoscale mapping and spectroscopy of nonradiative hyperbolic modes in hexagonal boron nitride nanostructures”. In: *Nano letters* 18.3 (2018), pp. 1628–1636.

[121] Toan Trong Tran et al. “Quantum emission from hexagonal boron nitride monolayers”. In: *Nature nanotechnology* 11.1 (2016), pp. 37–41.

[122] Gernot Deinzer and Dieter Strauch. “Two-phonon infrared absorption spectra of germanium and silicon calculated from first principles”. In: *Physical Review B* 69.4 (2004), p. 045205.

[123] Xuesong Li et al. “Large-area synthesis of high-quality and uniform graphene films on copper foils”. In: *science* 324.5932 (2009), pp. 1312–1314.

[124] Manukumara Manjappa, Yogesh Kumar Srivastava, and Ranjan Singh. "Lattice-induced transparency in planar metamaterials". In: *Physical Review B* 94.16 (2016), p. 161103.

[125] Basudeb Sain et al. "Plasmonic flat surface Fabry-Perot interferometry". In: *Nanophotonics* 7.3 (2018), pp. 635–641.

[126] Qing-Yuan Lin et al. "Strong coupling between plasmonic gap modes and photonic lattice modes in DNA-assembled gold nanocube arrays". In: *Nano letters* 15.7 (2015), pp. 4699–4703.

[127] Peining Li et al. "Infrared hyperbolic metasurface based on nanostructured van der Waals materials". In: *Science* 359.6378 (2018), pp. 892–896.

[128] Hua Cheng et al. "Dynamically tunable broadband mid-infrared cross polarization converter based on graphene metamaterial". In: *Applied Physics Letters* 103.22 (2013), p. 223102.

[129] OV Kotov and Yu E Lozovik. "Enhanced optical activity in hyperbolic metasurfaces". In: *Physical Review B* 96.23 (2017), p. 235403.

[130] Kaveh Khaliji et al. "Tunable plasmon-enhanced birefringence in ribbon array of anisotropic two-dimensional materials". In: *Physical Review B* 95.20 (2017), p. 201401.

[131] Zebo Zheng et al. "Highly confined and tunable hyperbolic phonon polaritons in van der Waals semiconducting transition metal oxides". In: *Advanced Materials* 30.13 (2018), p. 1705318.

[132] Eve D Hanson et al. “Systematic study of oxygen vacancy tunable transport properties of few-layer MoO3- x enabled by vapor-based synthesis”. In: *Advanced Functional Materials* 27.17 (2017), p. 1605380.

[133] Gonzalo Álvarez-Pérez et al. “Infrared permittivity of the biaxial van der waals semiconductor α-MoO3 from near-and far-field correlative studies”. In: *Advanced Materials* 32.29 (2020), p. 1908176.

[134] Luke H Nicholls et al. “Ultrafast synthesis and switching of light polarization in nonlinear anisotropic metamaterials”. In: *Nature Photonics* 11.10 (2017), pp. 628–633.

[135] Nathaniel K Grady et al. “Terahertz metamaterials for linear polarization conversion and anomalous refraction”. In: *Science* 340.6138 (2013), pp. 1304–1307.

[136] Dmitry L Markovich et al. “Metamaterial polarization converter analysis: limits of performance”. In: *Applied Physics B* 112.2 (2013), pp. 143–152.

[137] Maria Cristina Larciprete et al. “Effect of heating/cooling dynamics in the hysteresis loop and tunable IR emissivity of VO 2 thin films”. In: *Optics Express* 28.26 (2020), pp. 39203–39215.

[138] Maria Cristina Larciprete et al. “Tuning and hybridization of surface phonon polaritons in α-MoO 3 based metamaterials”. In: *Optics Express* 30.8 (2022), pp. 12788–12796.

[139] Jianchen Zi et al. “Dual-functional terahertz waveplate based on all-dielectric metamaterial”. In: *Physical Review Applied* 13.3 (2020), p. 034042.

[140] Longqing Cong et al. “Highly flexible broadband terahertz metamaterial quarter-wave plate”. In: *Laser & Photonics Reviews* 8.4 (2014), pp. 626–632.

[141] Stéphane Larouche et al. “Infrared metamaterial phase holograms”. In: *Nature materials* 11.5 (2012), pp. 450–454.

[142] Alexander E Minovich et al. “Functional and nonlinear optical metasurfaces”. In: *Laser & Photonics Reviews* 9.2 (2015), pp. 195–213.

[143] Emilija Petronijevic et al. “Extrinsic Chirality and Circular Dichroism at Visible Frequencies Enabled by Birefringent α-MoO3 Nanoscale-Thick Films: Implications for Chiro-Optical Control”. In: *ACS Applied Nano Materials* 5.4 (2022), pp. 5609–5616.

[144] Zuojia Wang et al. “Optical chiral metamaterials: a review of the fundamentals, fabrication methods and applications”. In: *Nanotechnology* 27.41 (2016), p. 412001.

[145] Biao Yang et al. “Direct observation of topological surface-state arcs in photonic metamaterials”. In: *Nature communications* 8.1 (2017), pp. 1–7.

[146] Minkyung Kim et al. “Extremely broadband topological surface states in a photonic topological metamaterial”. In: *Advanced Optical Materials* 7.20 (2019), p. 1900900.

[147] Joshua D Caldwell et al. “Photonics with hexagonal boron nitride”. In: *Nature Reviews Materials* 4.8 (2019), pp. 552–567.

[148] Nikolai C Passler et al. “Hyperbolic shear polaritons in low-symmetry crystals”. In: *Nature* 602.7898 (2022), pp. 595–600.

[149] ChengLong Zhou et al. “Radiative heat transfer in low-symmetry Bravais crystal”. In: *arXiv preprint arXiv:2206.03022* (2022).

[150] Anamika Singh Pratiyush et al. “High responsivity in molecular beam epitaxy grown β-Ga2O3 metal semiconductor metal solar blind deep-UV photodetector”. In: *Applied Physics Letters* 110.22 (2017), p. 221107.

[151] XZ Liu et al. "β-Ga2O3 thin films on sapphire pre-seeded by homo-self-templated buffer layer for solar-blind UV photodetector". In: *Optical Materials* 51 (2016), pp. 203–207.

[152] Sooyeoun Oh, Chang-Koo Kim, and Jihyun Kim. "High responsivity β-Ga2O3 metal–semiconductor–metal solar-blind photodetectors with ultraviolet transparent graphene electrodes". In: *Acs Photonics* 5.3 (2017), pp. 1123–1128.

[153] Minglin Zhao et al. "Ellipsometric determination of anisotropic optical constants of single phase Ga2O3 thin films in its orthorhombic and monoclinic phases". In: *Optical Materials* 102 (2020), p. 109807.

[154] Ji-Hyeon Park, Ryan McClintock, and Manijeh Razeghi. "Ga2O3 metal-oxide-semiconductor field effect transistors on sapphire substrate by MOCVD". In: *Semiconductor Science and Technology* 34.8 (2019), 08LT01.

[155] Manijeh Razeghi et al. "Microstrip Array Ring FETs with 2D p-Ga2O3 Channels Grown by MOCVD". In: *Photonics*. Vol. 8. 12. MDPI. 2021, p. 578.

[156] Masataka Higashiwaki et al. "Gallium oxide (Ga2O3) metal-semiconductor field-effect transistors on single-crystal β-Ga2O3 (010) substrates". In: *Applied Physics Letters* 100.1 (2012), p. 013504.

[157] Junhee Lee et al. "High Thermal Stability of κ-Ga2O3 Grown by MOCVD". In: *Crystals* 11.4 (2021), p. 446.

[158] Yaobin Xu et al. "Strain-induced metastable phase stabilization in Ga2O3 thin films". In: *ACS applied materials & interfaces* 11.5 (2019), pp. 5536–5543.

[159] Ji-Hyeon Park, Ryan McClintock, and Manijeh Razeghi. "Ga2O3 metal-oxide-semiconductor field effect transistors on sapphire substrate by MOCVD". In: *Semiconductor Science and Technology* 34.8 (2019), 08LT01.

[160] Masataka Higashiwaki and Shizuo Fujita. *Gallium Oxide: Materials Properties, Crystal Growth, and Devices*. Vol. 293. Springer Nature, 2020.

[161] Mathias Schubert et al. "Anisotropy, phonon modes, and free charge carrier parameters in monoclinic β-gallium oxide single crystals". In: *Physical Review B* 93.12 (2016), p. 125209.

[162] Frank K Urban III, David Barton, and Mathias Schubert. "Numerical ellipsometry: Methods for selecting measurements and techniques for advanced analysis applied to β-gallium oxide". In: *Journal of Vacuum Science & Technology A: Vacuum, Surfaces, and Films* 38.2 (2020), p. 023406.

[163] Frank K Urban III, David Barton, and Mathias Schubert. "Numerical ellipsometry: A method for selecting a near-minimal infrared measurement set for β-gallium oxide". In: *Journal of Vacuum Science & Technology A: Vacuum, Surfaces, and Films* 39.5 (2021), p. 052801.

[164] "Ellipsometric determination of anisotropic optical constants of single phase Ga2O3 thin films in its orthorhombic and monoclinic phases". In: *Optical Materials* 102 (2020), p. 109807. ISSN: 0925-3467.

[165] Junhee Lee et al. "Study of phase transition in MOCVD grown Ga2O3 from κ to β phase by ex situ and in situ annealing". In: *Photonics*. Vol. 8. 1. MDPI. 2021, p. 17.

[166] Hsien-Lien Huang, Christopher Chae, and Jinwoo Hwang. “Perspective on atomic scale investigation of point and extended defects in gallium oxide”. In: *Journal of Applied Physics* 131.19 (2022), p. 190901.

[167] N-J Park et al. “Effect of film thickness on the evolution of annealing texture in sputtered copper films”. In: *Journal of electronic materials* 34.12 (2005), pp. 1500–1508.

[168] Xianglian Song et al. “Tunable polaritonic metasurface absorbers in mid-IR based on hexagonal boron nitride and vanadium dioxide layers”. In: *Journal of Physics D: Applied Physics* 52.16 (2019), p. 164002.

[169] Hodjat Hajian et al. “VO 2-hBN-graphene-based bi-functional metamaterial for mid-infrared bi-tunable asymmetric transmission and nearly perfect resonant absorption”. In: *JOSA B* 36.6 (2019), pp. 1607–1615.

[170] Siyuan Dai et al. “Phase-Change Hyperbolic Heterostructures for Nanopolaritonics: A Case Study of hBN/VO2”. In: *Advanced Materials* 31.18 (2019), p. 1900251.

[171] Thomas G Folland et al. “Reconfigurable infrared hyperbolic metasurfaces using phase change materials”. In: *Nature communications* 9.1 (2018), pp. 1–7.

[172] FJ Morin. “Oxides which show a metal-to-insulator transition at the Neel temperature”. In: *Physical review letters* 3.1 (1959), p. 34.

[173] FJ Morin. “Oxides which show a metal-to-insulator transition at the Neel temperature”. In: *Physical review letters* 3.1 (1959), p. 34.

[174] MC Larciprete et al. “Adaptive tuning of infrared emission using VO 2 thin films”. In: *Scientific reports* 10.1 (2020), pp. 1–10.

[175] Joyeeta Nag et al. “Non-congruence of thermally driven structural and electronic transitions in VO2”. In: *Journal of Applied Physics* 112.10 (2012), p. 103532.

[176] Changhyun Ko and Shriram Ramanathan. “Observation of electric field-assisted phase transition in thin film vanadium oxide in a metal-oxide-semiconductor device geometry”. In: *Applied Physics Letters* 93.25 (2008), p. 252101.

[177] Nagaphani B Aetukuri et al. “Control of the metal–insulator transition in vanadium dioxide by modifying orbital occupancy”. In: *Nature Physics* 9.10 (2013), pp. 661–666.

[178] Andrea Cavalleri et al. “Evidence for a structurally-driven insulator-to-metal transition in VO 2: A view from the ultrafast timescale”. In: *Physical Review B* 70.16 (2004), p. 161102.

[179] Chenghao Wan et al. “Limiting optical diodes enabled by the phase transition of vanadium dioxide”. In: *ACS Photonics* 5.7 (2018), pp. 2688–2692.

[180] Matthias Wuttig, Harish Bhaskaran, and Thomas Taubner. “Phase-change materials for non-volatile photonic applications”. In: *Nature Photonics* 11.8 (2017), pp. 465–476.

[181] Filip Ligmajer et al. “Epitaxial VO2 nanostructures: A route to large-scale, switchable dielectric metasurfaces”. In: *ACS photonics* 5.7 (2018), pp. 2561–2567.

[182] Mikhail A Kats et al. “Vanadium dioxide as a natural disordered metamaterial: perfect thermal emission and large broadband negative differential thermal emittance”. In: *Physical Review X* 3.4 (2013), p. 041004.

[183] Zizhuo Liu et al. “Dynamic infrared thin-film absorbers with tunable absorption level based on VO 2 phase transition”. In: *Optical Materials Express* 8.8 (2018), pp. 2151–2158.

[184] Sébastien Cueff et al. “VO2 nanophotonics”. In: *APL Photonics* 5.11 (2020), p. 110901.

[185] A-Rang Jang et al. “Phase Transition-Induced Temperature-Dependent Phonon Shifts in Molybdenum Disulfide Monolayers Interfaced with a Vanadium Dioxide Film”. In: *ACS Applied Materials & Interfaces* 13.2 (2021), pp. 3426–3434.

[186] Hao Wang et al. “Resonance coupling in heterostructures composed of silicon nanosphere and monolayer WS2: a magnetic-dipole-mediated energy transfer process”. In: *ACS nano* 13.2 (2019), pp. 1739–1750.

[187] Sergey Lepeshov et al. “Tunable resonance coupling in single Si nanoparticle–monolayer WS2 structures”. In: *ACS applied materials & interfaces* 10.19 (2018), pp. 16690–16697.

[188] Daehan Yoo et al. “Ultrastrong plasmon–phonon coupling via epsilon-near-zero nanocavities”. In: *Nature Photonics* 15.2 (2021), pp. 125–130.

[189] Yanko Todorov et al. “Ultrastrong light-matter coupling regime with polariton dots”. In: *Physical review letters* 105.19 (2010), p. 196402.

[190] P Forn-Díaz et al. “Ultrastrong coupling regimes of light-matter interaction”. In: *Reviews of Modern Physics* 91.2 (2019), p. 025005.

APPENDIX A

Drude parameters and enhanced plasmonic apsorption borophene

A.1. Analysis of Drude parameters in borophene

In order to provide further insight into the variables in the Drude equation for borophene (Equation 2.46), effect of each one is investigated in this section briefly. This study is carried out on y direction LSPP of α-borophene. The width of the nanoribbon in the mentioned crystal direction is 50 nm and the periodicity is set to 100 nm (similar to Figure 3.3). The mesh in the out-of-plane direction is 0.03 nm as stated earlier and the polarization of the impinging light is along y direction. The effect of significant Drude model parameters, εr, m^* ($m_j = m_y$), n, τ and d on absorption is shed light on in Figure A.1. Panels (a) through (e) in the left side of Figure A.1 illustrate the dependence of LSPP resonance on different Drude model parameters. The panels (f) through (j) on the right-hand side illustrate spectral absorption of points picked from their left panel counterpart which are colored as red squares. In all these simulation results, the default value for parameters are taken from Table 3.1 in Chapter 3.2.2 for the y direction and only one parameter is changed at a time so that the effect of varying parameters can be visualized independently.

Taking Figure A.1 into consideration, it is obvious that the resonance wavelength increases for increased effective mass. This is not surprising since according to the 2DEG dispersion model (which fits to all our material models as discussed in Figure

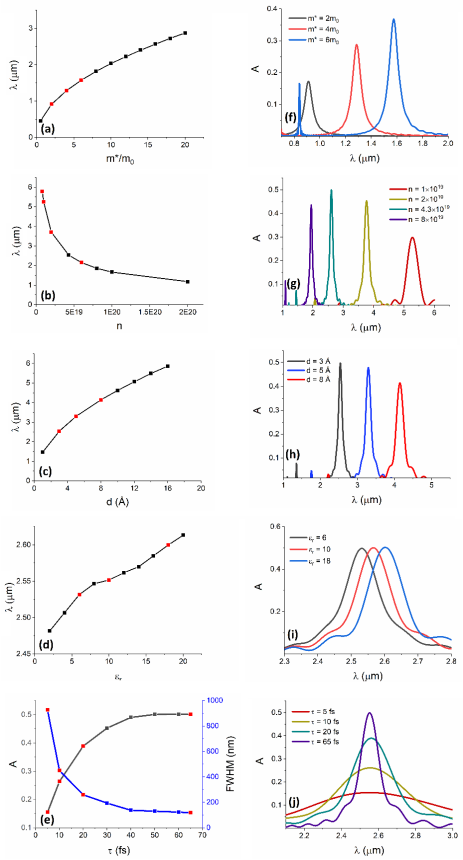

Figure A.1. Dependence of resonance wavelength on different Drude parameters (a) normalized effective mass (m^*/m_0), (b) free carrier density (n), (c) monolayer thickness (d) and (d) relative DC permittivity (ε_r). (e) Dependence of absorption strength (A) and full width at half maximum on carrier lifetime (τ). (f) – (j) Absorption versus wavelength counterparts for the red-colored dots in (a) – (d).

3.1), there is a square root dependence of resonant wavelength on effective mass. Writing this equation in terms of resonance wavelength instead of resonant angular frequency, we get

$$\lambda = 2\pi c\sqrt{2m_j\varepsilon_0/\sigma e^2 q}. \tag{A.1}$$

Fitting a square root function to the plot in Figure A.1, we get a function of the form $\lambda_{fit} = 0.6412(m^*)^{0.5} + 0.0031$ which proves the mentioned $\lambda \propto (m^*)^{0.5}$ dependence. On this figure, three different spots are selected, and their respective spectral absorption is provided in Figure A.1. Due to the curves in this figure, increasing the effective mass results in red-shifted resonance with higher absorption and narrower full width at half maximum (FWHM). This behavior can be deduced from Equation A.1 in that the higher the effective mass, the higher the real and imaginary parts of permittivity. Besides, the sharp and narrow resonance in the vicinity of 0.8 μm in Figure A.1f for the case of $m^* = 6m_0$ is the higher order mode LSPP resonance for the main resonance sitting at 1.6 μm. The discussion about square root dependence of resonance on effective mass can also be applied to the results of Figure A.1b and Figure A.1c and is avoided here for the sake of brevity. Figure A.1d illustrates the weak dependence of resonance wavelength on DC permittivity of borophene. This weak dependence is predictable since in the wavelength range of interest, the DC permittivity value is much smaller than the second term in Equation A.1. Moreover, since the resonance wavelength is almost unaltered with varying the carrier life time, it is avoided and the absorption intensity and FWHM are provided in Figure A.1e instead. Together with Figure A.1j, it illustrates that the intensity (FWHM) of spectral absorption is increased (decreased) as τ is chosen to be larger which is a natural result of a dielectric function of this form.

A.2. Enhanced absorption in borophene incorporated to a vertical cavity

In this section, we aim to elaborate briefly on the ramifications of constructing a vertical plasmonic cavity by incorporating layers from bottom to top as a thick metal, SiO_2 dielectric with thickness t and patterned borophene patch (patterned in both x and y directions) on top. It is a well-established practice to form such cavities to increase field confinement and enhancement and as a result, the absorption. This scheme indeed increases absorption to over 0.5 in both directions in borophene. In order to look at this effect closely, we have simulated a 50 nm by 50 nm patch of a phase borophene on SiO_2 and Au as illustrated schematically in Figure A.2a. The polarization of the impinging light is set to $\phi_p = \theta = 45°$ so that both resonances in the fundamental crystal directions are accessible.

The plot in Figure A.2b shows the absorption in the structure for t = 400 nm. It is obvious that adding a back reflector does indeed increase the absorption peak in both x (1.6 µm) and y (3.5 µm) LSPP resonances. These resonances are the fundamental LSPP modes in the mentioned directions. It is worth pointing out that in the results of Figure 3.5b, the maximum absorption for $\phi_p = \theta = 45°$ polarization is only 0.2. The absorption in Figure A.2b for the same polarization reaches 0.5 in both directions which emphasizes the fact that a vertical cavity boosts absorption in borophene and intensifies all the discussed phenomena such as electric field magniude. Figure Figure A.2c illustrates the dependence of spectral absorption on the thickness of the SiO_2 insulator (t). This illustration captures most of the critical information about resonances in a cavity. The dashed oblique lines are the cavity resonance modes that link the insulator thickness to the wavelength, linearly. The lowermost oblique line is the

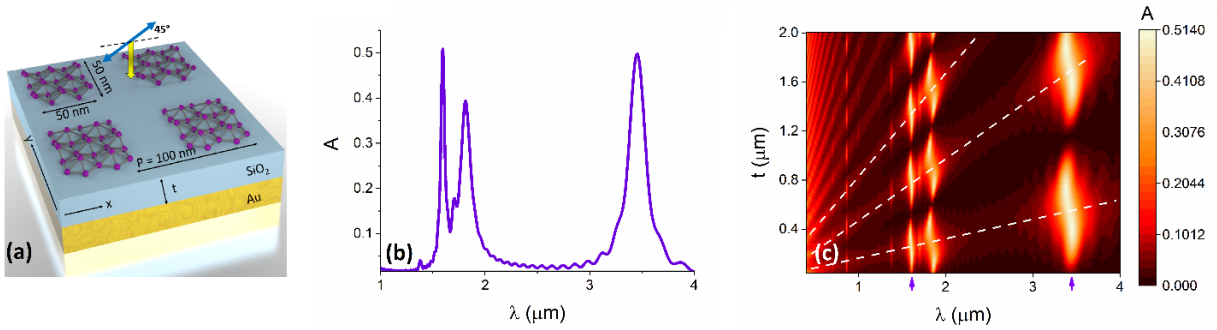

Figure A.2. (a) Schematic of the square patch borophene nanopattern forming a vertical cavity together with SiO_2 and Au with all of the simulation parameter values illustrated, (b) total absorption for the structure in (a) where the insulator thickness t is chosen to be 400 nm and (c) total absorption (A) versus insulator thickness t and wavelength (λ).

fundamental cavity mode and the other ones represent higher order modes and this behavior is a signature of interference and cavities that interact with LSPP modes and render them split. There are two modes (dark and bright) for x direction LSPPs and one for y direction at the higher wavelengths.

APPENDIX B

Coupling strength of plasmons and optical phonons in hBN

The oscillator model of the plasmonic and 1-Phz modes are illustrated in Figure B.1a where these two modes are independent. Figure B.1b represents the latter two modes in coupled condition schematically. Figure B.1c and d illustrated the fitted oscillator model that tracks the absorption peaks on the contour plots obtained from FDTD simulations.

The coupling strength is a critical parameter here to describe the enhanced interaction of optical phonons and plasmonic modes in our system, further discussion is put forth in the following. The coupling strength (g) can be calculated through the following equation,

$$g = \frac{\hbar\Omega}{2}, \tag{B.1}$$

where $\hbar\Omega$ refers to Rabi splitting energy, which could be obtained from the absorption contour, around the coupling peaks. For strong coupling, the system should satisfy the following criteria [186, 187],

$$\hbar\Omega > \frac{\hbar\gamma_{pl} + \hbar\gamma_{ph}}{2}, \tag{B.2}$$

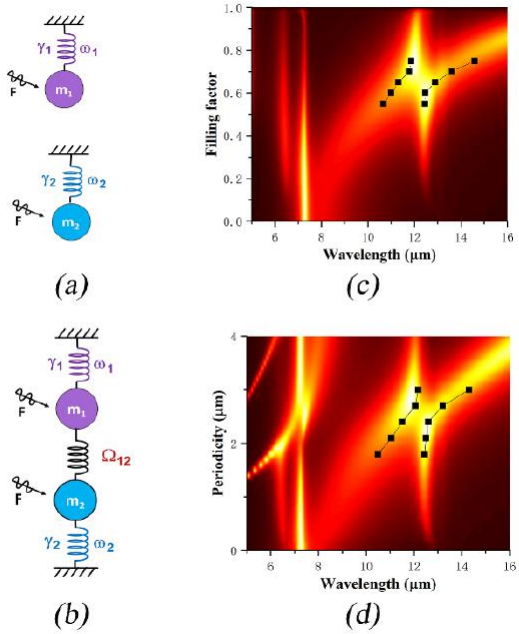

Figure B.1. The oscillator model of independent plasmonic and 1-Phz modes (a), and the two modes couplling (b). (c) & (d) Fitting oscillator model to the resoances from coupled plasmonic and 1-Phz modes, correspsonding to Figures 4.3a and d in Chapter 4 , respectively.

where γ_{pl} and γ_{ph} are the dissipation rates of the uncoupled plasmonic and phonon modes respectively. From the uncoupled oscillator model we can calculate $\hbar\gamma_{pl}$ = 130 cm^{-1} at ω_1 = 825.1 cm^{-1} for the single plasmonic mode and $\hbar\gamma_{ph}$ = 8 cm^{-1} at ω_2 = 876.48 cm^{-1} for the major optical phonon from the out-of-plane direction (1-Phz). The splitting energy from the coupled oscillator model is $\hbar\Omega_{pl-ph} = 2g = 76$ cm^{-1} at resonance freuency ω_r = 831.5 cm^{-1}. Thus, the following calculation can be obtained,

$$\frac{\hbar\gamma_{pl} + \hbar\gamma_{ph}}{2} = \frac{130 + 8}{2} = 69 < \hbar\Omega_{pl-ph} = 76cm^{-1}. \tag{B.3}$$

In Equation B.3 the total loss is smaller than the Rabi splitting energy. We can conclude here that the enhanced absorption we observe here from absorption enhancement of main out-of-plane optical phonons (1-Phz) is strongly coupled to plasmonic lattice mode. This strong coupling is realized thanks to the very sharp optical phonon resonance with small broadening factor. There are three regimes of exotic phenomena for light-matter interaction. Normalized strong coupling strength η [188] is defined as the ratio of light-matter coupling strength g to the mid-gap frequency ω_0 (orω_r),

$$\eta = \frac{g}{\omega_0}. \tag{B.4}$$

Strong coupling is usually referred to the case when $\eta < 0.1$, ultrastrong coupling (USC) regime where $0.1 < \eta < 1$, and deep strong coupling (DSC), $\eta > 1$ [189, 190]. We can calculate the normalized coupling strength for the splitting region from 1-Phz,

$$\eta = \frac{g}{\omega_r} = \frac{76/2}{831.1} < 0.1. \tag{B.5}$$

Therefore, only strong coupling takes place for our case since the interaction is not strong enough. As a result, rotating wave approximation (RWA) does not break down and the problem can be treated as a perturbation, neglecting the counter-rotating term (CRT). Hence the simplified coupled oscillator model is applicable.

APPENDIX C

Quarter wave plate frequency tuning using α-MoO_3 in IR

The main results represented in Figures 4.10 and 4.11 of the manuscript justify polarization rotation when ϕ_p = 45° and ϕ_a = -45°. This stems from the fact that the incident polarization is neither along x nor y directions. Therefore, having nonzero initial values in both in-plane directions (ϕ_p = 45°) results in the observed birefringence due to the fact that the decomposed light to the two directions experience different dielectric functions. Contrarily, if the incident polarization is set to be parallel to any of the crystal directions, no polarization rotation should be detected to cross-polarization after the analyzer. This experiment is carried out on the same sample (S2) and the result is illustrated in Figure C.1a. In this experiment, $\phi_p = \phi_i$ = 0° (parallel to x) and in the case of ϕ_a = -90° (parallel to y, pink curve), as expected, no substantial intensity is detected. Figure C.1b also shows the reflectance of the substrate (Au-Ge) for ϕ_i = 45°, while ϕ_a = 45° and ϕ_a = -45°, which is the same condition for the result of Figure 4.10. Since Au-Ge layers are isotropic, no cross-polarized reflectance signal is detected (pink curve). Besides, the green curve in Figure C.1b is used as reference to correct the attenuated detection signal due to the contribution of two polarizers (ϕ_i and ϕ_a) that render the total transmittance to less than 100%.

The circular polarization can be tuned with device parameters. From Figure 4.10c in Chapter 3, it is inferred that for S2 sample, we have two frequencies that circularly polarized reflectance is taking place (i.e. the quarter wave plate frequencies). However,

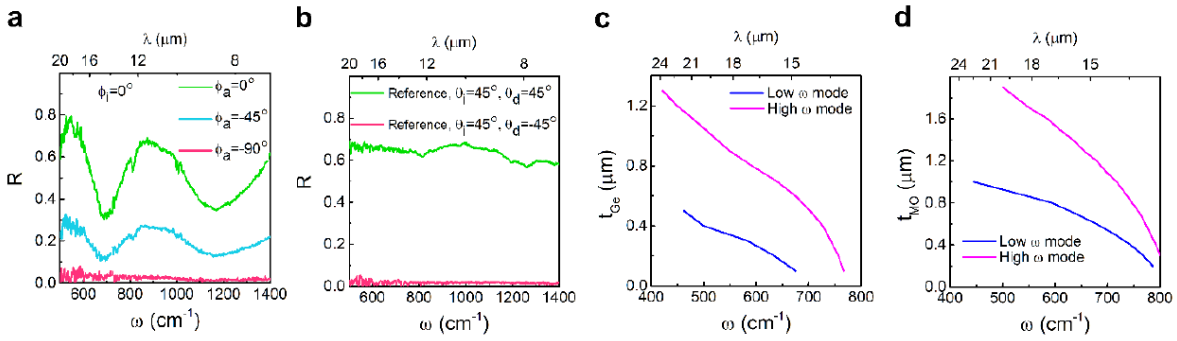

Figure C.1. (a) Reflectance of sample S2 when $\phi_p = \phi_i = 0°$, while $\phi_a = 45°$ and $\phi_a = -90°$. (b) Reflectance of Au-Ge substrate (no flake) when $\phi_p = \phi_i = 45°$ and $\phi_a = -45°$. Tracing the two modes of circularly polarized reflectance frequency (quarter wave plate frequency) when (c) $t_{MO} = 0.95$ μm and t_{Ge} is changed and (d) $t_{Ge} = 0.42$ μm and t_{MO} is swept.

due to reduced SNR in low frequency limit, the resolution of experiment does not permit for reflectance signals in the order of 10% to be recorded clearly. As a result, we observe one peak experimentally, around 730 cm^{-1}. Supplementary Figure C.1c demonstrates the effect of modifying t_{Ge} (while keeping $t_{MO} = 0.95$ μm) on the frequency of circularly polarized light can be tuned for both low and high frequency circular polarization points. Figure C.1d illustrates the effect of modifying t_{MO} (while keeping $t_{Ge} = 0.42$ μm) on the frequency of circularly polarized reflected signal. The FDTD simulation results of Figure C.1c and d are also validated by TMM calculations as demonstrated in Figure 4.10a and b, respectively.

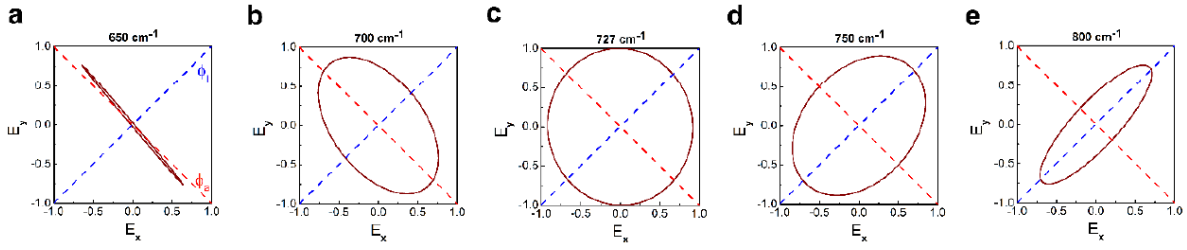

Figure C.2. Simulated reflected polarization ellipse where $\phi_p = \phi_i$ = 45° and ϕ_a = -45° at (a) 650 cm^{-1}, (b) 700 cm^{-1}, (c) 727 cm^{-1}, (d) 750 cm^{-1} and (e) 800 cm^{-1}.

The simulated polarization ellipse at 730 cm^{-1} is illustrated in Figure 4.10d. More examples of sample S2 polarization ellipse, where $\phi_p = \phi_i$ = 45° and ϕ_a = -45° (identical to the results of Figure 4.10d) at four frequency values less and greater than 730 cm^{-1} is illustrated in Figure C.2 which shows the transformation of polarization ellipse from almost parallel to -45° to 45°. Specifically, two polarization values at 700 cm^{-1} (Figure C.1b) and 750 cm^{-1} (Figure C.1c) imply that the significant rotation of polarization ellipse of approximately 90° is taking place between these two values. This is indeed true and as a result, circularly polarized reflected light is expected at 727 cm^{-1}. Contrarily, at 650 cm^{-1} a linearly polarized light is obtained.